MULTIPLE-HOLE DEFECTS: OPTIMIZING LIGHT-MATTER INTERACTION IN PHOTONIC CRYSTAL CAVITIES

By

Christopher Kang

Dissertation

Submitted to the Faculty of the

Graduate School of Vanderbilt University

in partial fulfillment of the requirements

for the degree of

DOCTOR OF PHILOSOPHY

in

Interdisciplinary Materials Science

August, 2011

Nashville, TN

Approved:

Professor Sharon M. Weiss

Professor Richard F. Haglund, Jr.

Professor Deyu Li

Professor Ronald D. Schrimpf

Dr. Solomon Assefa

To Umma, Jennifer, and Sunny,

who always keep me grounded.

ACKNOWLEDGMENTS

I arrived at Vanderbilt in June 2006, fresh from getting my undergraduate degree and probably thinking much too highly of myself. That said, I'm grateful for the many ways I've been humbled these last five years, especially by the opportunity to study with the great minds I can proudly call my colleagues and friends in the Weiss Lab.

For her guidance and mentoring, I have had the best advisor a grad student could ask for in Sharon Weiss. She has taught me what it means to be a proper scientist, has always been open to and supportive of my ideas, and has helped me to press on when the going got tough. Although she might have had her qualms about taking me on at first ("So, about your intro physics grades..."), I know that I definitely chose the right advisor, and I hope I've justified her confidence in me.

Solomon Assefa has been a great mentor to me, and I'm thankful for him taking the time to advise me during my internship at IBM and afterwards. This thesis would not have been possible without my time at Watson, which is an amazing place for a scientist to experience. I hope to see his vision of using technology to help the needs of others become a reality very soon. I would like to acknowledge the funding of the NSF IGERT fellowship program, which enabled my IBM internship experience.

I owe a lot of my device fabrication and process knowledge to the staff at the ORNL CNMS: Scott Retterer, Darrell Thomas, Dayrl Briggs, Ivan Kravchenko, Dale Hensley, and Laura Edwards, as well as those at VINSE: Bo Choi, Bob Geil, and Tony Hmelo. They have no doubt made many discoveries possible through their work and support, and I'm positive Tony's emphasis on safety has kept many bright futures intact. John in the Physics Machine Shop has enabled us to put together a lot of great measurement setups with his ideas and machining skills. Judson Ryckman and Yang Jiao have been my comrades on those many trips to Oak Ridge, and I'm grateful for the great conversations and fun times. Also, I'm thankful for Jeremy Mares and Petr Markov, the new guys in the group who have helped bring us out of our shells a bit. I always look forward to our weekly SATCO meals. Chris Phare's (C2) work on perturbation theory has contributed to making some of

the simulations outlined here more efficient.

The staff in Featheringill have been invaluable in their support: Lewis Saettel, Hampton Albert, Andy Richter, Sandy Winters, and Flo Wahidi. Flo was our mother away from home, always caring for us grad students and brightening up our days. I know her spirit will always be watching over the grad students in Featheringill from up above. I will never forget her.

Finally, this work would not have been possible without the support of my family. Since as far as I can remember (on the preschool playground!), my uncle Jan and aunt Jiyoung have supported me, and for their help I'm grateful. My sister Jennifer and I have gotten closer as we've gotten older, and I'm proud of the way she is passionate about loving what she does. My mom has always been there for me in every way, and at the risk of bragging, has done a perfect job of raising my sister and I. With an uncanny sense of right and wrong, her tough and never-give-up attitude has definitely rubbed off on me, and has helped me to become the person I am today. And last but certainly never anywhere close to least, I'm thankful for the support and love of Sunny, whose prayers and encouragement have helped the little miracles written here to happen.

TABLE OF CONTENTS

LIST OF TABLES

LIST OF FIGURES

LIST OF ABBREVIATIONS

ALD	**A**tomic **L**ayer **D**eposition
DBR	**D**istributed **B**ragg **R**eflector
EBL	**E**lectron **B**eam **L**ithography
FDTD	**F**inite **D**ifference **T**ime **D**omain
LMI	**L**ight **M**atter **I**nteraction
MHD	**M**ultiple **H**ole **D**efect
Q	**Q**uality **F**actor
PBG	**P**hotonic **B**and **G**ap
PCS	**P**hotonic **C**rystal **S**lab
PEC	**P**roximity **E**rror **C**orrection
PhC	**P**hotonic **C**rystal
PML	**P**erfectly **M**atched **L**ayer
PSi	**P**orous **S**ilicon
PWE	**P**lane **W**ave **E**xpansion
RIU	**R**efractive **I**ndex **U**nits
SHD	**S**ingle **H**ole **D**efect
SOI	**S**ilicon **O**n **I**nsulator
TE	**T**ransverse **E**lectric (polarization)
TM	**T**ransverse **M**agnetic (polarization)

CHAPTER 1

PHOTONIC CRYSTALS AND LIGHT-MATTER INTERACTION

1.1 Motivation

The study of light-matter interaction (LMI) very broadly describes the investigation of optical phenomena such as light scattering, reflection, refraction, diffraction, dispersion, and absorption. Some of the first discoveries of these phenomena date back thousands of years to the discovery of the first lenses used in ancient Greece, Egypt and Babylon. Mankind has since learned to shape, focus, filter, and bend light at will, by better understanding the nature of photons and their propagation in different kinds of materials. Among many others, the fiber optical waveguide is a good example of an application which has resulted from studying these basic principles of LMI. Indeed, the explosion of the telecommunications industry and the internet has been made possible by advancements of modern fiber optical links, which are a result of studying the total internal reflection of light in materials with low absorption.

Advances in nanotechnology and fabrication processes have resulted in the growth of silicon photonics, which combines the wide availability and low-cost of silicon with the high bit rates that can be achieved in fiber optic communications. This research has resulted in the development of silicon photonic building blocks for on-chip electro-optic modulation and signal routing, which use LMI fundamentals to study the guiding and trapping of light at the nanoscale. Active control of these nanophotonics devices is often achieved

through methods which modify the local refractive index of the waveguide material. This is done electronically by utilizing p-i-n junctions to sweep mobile carriers into the guiding region, and optically by using a high-energy pulse to excite carriers inside the guiding region through two-photon absorption, which is commonly used in pump-probe experiments [1–5]. In both cases, the LMI is actively modulated by changing the free-electron density that can directly interact with the transmitted lightwave signals at the core of the waveguides, modifying the refractive index. Thus, due to their demonstrated sensitivity to changes in the material refractive index, silicon-based photonic devices also have the potential to serve as a sensing platform for refractive index perturbations. Indeed, ring resonators [6–10], slot waveguides [11, 12], and interferometers [13–15] have demonstrated sensitivity to small perturbations such as surface-bound biomolecules. Any perturbation of the surface refractive index causes a change in the effective index of the guided waveguide mode, changing the properties of the device.

Overall, the degree of LMI in silicon photonic devices is a function of the **temporal** and **spatial** overlap of the guided light and the surface-bound material to be detected (often called the *analyte*). Resonant ring cavities created from silicon waveguide building blocks inherently improve the temporal overlap compared to a straight waveguide alone, due to the photon lifetime associated with light that is trapped inside the cavity at resonance. Any perturbation on the ring surface interacts multiple times with a trapped photon as it resonates in the cavity. Spatially, the interaction is limited to the dimensions of the top and sides of the waveguide, where the field is evanescently decaying. Increasing the photon lifetime and the interaction length is desirable for improving LMI in ring resonator cavities. This can be achieved by increasing the radius of the ring, which both increases the photon lifetime

and the total interaction length. However, increasing the ring diameter is undesirable for a compact device. Thus, a device platform must be utilized which maintains a long temporal overlap in the LMI while maintaining high spatial confinement. In order to improve the effectiveness of LMI in silicon photonic devices, methods for more effectively creating spatial and temporal light matter interaction must be investigated. Photonic crystals, as discussed in the next section, are one platform for exploring improved spatial and temporal LMI in silicon.

1.2 Introduction to Photonic Crystals

1.2.1 The Photonic Bandgap

Although so-called one-dimensional photonic bandgap structures have been known commonly as Bragg mirrors for centuries, the proposition of the existence of a photonic bandgap (PBG) for multidimensional, periodic dielectric lattices by Yablonovitch and John in 1987 [16, 17] paved the way for a new category of optical materials which control the propagation of electromagnetic waves by creating bands of forbidden states in specified regions of dielectric. The photonic bandgap can be seen as an optical analogue to the electronic bandgaps present in crystalline semiconductors and insulators, where certain ranges of energies are not accessible to propagating electrons or holes. The electronic band diagrams, which plot the energy eigenvalues of the electron wavefunction, are found by solving Schrodinger's equation in a Bloch wave basis. Bloch waves are used due to the periodic potential of the atoms in the crystalline lattice, and the atomic size scale necessitates the application of quantum mechanics.

Conversely, in a photonic bandgap material, the bands arise from the crystal-like periodicity of the dielectric material. Hence, materials that possess a photonic bandgap are often referred to as *Photonic Crystals* (PhC). The bandgap consists of a range of photon energies where light propagation is forbidden. Photons with energies falling within the bandgap decay exponentially into the PhC and are nearly totally reflected. The energy eigenvalues which are plotted in the photonic band structure correspond to the electromagnetic modes of the photonic crystal. The following section formulates the master equation of photonic crystals, which is akin to the wave equation for crystalline solids.

1.2.2 Formulation of the Master Equation

The size scale of the periodicity in PhCs is usually determined by the wavelength range of interest. For example, a photonic bandgap in the near-infrared range requires periodicity of the dielectric function on the order of a few hundred nanometers while a photonic bandgap in the terahertz region requires millimeter-scale periodicity. Maxwell's equations include built-in scalability, which allows for the formation of photonic bandgaps in wavelengths ranging from the visible to microwave, and they are the basis for formulating the "master equation" for solving modes of the crystal. As discussed in Joannopoulos et al. [18], it is assumed that: (1) the mixed dielectric medium in question is void of free charges and currents, so $\rho = 0$ and $\mathbf{J} = 0$; (2) field strengths are small enough that high order terms in the electric susceptibility χ can be ignored; that is, no non-linear effects are considered; (3) the material is macroscopic and isotropic; (4) the frequency dependence of the dielectric constant (material dispersion) can be neglected; and (5) the material is assumed to have purely real and positive $\varepsilon(\mathbf{r})$ for all positions in space $\mathbf{r}$. With these assumptions in place,

the time and spatially varying Maxwell equations are as follows:

$$\begin{aligned} \nabla \cdot [\varepsilon(\mathbf{r})\mathbf{E}(\mathbf{r},t)] = 0 \qquad & \nabla \times \mathbf{E}(\mathbf{r},t) + \mu_0 \frac{\partial \mathbf{H}(\mathbf{r},t)}{\partial t} = 0 \\ \nabla \cdot \mathbf{H}(\mathbf{r},t) = 0 \qquad & \nabla \times \mathbf{H}(\mathbf{r},t) - \varepsilon_0 \varepsilon(\mathbf{r}) \frac{\partial \mathbf{E}(\mathbf{r},t)}{\partial t} = 0, \end{aligned} \tag{1.1}$$

where $\varepsilon(\mathbf{r})$ represents the dielectric function in space. Note that ε_0 is divided out of the divergence terms due to the right side of the equation being 0. Next, the solutions are assumed to vary sinusoidally in time (harmonically), resulting in complex exponential solutions of the form:

$$\begin{aligned} \mathbf{H}(\mathbf{r},t) &= \mathbf{H}(\mathbf{r}) e^{-j\omega t} \\ \mathbf{E}(\mathbf{r},t) &= \mathbf{E}(\mathbf{r}) e^{-j\omega t}, \end{aligned} \tag{1.2}$$

where $\mathbf{H}(\mathbf{r})$ and $\mathbf{E}(\mathbf{r})$ are the spatial distributions of field contained in a mode of the crystal. These solutions can be plugged into each of the equations in 1.1, resulting in:

$$\begin{aligned} \nabla \cdot [\varepsilon(\mathbf{r})\mathbf{E}(\mathbf{r})] = 0 \qquad & \nabla \times \mathbf{E}(\mathbf{r}) - j\omega\mu_0 \mathbf{H}(\mathbf{r}) = 0 \\ \nabla \cdot \mathbf{H}(\mathbf{r}) = 0 \qquad & \nabla \times \mathbf{H}(\mathbf{r}) + j\omega\varepsilon_0 \varepsilon(\mathbf{r}) \mathbf{E}(\mathbf{r}) = 0. \end{aligned} \tag{1.3}$$

The divergence equations on the left side of 1.3 show that the solutions are modes that are transverse electromagnetic waves. That is, for plane wave solutions with wavevector $\mathbf{k}$ and field component $\mathbf{a}$, $\mathbf{a} \cdot \mathbf{k} = 0$. For example, if propagation occurs in the x-direction, the EM components are aligned with $\mathbf{a} = \hat{y}$ or $\hat{z}$. The two transverse polarizations primarily considered in this thesis are the transverse-electric (TE, $\mathbf{E}$ orthogonal to $\mathbf{k}$) and transverse-magnetic (TM, $\mathbf{H}$ orthogonal to $\mathbf{k}$). Finally, by decoupling the curl equations on the right side of 1.3, substituting for $\mathbf{E}(\mathbf{r})$ and remembering that $1/c = \sqrt{\varepsilon_0 \mu_0}$, we arrive at the

master equation:

$$\boxed{\nabla \times \left(\frac{1}{\varepsilon(\mathbf{r})} \nabla \times \mathbf{H}(\mathbf{r}) \right) = \left(\frac{\omega}{c} \right)^2 \mathbf{H}(\mathbf{r}).} \tag{1.4}$$

Eqn. 1.4 allows us to directly solve for the states $\mathbf{H}(\mathbf{r})$ of a PhC and their eigenvalues in a plane-wave basis, which allows for the plotting of dispersion diagrams for finding bandgaps and resonant modes. The equation is a function of the angular frequency of light ω and the dielectric function in space $\varepsilon(\mathbf{r})$. Software methods, which will be described in section 2.2, can be used to solve for all of the modes in a particular PhC lattice.

With the master equation in hand, it is important to consider the scalability of Maxwell's equations. The band diagrams which are plotted in this thesis are all normalized to a scale factor usually referred to as "a". In PhCs, "a" is usually set as the lattice constant of the crystal, and all other dimensions are defined relative to the lattice constant. Because of this normalization scheme, all eigenvalue solutions to the master equation are relative to the periodicity of the structure. For example, consider a periodic lattice of holes with hole radius defined as 0.2a; each hole has a relative radius of 1/5 of the lattice spacing. Any solution to the master equation for this lattice thus holds for all PhCs with identical *relative* lattice dimensions, such as [$a = 500\,\text{nm}$, $r = 100\,\text{nm}$], [$a = 25\,\mu\text{m}$, $r = 5\,\mu\text{m}$], etc. The free-space wavelength of any eigenvalue solution can then be found by taking the the normalized frequency and dividing the real lattice spacing dimension by this value. Thus, a calculated normalized mode frequency of $\omega = 0.25a$ has a wavelength of $\lambda = 500/0.25 = 2000\,\text{nm}$ for $a = 500\,\text{nm}$, and $\lambda = 100\,\mu\text{m}$ for $a = 25\,\mu\text{m}$. By first finding solutions to the relative lattice, spectral features can be "set" to be equal to a particular wavelength by changing the dimensions of the actual fabricated device.

1.2.3 Photonic Crystal Modes in Multiple Dimensions

Photonic crystals can exhibit one-, two-, or three-dimensions of periodicity in their dielectric function and are correspondingly referred to as 1D, 2D, and 3D PhCs. The simplest photonic crystals with one-dimensional periodicity are commonly known as Distributed Bragg Reflectors (DBR), as shown in Fig. 1.1. The DBR structure consists of alternating layers of two differing dielectrics as shown in Fig. 1.1. Here the lattice constant "a" is the distance between alternating layers of ε_1. Light impinging on the DBR at any angle is subject to multiple reflections and refractions as it passes through each layer. When the

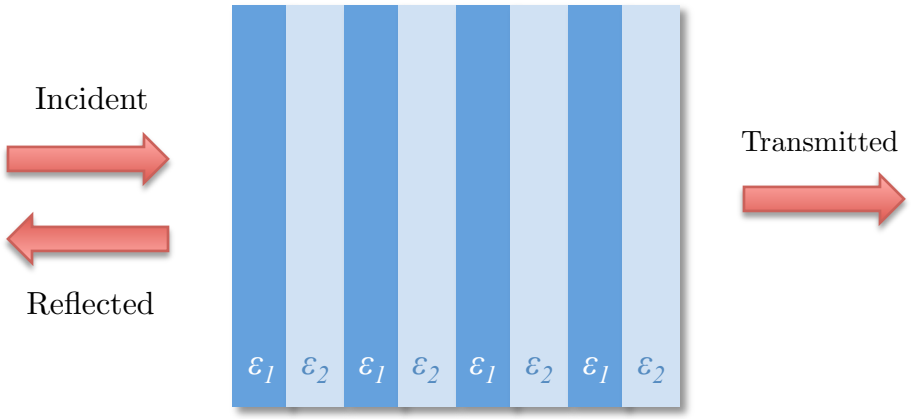

Figure 1.1: A one-dimensional photonic crystal (distributed Bragg reflector).

optical thickness of the layers correspond to quarter-wavelength thickness, bandgaps occur in the dispersion relations calculated in Fig. 1.2a. The bandgap position depends on the angle of incidence, since the optical path length changes as the slab is rotated. The dispersion diagram in Fig. 1.2b shows the folded bands of an infinite slab of dielectric, in this

case silicon, for comparison to the multilayer structure. Band folding occurs at the edges of the Brillouin zone, which is the unit cell of the reciprocal lattice. In the case of a DBR, the bands at the Brillouin zone edge ($k = \pi/a$) appear to be separated by a gap. Note that

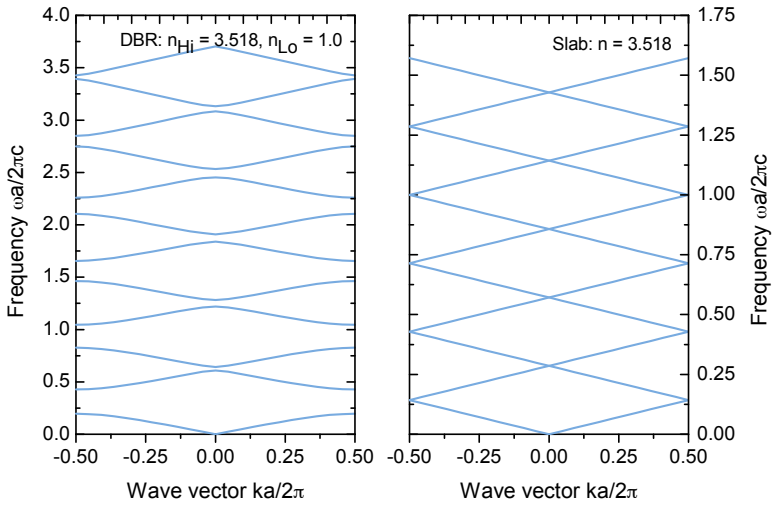

(a) (b)

Figure 1.2: The dispersion plots for (a) DBR with quarter-wave thickness alternating layers of $n = 3.518$ (silicon) and $n = 1.0$ (air), and (b) an infinite slab of silicon.

since the wave vector k is also defined as $k = 2\pi/\lambda$, the wavelength $\lambda = 2a$ equals twice the period of the DBR, which exactly corresponds to the aforementioned criterion that the layer thicknesses are set to quarter-wave optical thickness. Thus the field concentration associated with the band-edge modes form a sinusoidal standing wave having a period of $2a$. Two mode concentrations can be considered for a wave with this period, with the local energy density located either mostly in ε_1, or in ε_2, as shown in Fig 1.3. Despite their equivalent periods, the two states have slightly different frequencies due to having their energies concentrated mostly in either material, so a split of modes is created at the band edge. This split is clearly shown at the Brillouin zone edge of Fig. 1.2a when compared to

the dispersion of a slab without periodicity in Fig. 1.2b. The frequency gap which is created between the two states is called a **photonic band gap**. The different field distributions of

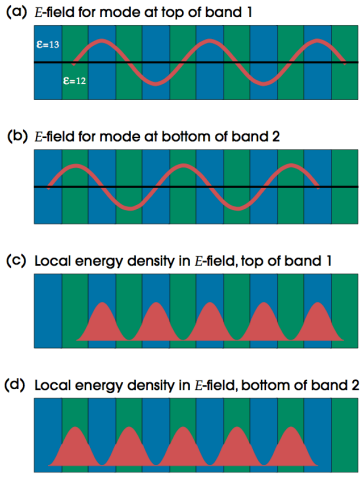

Figure 1.3: The electric field and energy density for the dielectric-band (a,c) and air-band (b,d) modes, respectively. (adapted from Joannopoulos et al. [18])

the split modes can further be explained by the electromagnetic variational theorem shown in Eqn. 1.5. From the equation, it can be shown that lower frequency modes are usually concentrated in high-ε regions in order to minimize the energy functional U_f, whereas higher frequency modes have a larger fraction of energy in low-ε regions. Because of this tendency for energy to concentrate in high/low-ε regions on either side of a bandgap, the higher frequency mode is commonly called the "air-band," and the lower frequency mode the "dielectric-band." Additionally, the orthogonality condition required by solutions to the master equation force the split mode into concentrating their energies in one dielectric or the other.

$$U_f(\mathbf{H}) = \frac{\int d^3\mathbf{r}\,|\nabla \times \mathbf{E}(\mathbf{r})|^2}{\int d^3\mathbf{r}\,\varepsilon(\mathbf{r})\,|\mathbf{E}(\mathbf{r})|^2} \tag{1.5}$$

While one-dimensional PhCs perform well as mirrors and are useful in demonstrating the concepts of the PBG, the mirror structure alone cannot guide light in the plane. Two and three-dimensional configurations of PhCs present more flexibility in guiding using photonic bandgaps. 2D PhCs, which typically require only standard silicon lithography and etching techniques for fabrication, have their bandgap limited to the plane. 3D PhCs can control light propagation for all incident angles and all directions, but they are often difficult to fabricate, and often require non-standard lithography, wet chemistry, and wafer bonding techniques. Examples of 3D PhCs include opal and inverse-opal structures [19, 20], woodpiles [21–23], and layer-by-layer construction [24]. Since 3D PhCs cannot be easily integrated with current silicon photonic technology, 2D PhC geometries such as photonic crystal slabs are more suited to silicon integrated applications, and will be discussed in the next section.

1.2.4 Two-Dimensional Slab Photonic Crystals

Two-dimensional slab PhCs have been found to be most compatible with existing semiconductor fabrication technology. Photonic crystals slabs (PCS) can be thought of as a mix of a 2D PhC in the plane and confinement by total internal reflection (TIR) perpendicular to the plane. The most common configurations of PCS consist of air holes in a slab ("hole slab"), or an isolated lattice of dielectric rods ("rod slab"). TIR requires that the refractive index of the substrate (below) and cladding (above) are lower than that of the guiding layer. A large index contrast between the guiding layer and the cladding is desirable for increased field confinement. The largest field confinement is achieved by surrounding the slab by air, which requires additional fabrication steps to form an air bridge in a hole slab. In the

case of rod slabs, each rod consists of a high index guiding region on top, and a lower cladding material on the bottom. Although the index above and below the guiding layer is not symmetric because the rod requires a solid support, a gap is still formed for guiding [25, 26].

PCS devices can be fabricated a number of ways to meet the requirements of TIR and in-plane periodicity. Both the rod and hole varieties of PCS shown in Fig. 1.4 meet these criteria. The band diagrams shown in Fig. 1.4 plot the energies of the eigenmodes as a function of propagation direction in the two-dimensional reciprocal lattice, shown in the inset. It is found that the bandgaps commonly occur with transverse-electric (TE) polarization for the hole PCS and transverse-magnetic (TM) polarization for the rod PCS [18]. Furthermore, lattice symmetry in the plane of the PCS can be defined in a number of ways; however, it has been shown previously that in a rod PCS, a square lattice can produce a photonic bandgap for incident TM-polarized light, and a hexagonal lattice can produce a gap for both TE and TM polarized light (a "complete gap") for the hole PCS [18]. For sensor applications, a large surface area is desired for increased LMI, and both hole and rod slabs provide area for molecular attachment. As will be discussed in section 1.3, the field intensity of defect modes is concentrated in regions where the symmetry of the PhC lattice is broken. Because the hole slab has the top and bottom surfaces of the defect region available for molecule attachment in addition to the inner hole surface, all the PhC structures considered in this thesis are hole slabs of air in silicon, as shown in Fig. 1.5.

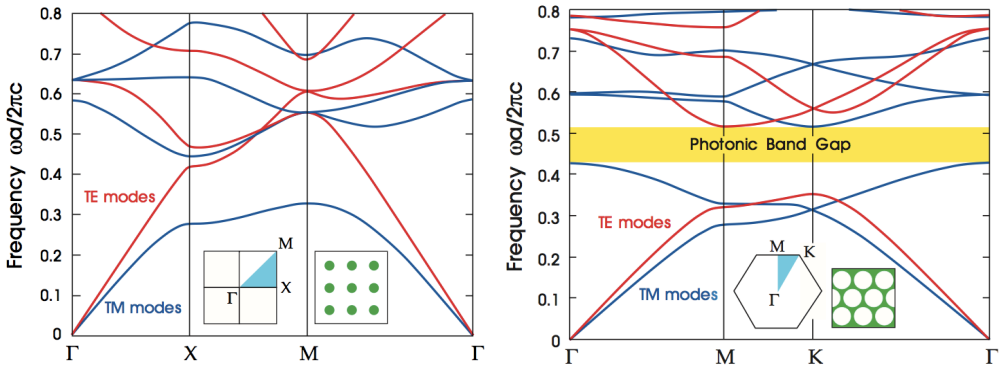

(a) (b)

Figure 1.4: The band diagrams for (a) square lattices and (b) hexagonal lattices, with insets showing reciprocal lattice directions. (Adapted from Joannopoulos et al. [18]).

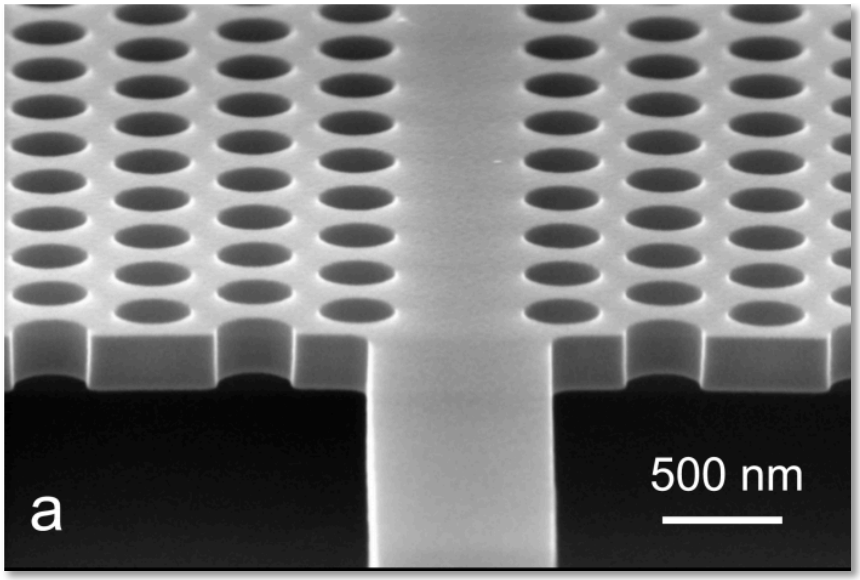

Figure 1.5: Angle-view of silicon photonic crystal slab waveguide with air holes (adapted from McNab et al. [27]).

1.3 Photonic Crystal Defects

While control over the reflectance spectrum of PhCs via the bandgap is useful for applications beyond mirrors (such as in the use of MEMS-based optical scanners [28]), the most interesting applications and devices arise when defects are introduced into the crystal lattice. Again, following an analogy to semiconductor crystals that can possess donor and acceptor defect states in the electronic bandgap, the inclusion of PhC defects create states inside the photonic bandgap, which can be utilized to selectively guide light or allow it to resonate in small volumes. The next sections will introduce these characteristics, enabled by creating line defects and point defects, respectively.

1.3.1 Line Defects: Waveguides

Controlling light propagation using PhC line defects differs from classical methods of index guiding, which use total internal reflection to confine light. Index guiding is used in applications of fiber optics and semiconductor planar waveguides when long signal propagation lengths and/or microelectronics process integration are necessary, respectively. The bandwidth of these types of waveguides is determined by the physical dimensions of the waveguide, and discrete modes are supported over a finite range of wavelengths, as governed by the wave equation [29]. Light of wavelengths that are not guided in the structures evanescently decay out of the waveguide. In a photonic crystal waveguide, light is constrained within the linear defect region primarily because it is not supported elsewhere; it is essentially trapped in the waveguide region. This is most evident in the rod PCS, where line defect waveguides can even guide light in regions of air. This is possible even though

as discussed in section 1.2.4, guiding using TIR requires the light-guiding region to have a higher refractive index than the surrounding cladding.

In hole PCS structures, waveguides are formed by filling in one row of holes in the Γ-K direction as shown in Fig. 1.6. The line defects introduce a small band of guiding states inside the bandgap, shown by the blue and red mid-gap states in the band diagram of Fig. 1.7. Light with the same momentum (frequency) as that of the defect state can propagate in the linear defect, and when only a single mode exists (such as the light-blue shaded region of Fig. 1.7) propagation occurs with very low-loss. The lowest energy state in the low-loss guiding region is referred to as "cutoff". The existence of the low-loss guiding region enables the guiding of light in sharp PhC bends with small footprints [30]. Tight bends are not possible in conventional waveguides, as the field must be modified gradually to minimize loss, which requires higher radius bends that take up valuable real estate on a fabricated chip.

The nomenclature of different waveguide types follows the number of rows removed in the defect: a "W1" waveguide has one row removed, while a "W2" has two rows missing. Adding more rows to a waveguide adds more guiding bands within the gap, whereas shrinking the waveguide width creates wider bandwidth guiding bands [31]. In addition to small-area bends, PhC waveguides can be used to couple light to point defects, which will be described in the next section.

1.3.2 Point Defects: Resonators

Resonator structures in silicon photonic devices, such as rings or disks, have been previously researched for their uses in optical filters, switches, and modulators [3, 32–36]. Many

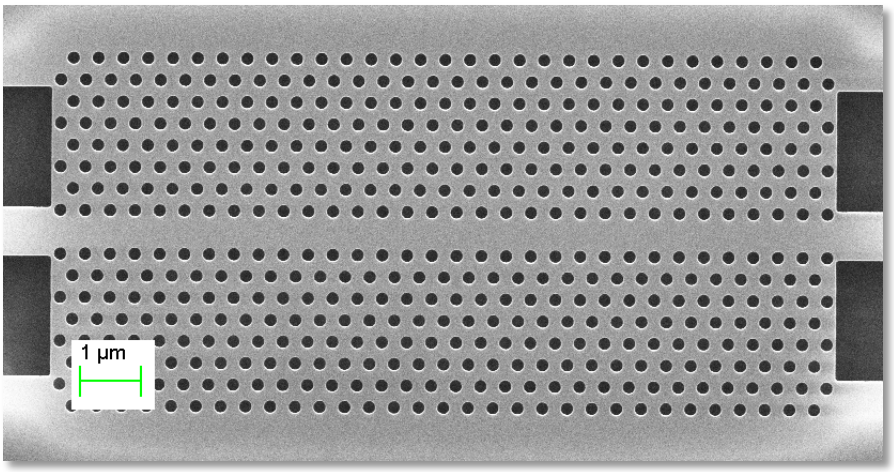

Figure 1.6: Fabricated photonic crystal W1 waveguide and input/output strip waveguides, formed by a single line defect.

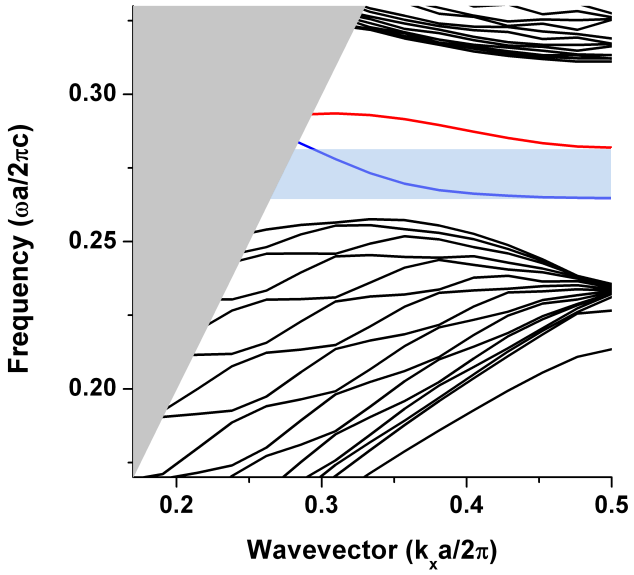

Figure 1.7: Band diagram of a W1 waveguide structure in a silicon photonic crystal slab. In the light-blue shaded region, low-loss single-mode guiding occurs. (Blue: "even", Red: "odd" symmetry modes)

of these devices require large radius bends, which can potentially increase the size of a device to several hundred square microns. Alternatively, more compact resonant cavities can be formed by creating point defects in PhCs. When the properties of one or more lattice points are modified, an isolated region of broken symmetry is created, surrounded by the periodic PhC lattice. For example, the radius of one lattice hole can be modified, making it smaller or larger relative to the surrounding lattice holes (a "single-hole defect", *SHD*), or by filling in the hole altogether. Point defects are commonly named according to their symmetry and dimensions: single filled-in holes are named "H1" defects due to their hexagonal symmetry, and filling in more holes results in a "L2," "L3," etc (due to their linear fashion) [37]. Examples of these defects are illustrated in Fig. 1.8. The broken symmetry creates a

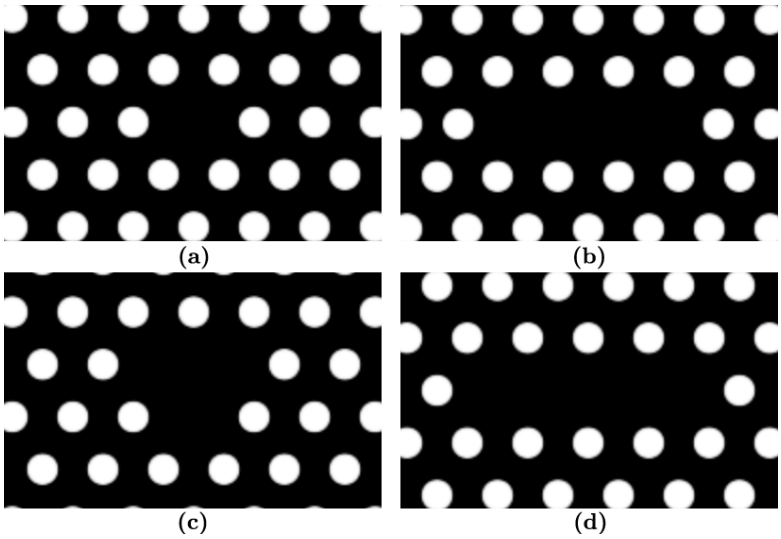

Figure 1.8: Different types of PhC cavities: (a) H1, (b) L3, (c) T3, (d) L4 type.

resonant state within the bandgap, the frequency of which is the characteristic resonance frequency of light associated with the cavity geometry. The simulation methods which are used to calculate the resonance frequency in the bandgap will be introduced in Chapter 2.

At resonance, photons are trapped inside the cavity until they are eventually lost by leakage, absorption, or scattering. The time constant τ associated with the photon energy decay in the cavity is directly related to a measurable quantity called "quality factor," commonly referred to as Q. As shown in Eqn. 1.6 below, Q relates the decay time constant to the measurable quantities of resonance wavelength/frequency, and the full-width half maximum (FWHM) of the resonance peak in the transmission. Thus, the longer light resonates inside the cavity, the higher the quality factor [29]. A small FWHM (Fig. 1.9) gives a narrower resonance and a higher Q.

$$Q = \omega_0 \tau = \frac{\omega_0}{\Delta\omega_{1/2}} = \frac{\lambda_0}{\Delta\lambda_{1/2}} \quad . \tag{1.6}$$

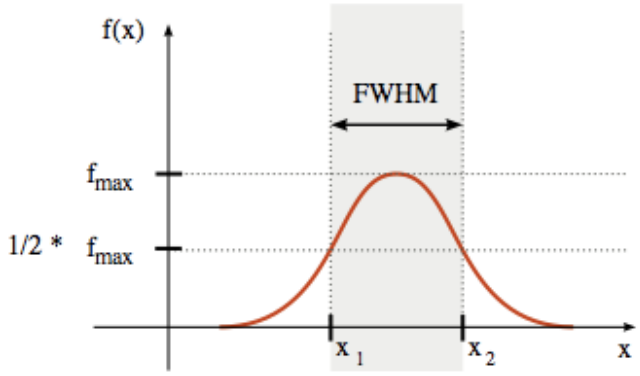

Figure 1.9: Full-Width at Half Maximum for a cavity resonance.

1.4 Advances in Photonic Crystal Sensors

Recent advances in the field of PhC-based sensing have utilized their high field confinement and long photon lifetime advantages of PhCs to demonstrate increased sensitivity to LMI. In these devices, line and point defects in PhC slabs are used to detect the refractive

index change due to fluid infiltration (bulk index sensing), as well as detect the binding of small molecules and monolayers (surface sensing). Here, the recent progress of techniques developed for PhC waveguide and cavity sensors is reviewed, as well as opportunities for improvements.

1.4.1 Waveguide-based Sensors

In a PhC waveguide, the cutoff wavelength (as discussed in 1.3.1) is the spectral feature most commonly used to track index perturbations. Waveguide-based sensors are particularly sensitive to bulk index changes, as the lattice surrounding the guiding region is easily penetrated by fluids [38]. By infiltrating the air regions with oil of a known refractive index, as performed in the work by Skivesen et al. [39], for example, the cutoff *redshifts*, or moves to higher wavelengths, as shown in Fig. 1.10. The bulk index change is a *large signal* change, which is evident in the wavelength shift of nearly 20 nm. *Small signal* changes have been demonstrated by Buswell et al. [40] in similar W1 waveguide devices, in which

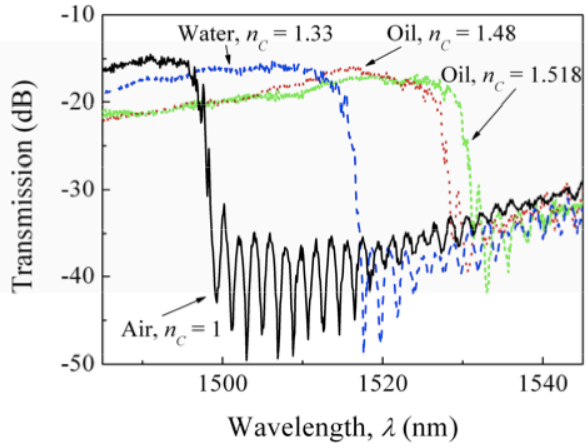

Figure 1.10: Red-shifting cutoff wavelength of W1 PCS waveguide due to oil infiltration representing a bulk index change (adapted from [39]).

biotin and streptavidin molecules are bound to the surface of a PCS and guiding layer as shown in Fig. 1.11. In this case, the redshift is much smaller, less than 1 nm, due to the smaller amount of analyte involved in the interaction. The field overlap with the molecules is mainly limited to the surface of the linear defect. The two sensors shown in Figs. 1.10 and 1.11 demonstrate that waveguide-based structure is ideal for large signal, volume index changes, and not for small signal surface sensing. Buswell et al. have shown that the waveguide can be further optimized for volume index change by adding holes to the guiding region that are smaller than the lattice holes, as shown in Fig. 1.12. By adding volume

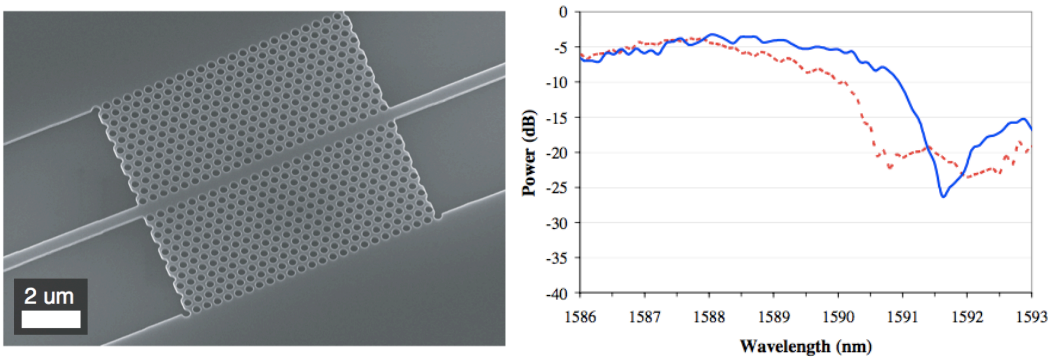

Figure 1.11: W1 PCS waveguide in silicon (left) and the cutoff wavelength redshift due to surface-bound biotin and streptavidin molecules (adapted from [40]).

directly to the waveguide region, the overlap with field is increased, and the sensitivity is improved. As will be discussed in the next chapter, the surface area enhancement can be improved by design optimizations.

1.4.2 Cavity-based Sensors

Compared to line defect waveguides, PhC point defect cavities have the advantage of additional field confinement, which increases the localized intensity of light available for LMI.

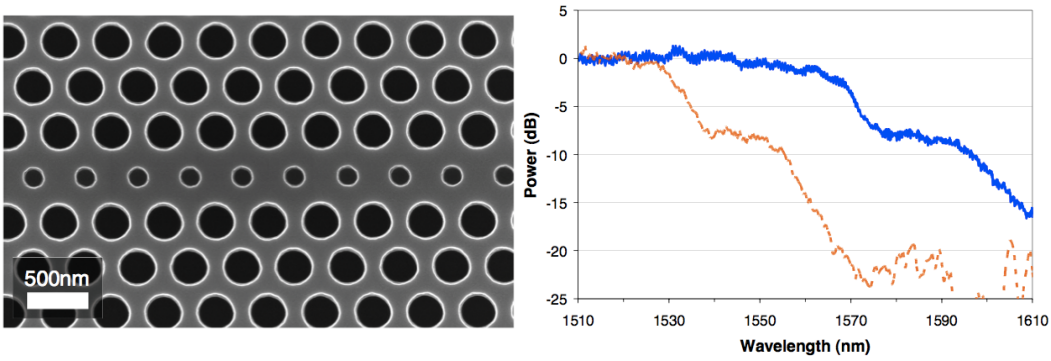

Figure 1.12: W1 PCS waveguide with direct volume enhancement (left) and the improved cutoff wavelength redshift due to bulk infiltration of DI water (adapted from [40]).

The high quality factors afforded by PhC cavities also enhance the temporal interaction with surface perturbations at the cavity due to the long photon lifetimes. Over the past several years, research to optimize defect location, size, and shape has led to PhC cavity structures in silicon and III-V materials with quality factors exceeding 10^6 [41]. Heterostructure-type cavities, which create high-Q modes by gently altering the band edge mode confinement, have achieved cavity lifetimes of up to 2 ns [42]. However, the applications of these high-Q cavities have been somewhat limited by the very tight fabrication tolerances necessary. Additionally, the implementation of these cavities for sensing applications is challenging, because resonances with extremely narrow resonances are increasingly sensitive to environmental changes such as fluctuations in temperature. As will be discussed in chapter 3, any imperfections in the lattice detract from the cavity Q by causing losses. Such losses usually arise from errors in fabrication, which can require extensive process optimization to address.

Bulk Index Change

Photonic crystals with Single-Hole Defects (SHD) having lower Q values are often suitable for demonstrations of cavity sensitivity for sensing applications [43]. Like the aforementioned waveguide sensors, photonic crystal slabs have been used in SHD configurations for bulk index sensing such as the work by Chow et al. [44] shown in Fig. 1.13. In PhC cavities constructed out of light-emitting III-V materials, SHD introduction can enable tuning of the lasing wavelength due to the infiltration of fluids that cause a bulk index change [45–47].

L3 cavities, which have larger sensing area compared to H1 cavities due to the filling of two additional holes offer higher Q compared to SHD. In the work by Dorfner et al. [48], both H1 and L3 cavities in air bridge configurations are used to detect fluids, utilizing the improved overlap with the modal field enabled by having the underlying oxide cladding removed. It is worth noting that the SHD cavity in [48] is an H1 defect with an enlarged hole (an "acceptor"-type defect [49]), which is ideal for large volume changes, but is less advantageous from a surface area standpoint, as shown in Fig. 1.14. Indeed, the large volume displaced by the defect contributes more to the spatial LMI when a bulk change occurs: the acceptor H1 cavity gives a sensitivity of $\Delta\lambda/\Delta n = 155 \pm 6\,\mathrm{nm/RIU}$, while the sensitivity of the L3 cavity is $\Delta\lambda/\Delta n = 63 \pm 9\,\mathrm{nm/RIU}$ [48]. A similar trend in sensitivity would not be expected for surface sensing applications.

Surface Index Change

In order to study the effect of small index perturbations due to surface attachment on PhC slab devices, molecular binding techniques or methods of depositing ultrathin films must be

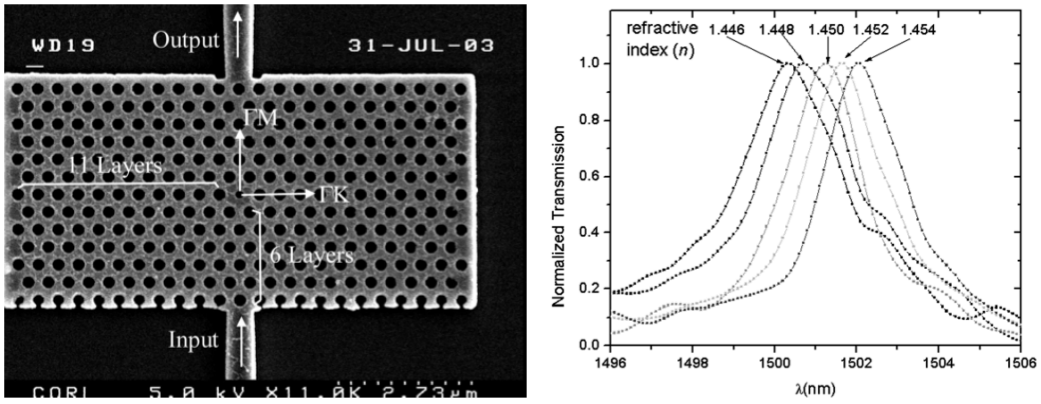

Figure 1.13: Single-hole defect H1 cavity (left), and transmission spectra when entire PhC is immersed in fluids of different refractive index (right) (adapted from [44]).

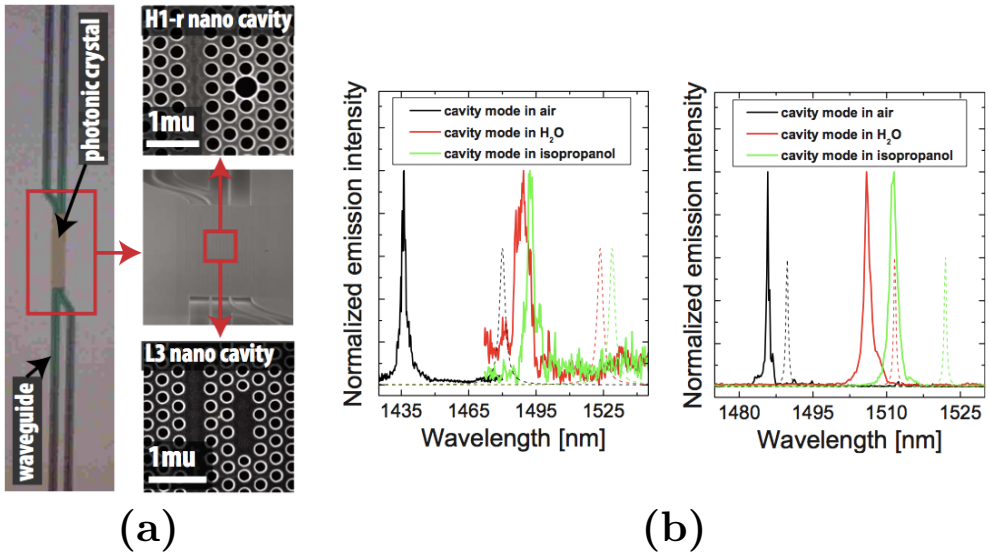

Figure 1.14: (a) Fabricated H1-type acceptor and L3 donor cavities, (b) resonance shifts of both H1 and L3 cavities due to immersion in different fluid backgrounds (adapted from [48]).

employed. In work by Lee and Fauchet [50], the binding of two different sized molecules, glutaraldehyde and bovine serum albumin (BSA), causes different magnitude resonance shifts to be measured in the transmission spectrum of a single hole defect PhC, as shown in Fig. 1.15. By enlarging the defect further into an acceptor type, larger particles such as latex macrospheres can be detected [51]. However, the aforementioned methods have not specifically examined the available surface area of the defect, which is a critical parameter for increasing the sensitivity of the device. While SHD cavities do introduce additional surface area into the cavity, the radius of the hole in the defect needs to be small relative to the slab thickness in order to gain the most surface area. For detection of smaller particles, the size of the reduced radius hole also needs to be optimized for efficient capture. Finally, in pursuit of smaller detection limits, resonances with higher values of Q are necessary to resolve minute resonance shifts, which require cavity design optimizations.

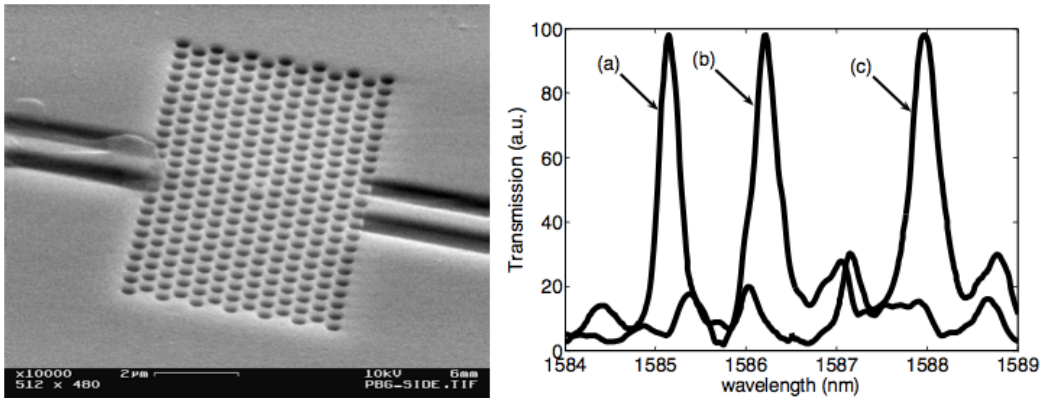

Figure 1.15: (a) Fabricated single-hole defect cavity with input/output waveguides, and (b) shift of cavity resonance due to attachment of glutaraldehyde and BSA molecules (adapted from [50]).

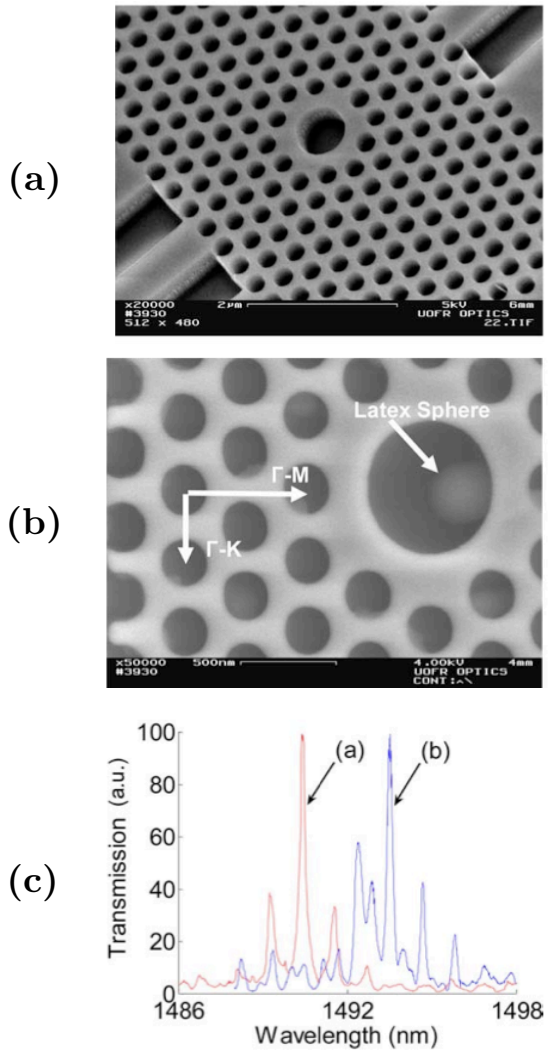

Figure 1.16: (a) Fabricated H1-type acceptor defect in hole PCS with (b) microscale latex sphere for detection, (c) resulting resonance shift (adapted from [51]).

1.5 Overview of the Dissertation

The objective of this dissertation is to investigate the effects of added surface area inside photonic crystal slab cavities, in order to increase the efficiency of both spatial and temporal aspects of light matter interaction. This is achieved by introducing the concept of the Multiple-Hole Defect (MHD), which consists of small holes directly added to a photonic crystal cavity. Several issues related to the design, simulation, fabrication, and characterization of MHD PhCs will be discussed. Chapter 2 introduces the concept of MHD and their potential for improving the LMI in sensing applications. Aspects of MHD design are explored by using simulations to characterize the MHD cavities' sensitivity to refractive index perturbations, as well as the quality factor. Both H1 and L3 types are investigated. Chapter 3 presents results from fabricated MHD cavity devices, and discusses some of the design parameters involved in the fabrication process. Details are given for the CMOS process compatible fabrication steps, as well as the entire measurement setup. Measurement results and analysis of passive MHD cavities consisting of several different designs are also presented. Chapter 4 focuses on the sensitivity of fabricated MHD cavities to bulk index changes, which is the method used for detection of fluids by immersing the device. The figure of merit and measurement methods are discussed, as well as simulation methods for initial device characterization. The measurement results of exposing the MHD cavities to fluids of different refractive indices are presented and discussed, and the sensitivity of the devices are compared to others found in the literature. The devices are then used to sense surface perturbations due to small-molecule binding, which is discussed in Chapter 5. The sample preparation methods for molecular attachment are shown, and a comparison

of sensitivity due to surface condition is presented through measurement results of native oxide and ALD oxide treated devices. Chapter 6 summarizes the highlights of the dissertation and presents possible opportunities for future research related to the MHD cavities. Appendix A presents simulation code utilized for MHD hole pattern generation and FDTD simulation.

CHAPTER 2

THEORY AND DESIGN OF MULTIPLE-HOLE DEFECTS

2.1 Overview: Multiple-Hole Defects

Photonic crystal cavities are an ideal platform for studying small perturbations in light-matter interaction (LMI) due to their ability to control both the temporal and spatial interaction between light and matter. Temporally, as mentioned in section 1.4.2, the high quality factors of PhC cavities can enable photon lifetimes in the nanosecond range. Unlike the transmission of light in a waveguide, the fields in the cavity form a harmonically oscillating mode, and the interaction with the slab material is very long when considering the speed of light. However, Q is not the only important factor when considering LMI, as other devices such as whispering gallery mode resonators can easily achieve quality factors of 10^8 and higher [52–54]. In order to make the most efficient use of the resonant mode to study the effect of small refractive index perturbations, the field should be restricted to a very small volume. A traditional waveguide is not a favorable structure for studying small perturbations to LMI since the field distribution is not localized near the surface where small index perturbations, for example due to particle attachment, can most easily occur. Spatially, the formation of a cavity in the PhC lattice has the advantage of restricting the field to the small defect region (where holes are modified) at the resonance wavelength. This creates a tightly held cavity mode which has a very small mode volume (V_{eff}). The mode volume is defined as the effective volume occupied by the total modal field, calculated by integrating the field

over all space and normalizing by the maximum value. The highly intense, compact mode of a PhC cavity is very sensitive to perturbations in the LMI throughout the cavity. For sensing applications, the small mode volume also provides the benefit of requiring only small analyte volumes for detection since the spatial interaction between light and matter can be localized to only the defect region.

Optimizing the temporal and spatial overlap in PhC cavities to achieve longer photon lifetimes and smaller cavity mode volumes improves the sensitivity of the structures to small perturbations in LMI. The temporal overlap enhancement is difficult to achieve because the Q is usually limited by device design and accuracy of the fabrication process. However, the improvement in spatial overlap is related to the cavity shape and resulting field distribution, which can be modified with "cavity engineering" design. When considering surface-bound perturbations such as particles, small organic molecules, or monolayers of material, the available binding area is the limiting factor in determining the degree of LMI that can occur. In light of this, one drawback of PhC slab cavities with missing lattice holes is that the high Q and small V_{eff} inherently constrain the majority of the modal field inside the solid slab material, which is inaccessible to surface-bound perturbations. Ideally, surface perturbations would overlap with the most intense part of the modal field. An optical material which enables this sort of overlap has been previously demonstrated in porous silicon (PSi), which is a high surface area to volume ratio material formed by electrochemical etching in HF acid. PSi has a surface area to volume ratio on the order of 100 m^2/cm^3, which substantially increases the available area for surface binding and hence sensitivity of biosensor devices [55]. The high aspect ratio of the pores, which are perpendicular to the surface, contribute to the high surface area. Several applications have taken advantage of

the high surface area of PSi, such as waveguide-based sensors for detection of biomolecules attached to the pore surfaces [56–58], microcavities and mirrors which can be controlled electrically by infiltrating liquid crystals [59–61], and drug delivery systems using PSi microparticles [62]. For monolithically integrated silicon devices, however, the usage of PSi in nanophotonics is limited by the availability of current pathways to the bulk during the electrochemical etching process. Integration of PSi using a CMOS process becomes difficult when silicon-on-insulator is used as a substrate, as the buried oxide prevents current flow to the substrate. Also, although the pores are small relative to the wavelengths of interest, PSi is lossy as an optical guiding material, due to the high scattering losses. Thus, for integration into PhC devices, another method must be used in order to add additional surface area.

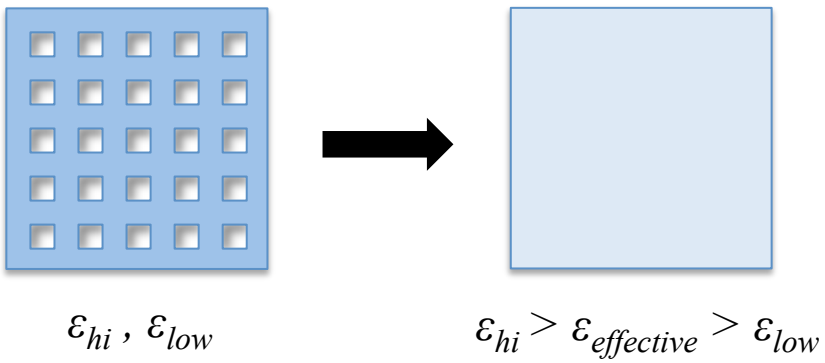

Figure 2.1: Demonstration of effective medium theory: sub-wavelength features in a high-index material result in an overall intermediate, effective index value.

By creating multiple-hole defects (MHD), which consist of arrays of small holes placed directly inside existing PhC defect structures, it is possible to combine the advantages of both silicon PhC slab cavities and high surface area porous materials. The integration

of MHD enhances the spatial overlap for LMI by bringing surface perturbations directly to the cavity mode where the field is strongest. Using modern lithography and etching techniques, holes as small as a few tens of nanometers wide can potentially be fabricated monolithically with the PhC lattice structures. The regions where MHD are introduced can be optically treated as having a uniform, effective index as illustrated in Fig. 2.1. A mixed dielectric media with features smaller than the wavelength can be considered optically as a single effective medium [63, 64]. While scattering is minimized due to feature sizes being smaller than the wavelength of light, mixed dielectric media tend to be lossier than a true, isotropic material. Assuming that a uniform diameter hole can be fabricated in a slab of silicon, the increase in area per added hole is directly proportional to the aspect ratio in the slab t/r, where t is the slab thickness and r is the hole radius.

However, engineering the MHD cavity for optimal surface area and, for sensing applications, analyte interaction can be challenging for several reasons. Small, sub-wavelength sized holes with high aspect ratio are needed for high area/volume ratios, and isolated features of this size are often difficult to fabricate even with known processes. Due to the sensitivity of the cavity mode to any refractive index perturbation, the placement of the holes can be very specific to the field distribution in the cavity. Also, the effect of larger hole sizes must be taken into account, in order to accommodate larger-sized molecules for sensing applications. In order to understand these properties, comprehensive simulations are necessary prior to fabrication, and these methods are discussed in the next section.

2.1.1 Nomenclature

We define the following terms for clarity:

- *Defect region* (*MHD region*) = area in which symmetry of surrounding photonic crystal is broken
- *Defect hole* = one of many small holes inside the defect region
- *Defect hole radius* = radius of a defect hole
- *Defect* (*region*) *effective radius* = radius of entire defect region that contains multiple defect holes
- *Photonic crystal holes* = periodic holes of photonic crystal with center-to-center spacing "*a*"

2.2 Simulation Methodology

Finite-difference time-domain and plane wave expansion methods are used to simulate MHD PhC devices before fabrication takes place. Freely available open-source packages are used for both simulation and code generation, as discussed in the next sections. All packages are compiled from source for the available `Ubuntu` linux systems. Source code for the programs used to perform simulations, as well as information about the hardware used, are available in Appendix A.

2.2.1 Plane Wave Expansion

Plane wave expansion (PWE) is a frequency-domain computational method which can be used to directly solve for eigenstates of the *master equation* (Eqn. 1.4). The bandgap of the photonic crystal can then be found by plotting the band diagram, using the calculated eigenvalues of the modes. The software package '`mpb`' (MIT Photonic Bands) [65] was used for the MHD slab photonic crystal simulations, which is a block-iterative method for solving Eqn. 1.4 in a periodically-bounded supercell, as shown in Fig. 2.2 [66].

The iterative method uses a pseudo-random field to initiate the eigensolver, and the modes are solved over a spatial grid determined by the resolution parameter, until good

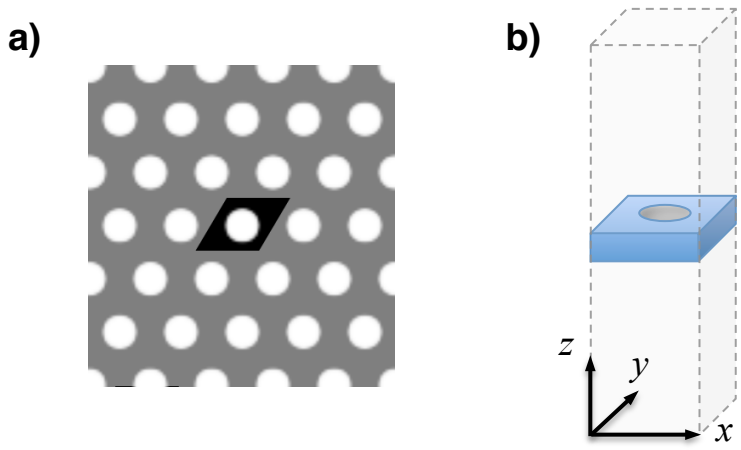

Figure 2.2: (a) Plot of the photonic crystal dielectric function, highlighting the unit cell of interest in the hexagonal basis, and (b) 3D supercell used for bands calculations, showing vertical separation between slabs.

agreement with a preset convergence factor is reached. The resolution in this case is defined as the number of points per lattice constant 'a'. For the 2D photonic crystal slab, which is periodic only in the plane of propagation, the periodic boundary condition holds for the x and y-directions of the supercell illustrated in Fig. 2.2. The periodic boundary condition repeats the supercell in all dimensions according to the specified basis vectors. For the case of the hexagonal lattice, the basis vectors are specified as $(\frac{1}{2}, -\frac{\sqrt{3}}{2})$ and $(\frac{1}{2}, \frac{\sqrt{3}}{2})$. In the z-direction, no periodicity inherently exists, since there is only the slab surrounded by air on top and bottom. For the purposes of the mode solver, a periodic boundary is forced in the z-direction of the supercell as well, but the "virtual" slabs located in the cells above and below need to be separated by a large enough distance so that the fields emanating from each do not affect each other. For 3D slab simulations, the vertical dimension of the supercell is set to 4 lattice constant units in order to provide this separation. Increasing the vertical dimension beyond 4 units is redundant, and only results in longer simulation times due to more memory used. In the following discussion, PWE is used primarily to solve for the band gap of the surrounding lattice in the MHD cavity devices.

2.2.2 Finite-Difference Time-Domain

Finite-difference time-domain (FDTD) analysis [67] is a numerical, time-domain method of examining the propagation of electromagnetic fields by solving Maxwell's equation in dielectric structures. The desired dielectric structures and dipole sources are placed inside a spatially-gridded 'cell' and the fields are iterated in time by calculating the electric and magnetic field over all grid points. In time-domain simulations, Fourier analysis enables the frequency response of structures to be computed by using a source with a broadband frequency component (a short pulse in time). The software package '`meep`' [68] was used for FDTD simulations, which supports subpixel averaging of dielectric interfaces for increased accuracy [69]. ε-averaging improves the modeling of high contrast dielectric interfaces by averaging features when they cannot be clearly resolved by the set resolution.

For cavity simulations in FDTD, a periodic boundary condition is not applicable, so another must be chosen. Fields radiating away from the cavity must be kept from being reflected back at the edge of the simulation cell. Such reflections could interfere with the measurable quantities of interest, especially for cavity devices, where the quality factor depends on the field decay in time. Therefore, for non-periodic boundaries a perfectly-matched layer (PML) is implemented, which absorbs all fields leaving the simulation cell [70]. The main drawbacks to the FDTD method are the potentially long simulation times and computational resources necessary, which are directly proportional to the resolution of the cell (like `mpb`, defined in terms of the scaling constant a). The time-iterative nature of the method requires that the field at all points must be stored in memory, which can become a limiting factor as dimensions and resolution scale up. Therefore FDTD is generally not utilized for full nanophotonic circuit simulations, but useful for the analysis of primitive components.

2.2.3 Harmonic Inversion

For cavity analysis, the stand-alone cavities are simulated without waveguide coupling in order to extract the ideal quality factor. When searching for cavity modes, a broadband frequency source is first used to excite the range of frequencies in the photonic band gap, which can result in several different modes oscillating together in the cavity, each with its own time constant. A harmonic inversion code based on the filter diagonalization method ('`harminv`') [71] is used to decouple each of the sinusoidally oscillating modes and extract their quality factor and resonance frequency, as shown in Fig. 2.3 [72]. `harminv` will often report more than one mode exists. The extraneous values are usually the radiative slab modes which may still be in the PhC, and the value with the highest Q is usually the actual cavity mode. In this work, all reported values of Q from simulation are extracted from `harminv`.

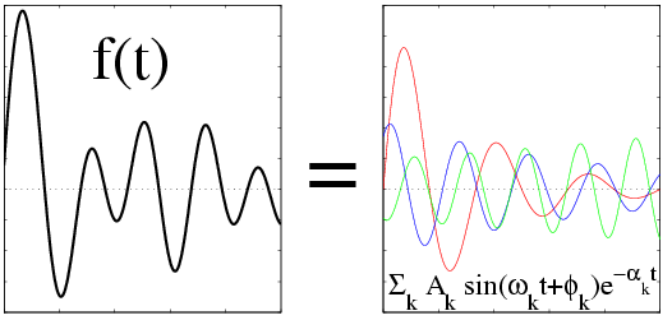

Figure 2.3: Demonstration of `harminv`, which decouples harmonically oscillating waves into their discrete Fourier components.

2.2.4 Lattice Generation

The positions of the photonic crystal lattices and multiple defect holes were generated using a `python` script, which can be found in Appendix A. Hole positions are generated by translating the hexagonal-basis coordinates of each hole into cartesian coordinates, and

generating code in the meep format to be inserted into the source.

2.3 Multiple-Hole Defects: H1 Cavities

For the first study of the defect hole interaction with the modal field a simple H1 type PhC cavity is considered, as shown in Fig. 2.4.a. Following the discussion in section 2.1, the addition of the multiple-hole defect in the cavity modifies the effective index of the mode, enabling direct light matter interaction inside the cavity. The effect of changing one or more of the size, spacing, and number of defect holes in the cavity is studied in order to understand the full characteristics of the MHD layout and design. The analysis was performed using two different conditions on the dimensions. First, the size and spacing of the defect holes were held constant and the effective MHD radius was changed. In the second analysis, the ratio between size and spacing of the defect holes was kept constant, essentially keeping the effective index of the MHD region constant. Both analyses will be explained in greater detail in the following sections, and trade-offs between surface area, sensitivity to small index perturbations, and quality factor are examined for both cases. Here it is important to note that although the H1 MHD cavities were simulated in two dimensions only, the concepts apply to a 2D slab configuration due to the bandgap existing solely in the slab plane.

2.3.1 Simulation Methods

A PhC hole radius of $0.4\,a$ was chosen in order to open a large photonic bandgap. The bandgap was calculated using mpb, and occurs between the frequencies of 0.2462 (dielectric band) and 0.4052 (air band) as shown in Fig. 2.5. The positioning of the defect holes is automatically generated by a script, which outputs cylindrical objects in meep syntax. The desired spacing and radius of the defect holes are used as inputs to the script, and

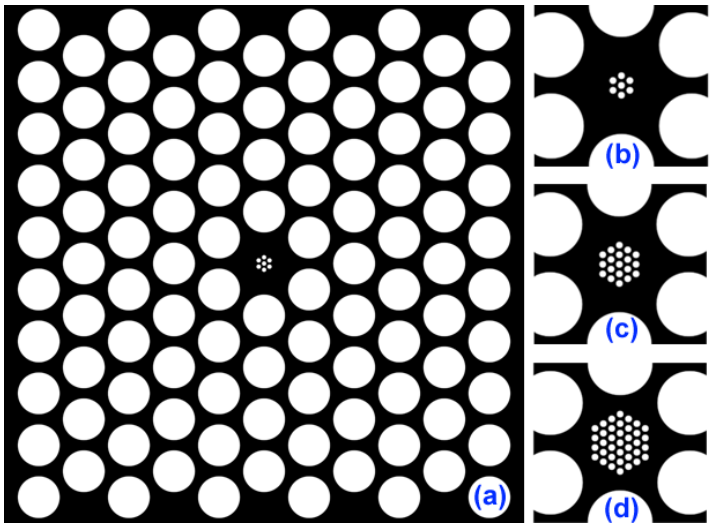

Figure 2.4: (a) Dielectric constant plot of MHD simulation space, where black indicates $\varepsilon = 12$ (silicon), white indicates $\varepsilon = 1$ (air). Detailed MHD regions with effective radius (b) 0.2 a, (c) 0.3 a, and (d) 0.4 a are also shown. The defect hole radius in all cases is 0.04 a, with defect hole spacing 0.12 a.

all possible positions which fall within a specified circular region are outputted. Partial holes were not considered. In order to fill in the area most efficiently, a hexagonal lattice is used for the positional layout, starting with a hole at position (0,0). Different effective defect radii were evaluated, as illustrated in Fig. 2.4.b-d. The small holes constituting the MHD are more than an order of magnitude smaller than wavelengths falling within the photonic band gap of the surrounding photonic crystal. The resolution of the simulation was increased to 150 grid lines per unit a in order to resolve the relatively small size of the defect holes. All simulations of the H1 MHD cavities were carried out at this higher resolution in order to obtain consistent comparison results.

In order to excite cavity resonances, a Gaussian source with center frequency and width matching that of the photonic band gap was positioned in the middle of the MHD region and run for several periods before turning off. The source is placed in the center in order to maximize the coupling to the single resonance mode. The resulting cavity mode is shown in

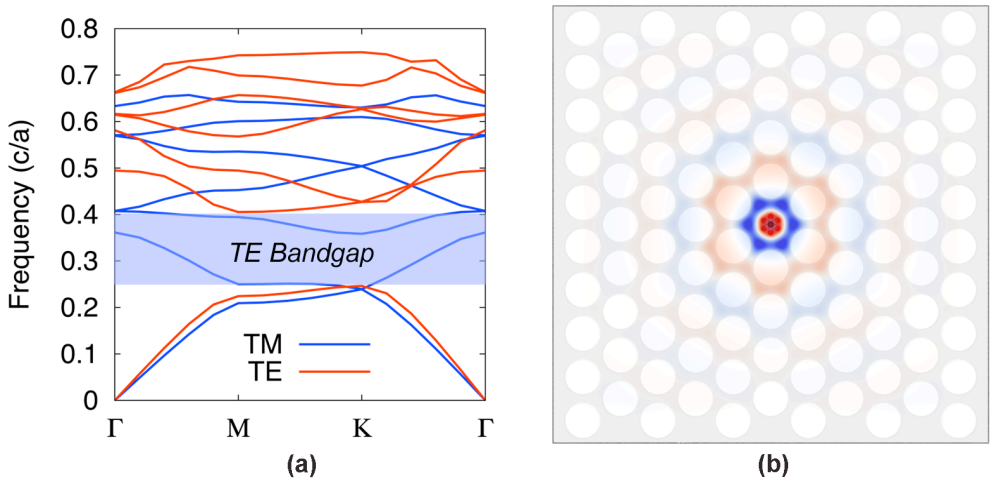

Figure 2.5: (a) Photonic bands for the photonic crystal with lattice hole radii of 0.4a. A photonic bandgap exists for only for the TE polarization between 0.2462 and 0.4052. (b) Field distribution for a MHD with effective radius 0.2a, with defect hole radius and dielectric constant 0.04a and 1.05, respectively.

Fig. 2.5b, where 7 defect holes are included to show the maintained field uniformity. The remaining resonating fields were then analyzed with `harminv`. The simulation area was bordered by a 1-spatial unit thick PML, which ensures no reflections occur at the cavity boundaries. The simulation grid covered approximately 10 periods of the photonic crystal lattice, which increased the maximum achievable cavity quality factor for the device to that of comparable devices [45].

2.3.2 Surface Area Enhancement

The primary advantage of the MHD PhC is the increased surface area that results from the multiple holes utilized in the defect region. For example, biosensing applications require biomolecules to be immobilized on a surface. Hence, available surface area is the limiting factor for the number of molecules that can be attached. Larger numbers of immobilized biomolecules, often referred to as probe molecules, increase the likelihood of capturing and detecting the complementary biomolecules of interest, often called target molecules.

Optical switching applications that rely on the attachment of an electro-optic polymer may also benefit from the increased surface area of MHD photonic crystals.

In order to quantitatively demonstrate the surface area enhancement achieved by MHD photonic crystals compared to traditional SHD PhCs, the surface area for various MHD structures and SHD structures was calculated. The defect holes were generated as described in section 2.2.4 and a PhC slab thickness of $0.7\,a$ was assumed in the calculations. Fig. 2.6 summarizes the results of the surface area calculations, where (a) shows the effect of spacing out constant radius defect holes, and (b) shows the surface area increase when defect hole radii are reduced. In Fig. 2.6a, the available surface area increases as expected when the defect hole spacing is reduced, since more holes can fit into the effective MHD region. Similarly, Fig. 2.6b shows that smaller radius defect holes are more effective for creating more surface area within the MHD region, due to the aspect ratio increase in smaller holes. For large defect effective radii, the available surface area for a MHD approaches nearly 25 times that of the single hole. Fig. 2.7 provides schematics for many of the MHD configurations considered in Fig. 2.6.

2.3.3 MHD Effective Radius Modulation

Resonance Frequency

When considering the application of sensing surface perturbations, the design of the MHD cavity would need to be tailored to the size of the perturbation in question. For example, large size particles require larger defect holes. Since fewer large diameter defect holes can fit within a given MHD effective radius, in order to maintain a large surface area for light-matter interaction, the effective radius of the MHD can be increased. In order to evaluate how the sensitivity towards index perturbations in the PhC cavity scale with the effective defect radius, FDTD simulations were carried out in which the dielectric constant of the

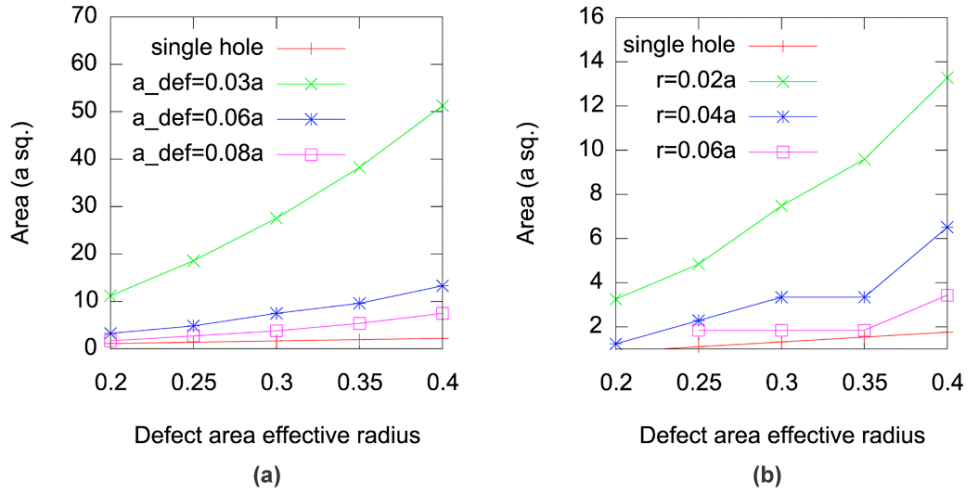

Figure 2.6: Surface area in units of a^2 assuming device slab thickness of 0.7a, for (a) defect radius held constant at 0.02a and variable defect hole spacing, and (b) relative spacing kept constant at $a_{defecthole} = 3 * r_{defecthole}$ with variable defect hole radius. A plot of the SHD surface area is also shown for comparison.

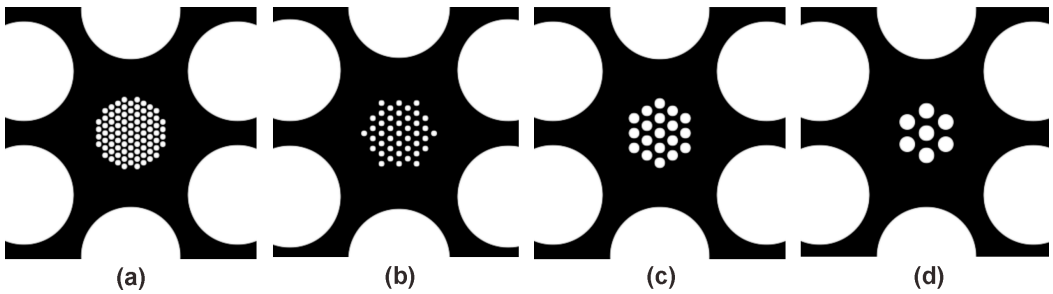

Figure 2.7: View of defect regions for generated MHDs corresponding to some of the configurations analyzed in Fig. 2.6: defect holes with (a) radius 0.02a, spacing 0.06a, (b) radius 0.02a, spacing 0.08a, (c) radius 0.04a, spacing 0.12a, and (d) radius 0.06a, spacing 0.18a. All defects have a specified effective MHD radius of 0.3a.

individual defect holes was varied between 1 and 12 (silicon) for three different MHD effective radii. The defect hole radius and spacing were held constant at 0.04a and 0.12a, respectively. Fig. 2.8 shows the relationship between the MHD photonic crystal resonance frequency and dielectric constant of the defect holes.

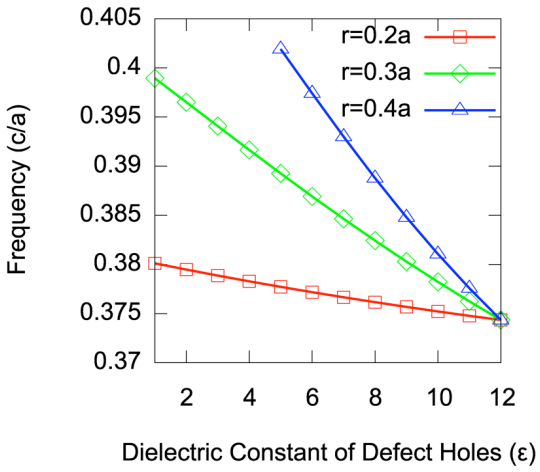

Figure 2.8: Resonance frequency for varied defect hole dielectric constant and MHD effective radius.

The slope of each curve shown in Fig. 2.8 represents the sensitivity of the specified MHD photonic crystal. For sensing applications, it is desirable to design a device that has a large resonance frequency change for small dielectric constant changes (i.e., steep slope). In general, the largest slope and maximum sensitivity occurs for larger effective MHD radii. Because larger effective radii provide more surface area, the amount of spatial light-matter interaction is increased. However, below a defect hole dielectric constant of approximately 5, the mode corresponding to a MHD with effective radius 0.4a is no longer supported due to the state being pushed into the air band. Upon close inspection of Fig. 2.8, the slopes of the MHD resonance plots are not linear, but change with increasing slope for lower defect hole dielectric constant. The maximum achievable sensitivity thus increases for defect hole dielectric constants near that of air, or $\varepsilon = 1$. Physically, this condition is

favorable for small molecule sensing because the index contrast between the air/silicon is large, and for most materials involved in sensing (such as fluid backgrounds) the value of ε is on the lower end of the simulated range.

Quality Factor

Increasing the surface area by making the effective MHD radius larger also affects the quality factor due to a lowered effective index. The more defect holes added to the cavity, the larger the fraction of air in the cavity, which reduces the effective index of the cavity based on the effective medium approximation. Fig. 2.9 shows the cavity quality factor for MHD photonic crystals with different defect hole dielectric constants and different effective radii. The defect hole radius and spacing are held constant at $0.04\,a$ and $0.12\,a$, respectively. The quality factor increases with decreasing effective MHD radius. The field distribution for a $0.2\,a$ effective radius MHD confirms the mode is monopole in Fig. 2.5b. Larger effective radii contribute a greater perturbation to the field and dielectric constant within the defect region, causing the quality factor to drop by nearly a factor of 5. Alternatively, the lowering of the effective modal index can be seen as pushing the resonant frequency towards the air band edge, which results in more leakage to radiative slab modes, creating more loss. For all MHDs, the quality factor reaches the same maximum value when the defect area is completely filled with high-index material (silicon); in this case, the MHD is essentially replaced with a solid defect (i.e., missing lattice hole).

Based on the results shown in Figs. 2.8 and 2.9, there is a clear trade-off that occurs between sensitivity and cavity quality factor in the H1 MHD cavities, which affects the design of the MHD photonic crystal for specific applications. For example, at low defect hole dielectric constants, sensitivity is high for effective radii of $0.3\,a$; however, in this regime of dielectric constant, the cavity quality factor is the lowest. For silicon-based

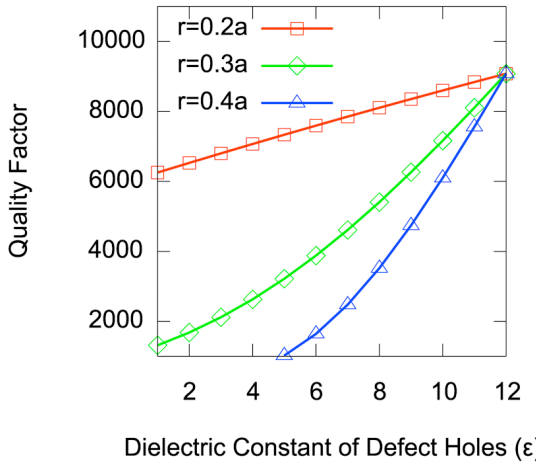

Figure 2.9: Change in cavity quality factor for varied defect hole dielectric constant and effective MHD radius.

photonic crystal sensors, depending on the refractive index of the material to be detected and the accuracy of available measurement equipment, a MHD pattern can be generated to appropriately balance quality factor and sensitivity by changing the MHD effective radius. It is also possible to change the defect hole radius and spacing to modify the sensitivity and quality factor: smaller defect holes spaced closer together offer larger surface area and greater sensitivity, but also lower quality factor.

2.3.4 Constant Effective Index

In section 2.3.3, it was shown that adding more surface area to the cavity by increasing the effective MHD radius increases the sensitivity, but reduces the cavity Q significantly. Therefore to preserve Q it is desirable to use a small effective MHD radius, and then utilize many small holes in order to maximize the surface area. The design considerations for the defect hole layouts are thus restricted to the defect hole size and spacing. Comparison of different designs can be simplified by fixing the ratio between the defect hole radius and spacing, which holds the effective index of the region constant. This can be shown

by considering an area of fixed size inside the MHD effective radius boundary. Because the effective index approximation takes into account the fraction of high and low index materials within the area of interest, scaling the dimensions (defect hole size and defect hole spacing) by the same factor retains the same relative fractions, and the effective refractive index is kept constant. As a result, a cavity of constant effective MHD radius with two different designs can have the same effective index, but widely varying surface area. An example of this is illustrated in the previous section's Fig. 2.7a,c,d, which share a constant ratio of 3 between radius and spacing. In this section, the effect of changing the available surface area contained within similar effective MHD radii are examined by simulation, in the interest of enhancing the spatial LMI.

Simulations were performed for H1 MHD cavities with a range of defect hole dielectric constants, representing additional material added inside the defect holes for active photonic crystal applications. The defect hole radius was varied as $0.02\,a$, $0.04\,a$, and $0.06\,a$, with respective defect hole spacings of $0.06\,a$, $0.12\,a$, and $0.18\,a$. The ratio between radius/spacing is set as 3. For these three defect hole sizes, the defect effective radius was varied as $0.2\,a$ and $0.3\,a$. In the case of defect hole spacing $0.18\,a$, only the $0.3\,a$ effective radius MHD was simulated, as a smaller defect effective radius resulted in only one defect hole by the hole generation algorithm.

Resonance Shift

Similar to the simulations in section 2.3.3, the resonance wavelengths of each simulated MHD PhC are plotted in Fig. 2.10 as a function of the defect hole dielectric constant. The slope of the curves shown in Fig. 2.10, which can be taken as the sensitivity of the MHD to changes in defect hole refractive index, is again found to be higher for larger defects.

Because the effective index is assumed to be equivalent for similar effective MHD radii,

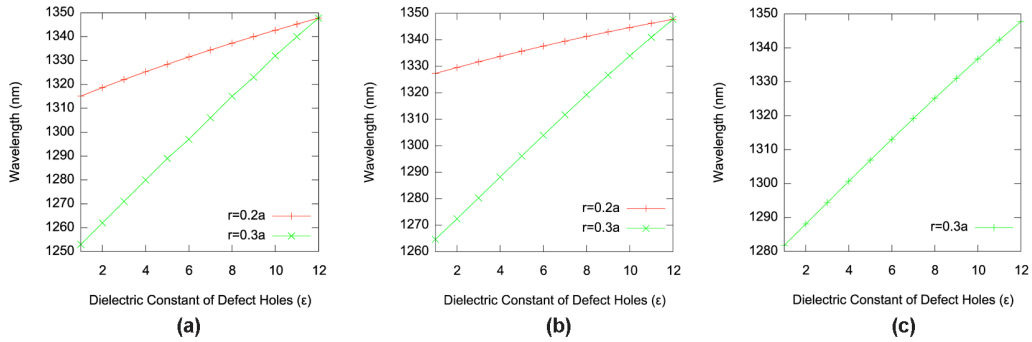

Figure 2.10: Resonance wavelength of the H1 MHD for varied dielectric constant and defect hole radius/spacing: (a) radius 0.02a, spacing 0.06a, (b) radius 0.04a, spacing 0.12a, (c) radius 0.06a, spacing 0.18a.

comparisons can be made between the red curves of Fig. 2.10a-b and the green curve in Fig. 2.10a-c. It is found that for MHDs with the same effective defect radius but differing defect hole size and spacing, the resonance wavelength trend differs slightly. Since the ratio of defect hole size and spacing is equivalent, and thus the effective index within the defect regions are equal, the anticipated behavior of the MHD photonic crystals should be the same. However, Fig. 2.10 shows that the wavelength of the resonance state increases as the defect hole spacing is increased. For example, for the effective MHD radius of $r = 0.2a$ (red points), the resonance wavelength at $\varepsilon = 1$ is 1315 nm for $a_{def} = 0.06a$, and 1328 nm for $a_{def} = 0.12a$. Similarly, for the MHD effective radius of 0.3a (green points), the resonant state increases as 1253 nm, 1265 nm, and 1282 nm for 0.02a, 0.04a, and 0.06a defect hole radii, respectively. The unexpected, slight change in defect resonance wavelength can be accounted for by the method in which the defect hole positions are generated. Since defect hole positions are found only for complete holes within a specified defect effective radius, the number of holes generated within the MHD region depends on the defect hole spacing and size. Although the ratio of defect hole size/spacing is constant, smaller holes and radii result in more defect holes being generated within the effective MHD radius, "filling out" the circle more efficiently. This explains the increased wavelength blueshift for in

Fig. 2.10a compared to Fig. 2.10b, since more holes are included at the edge of the effective MHD circle. This additional air contribution decreases the modal effective index slightly. Therefore, the defect hole generation method is only guaranteed to create equivalent effective index regions in the middle of the MHD region.

Quality Factor

Following the trend found in section 2.3.3, it is found that the quality factor is much higher for a smaller effective MHD radius photonic crystal, as shown in Fig. 2.11. While the change in quality factor due to defect hole index change is more linear in the 0.2a radius case, for an effective radius of 0.3a, the quality factor increases far more rapidly at higher dielectric constants. This is due to the overall faster change in effective defect dielectric constant. Conversely, there are fewer holes for the effective radius of 0.2a, which results in the linear trend. As explained at the end of the previous section, the differences in the quality factor of MHD photonic crystals with different defect hole sizes and spacing but the same defect effective radius and effective refractive index can be accounted for by the method of generating the defect hole positions within the defect effective radius.

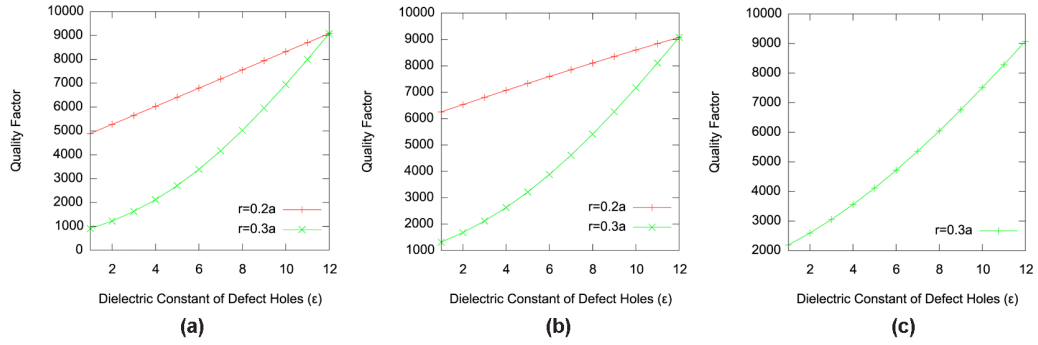

Figure 2.11: Quality factor of the H1 MHD for varied dielectric constant and defect hole radius/spacing: (a) radius 0.02a, spacing 0.06a, (b) radius 0.04a, spacing 0.12a, (c) radius 0.06a, spacing 0.18a.

The sensitivity or quality factor of the MHD PhCs, or a combination of the two param-

eters, can be chosen as the desired figure of merit depending on the intended application. The defect hole radius and spacing, along with the defect region effective radius, can be adjusted to tune the desired characteristics of the PhC. While high sensitivity may be advantageous for applications such as sensing, for other applications such as low threshold light emission, it may be more useful to have a cavity with higher quality factor.

2.3.5 Cavity Sensitivity

The enhanced surface area afforded by MHD photonic crystals, which allows strong interaction between the resonant photonic crystal mode and biomolecules attached inside the MHD holes, is extremely favorable for small molecule detection. To quantitatively demonstrate the advantage of MHD compared to SHD biosensors, the effect of adding a variable thickness monolayer of biomolecules on the defect hole walls of MHD and SHD photonic crystals is simulated. For sensing applications, chemical linkers are used to attach biomolecules to inorganic surfaces [56]. Thus, simulations can accurately model the addition of a uniform monolayer of a chemical linker, or approximate the addition of discrete molecules, such as DNA and proteins.

The simulated MHD cavity has an effective radius of $0.2\,a$, defect hole radius of $0.04\,a$, and defect hole spacing of $0.12\,a$. The SHD is specified with a radius of $0.2\,a$, such that the defect region of the SHD has the same footprint as the MHD. Fig. 2.12 shows the resonance frequency shift as a function of monolayer optical thickness of material added in the MHD and SHD. The Maxwell-Garnett approximation is used to calculate the effective refractive index for each defect hole containing the added monolayer of biomaterial [63]. Both defect configurations were assumed to be initially filled with air ($n = 1$), and all resonance shifts were measured relative to the calculated resonance of an empty structure of only silicon and air.

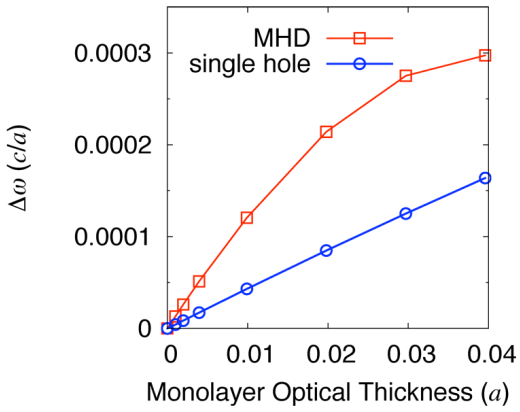

Figure 2.12: Plot of resonance shift as a function of monolayer optical thickness. The monolayer optical thickness is specified as a fraction of the photonic crystal lattice constant, a.

For monolayers thinner than the defect hole radius, the resonance frequency shift of MHD photonic crystals is approximately 3 times larger than that of SHD photonic crystals. Hence, the sensitivity of detection is clearly superior for the MHD structures. While the resonance shift is approximately linear with increasing monolayer thickness for thinner monolayers, the resonance shift of the MHD sensor tapers off as it approaches the condition of completely filling the defect holes. As the defect holes in the MHD become nearly filled with the monolayer, the change in effective index becomes smaller since there is increasingly less available surface area. The SHD sensor experiences a similar phenomenon near its complete filling condition when the monolayer optical thickness approaches $0.2\,a$.

Also notable is the difference in quality factor of the MHD and SHD sensors. The quality factor of the SHD sensor is 2.8×10^3, whereas the MHD sensor has a quality factor of 6.3×10^3 when the defect holes are filled with air. Higher quality factors correspond to sharper resonances in measured transmission spectra. Since narrower resonances facilitate the detection of small resonance frequency shifts, the larger cavity quality factor of the MHD sensors further enhances the detection capabilities of the MHD sensor compared to

the SHD sensor. The higher quality factor of the MHD can be explained in part due to the larger effective refractive index of the MHD, which results in stronger field confinement. For the same radius defect region, the MHD has index contributions from both air and silicon, while the SHD has an index contribution only from air. Additionally, the more abrupt index change at the boundary of the SHD contributes to scattering and loss, which reduce the quality factor.

2.4 Multiple-Hole Defects: L3 Cavities

The L3-type cavities, which are formed by filling in three air holes in a line, are well known for their high-Q and small mode volumes, which make them an ideal candidate for a LMI platform based on PhC. In an H1-type cavity, the amount of area available for defect hole placement is limited, and realistic fabrication tolerances make it difficult to fit more than a single hole. Conversely, the L3 has inherently more surface area for binding, which allows for more flexibility in the placement of defect holes. In the previous section, 2D FDTD simulations confirmed that H1 cavities with MHDs exhibit larger resonance shifts and, consequently, improved LMI and sensitivity for detecting analyte compared to PhCs with single hole defects (SHD). For practical applications, the dimensions of the defect holes in the H1 MHD cavity analysis are difficult to fabricate at high aspect ratios in silicon. Thus, compromises in the design must be made in terms of feasibility from a fabrication standpoint. When considering designs for L3 MHD cavities, a few issues must be addressed. First, 3D simulations are required to accurately model a device intended for fabrication. Since 3D simulations are resource and time-consuming, the overall design process must be well-planned. Second, the number of defect holes, their size, and their positioning are limited by the pattern writer resolution. Test patterns and dose arrays need to be run before the device simulations, in order to get an idea of realistically achievable

dimensions. Finally, the coupling mechanism to the cavity must be considered as part of the design, since light needs a pathway to the resonator. The next section describes simulations of L3 type cavities with defect holes and their design considerations.

2.4.1 Baseline L3 Cavity and Methods

Three-dimensional FDTD simulations were carried out in order to examine the effect of adding MHDs to an L3 cavity. All dimensions are normalized to the PhC lattice constant of $a = 410$ nm for cavity resonances in the range of 1550-1600 nm. The silicon slab forming the PhC is surrounded entirely by air, with a slab thickness of $0.536a$ (220 nm) and lattice hole diameter $0.512a$ (210 nm). The dielectric constant of the slab was set to $\varepsilon_{Si} = 11.56$, which can vary slightly in experimental settings. The L3 cavity itself consists of three filled in lattice holes, as shown in the inset of Fig. 2.13. The two lattice holes laterally adjacent to the cavity are moved outwards by $0.15a$ (62 nm) to increase the quality factor by relaxing the boundary conditions on the cavity mode Fourier transform [73]. The cavities are surrounded by 7 lattice rows in the Γ-M direction, and 10 rows in the M-K direction. The simulation resolution is set to 24 (grid points every a/24, or 17 nm) with subpixel averaging enabled to increase accuracy. The entire simulation space is surrounded by a perfectly matched layer (PML) of thickness $2.0a$, absorbing at the boundaries any fields emitted by the cavity. The resonance wavelength and quality factor of the cavities are calculated by placing a E_y-polarized dipole electric field point source with a Gaussian frequency distribution within the cavity, offset by $0.1a$ (41 nm) in the X and Y directions in order to avoid direct excitation of field maxima/minima. Assuming propagation in the plane of the cavity, with the wavevector k in the x-direction indicated in Fig. 2.13, the polarization can be considered *quasi*-TE. Overlapping the source and points of modal symmetry is avoided in order to excite all possible modes, if the symmetry of the cavity field distribution is not

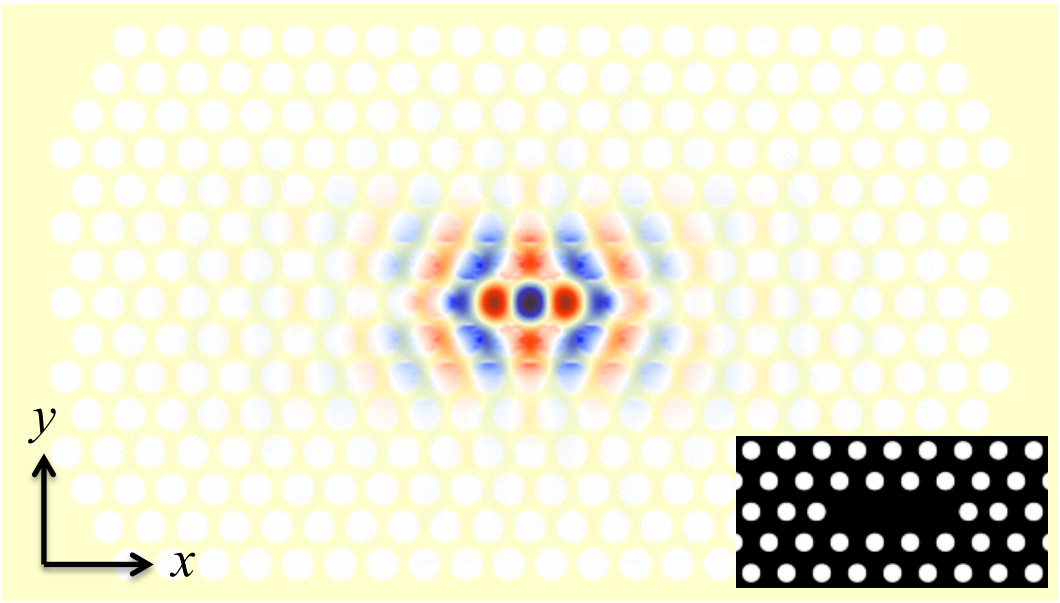

Figure 2.13: $z = 0$ cut of E_y field distribution overlaid onto dielectric function (yellow) for L3 cavity with lattice hole radius $0.256a$. Inset: detailed dielectric function in the cavity area.

already known. If the source dimension and placement closely matches the cavity mode, the number of modes excited is limited.

At time $t = 0$, the broadband pulse excites the cavity, and 1000 further time steps are computed after the source is turned off. The number of time steps is large to ensure that radiative slab modes and other non-resonant cavity modes have dissipated. The resonance wavelengths and quality factors of the remaining resonating modes are then computed by `harminv`, which decouples the fields into individual sinusoids and calculates their decay rates. For the baseline L3 cavity with no MHD, `harminv` gives an intrinsic cavity quality factor $Q = 25{,}300$ and $\omega = 0.266317\, c/a$. The normalized frequency of the cavity mode is equivalent to a wavelength of $a/\omega = 1539.5$ nm, and using Eqn. 1.6, the cavity lifetime $\tau = 20.66$ ps.

For optimizing refractive index perturbation using MHD, the regions of interest are the spatial locations within the modal field distribution with the highest intensity. These

locations can then be targeted for the addition of defect holes, in order to increase the spatial LMI. From the simulation results in Fig. 2.13, the L3 cavity has the highest field intensity in the middle of the L3 cavity, followed by two lateral intensities to either side of the center in the $\pm x$-directions.

2.4.2 Stationary Defect Hole Position

The baseline L3 cavity FDTD simulations showed that three main intensities exist within the modal field distribution. In parallel with cavity simulations, several test designs were fabricated using previously known parameters for L3 cavities and adding defect holes to the designs. The test design which became the basis for all future designs consisted of three defect holes located within the cavity with diameters ranging from 50-80 nm, spaced laterally by 470 nm from center. The spacing of 470 nm was initially chosen because of the lattice constant of 410 nm plus the added 60 nm of shift in the laterally adjacent lattice holes for increased Q. Simulations confirmed after fabrication had already begun, that the mode is actually compressed more towards the center. It was found with other test structures that the inclusion of more than three defect holes increased the scattering in the cavity significantly, making the resonance undetectable in the transmission. Therefore the number of defect holes in all designs was restricted to three. The characteristics of the fabricated MHD L3 test design were examined by simulation using the dimensions from the completed device.

The resulting cavity modes are shown in Fig. 2.14. The calculated resonance frequencies for the L3 cavity and MHD were 0.2626 c/a and 0.265 c/a respectively, corresponding to 1561 nm and 1547 nm for a lattice constant of 410 nm. The addition of defect holes filled with air lowers the modal index and blue-shifts the resonance. Examination of Fig. 2.14(a-b) shows similar in-plane mode profiles for both cavities, with three main lobes inside the

cavity region. Fig. 2.14(c-d) shows the plotted field amplitude for each cavity using a vertical cut through the slab center, with the matching field profile plot overlaid for reference. It is important to note that the field amplitude is continuous in the MHD, with the highest positive field directly overlapping with the central defect hole, lowest negative field at the lateral defect holes, and no loss of intensity at the defect holes. The sharp field increase inside the defect holes results in a perceived offset in field intensity between the MHD and L3 cavities after normalization to the color map scale. However, the field amplitude in the MHD cavity is in fact comparable to that in the L3 cavity. The calculated intrinsic cavity Q

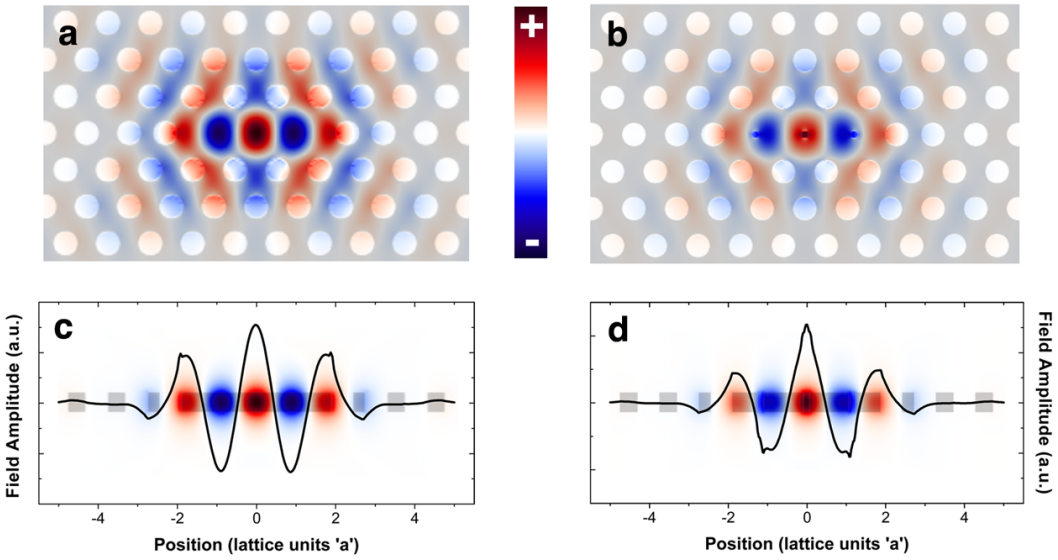

Figure 2.14: Cavity mode TE field profiles from FDTD analysis overlaid onto the in-plane dielectric structure for (a) L3 and (b) 3-hole MHD cavities, with their respective vertical cuts and overlaid field amplitude data shown in (c,d).

values are ∼27,000 for the L3 cavity, and ∼24,000 for the MHD cavity. We note that these Q values are in good agreement with those reported for similarly designed L3 cavities [73]. The values of Q are slightly different from those of section 2.4.1 due to a corrected dielectric constant of $\varepsilon_{Si} = 11.9$, from fitting to experimental results, as will be shown in Chapter 3. While higher intrinsic Q can be achieved through further optimization of the lattice hole

positioning around the cavity [74], ultra-high Q factors can introduce increased sensitivity to environmental changes, which can be problematic for sensor applications. The slight degradation of Q after insertion of the three MHD holes is likely caused by scattering occurring at the silicon/defect hole interfaces. Since the field is most strongly concentrated in the regions of additional surface area, inside the defect holes, analyte that binds to the silicon surface can be detected directly inside the volume where the modal field intensity is highest.

2.4.3 Design Optimization

The first MHD L3 test design was not optimized for the cavity mode, because test structures were fabricated in parallel with simulation. Once the mode distribution is known, the spatial aspect of the LMI can be tuned further by changing the placement of the holes. The goal is to optimize the cavity to a design where the cavity Q is not severely degraded, and the largest perturbation of the resonance position is achieved. By simulating L3 MHD cavities with differing lateral defect hole spacings, the effect of fractional overlap between the modal field and the defect holes can be investigated. The magnitude of the measured transmission resonance shift for L3 MHD cavities with different lateral defect hole locations is a relative indication of the sensitivity of the LMI to perturbations for each design. Several cavities are simulated, with the lateral spacing (here referred to as 'd') of the 60 nm diameter defect holes increased in 40 nm increments, starting from 100 nm and ending at 500 nm. The defect holes are always arranged in a straight line which bisects the cavity lengthwise, and d is measured as the lateral distance going away from cavity center. The dielectric constant was set at $\varepsilon = 11.56$ for these simulations.

First, the resonance shift due to defect hole placement is examined, which is plotted in the black points shown in Fig. 2.15. The resonance wavelength of the L3 cavity without

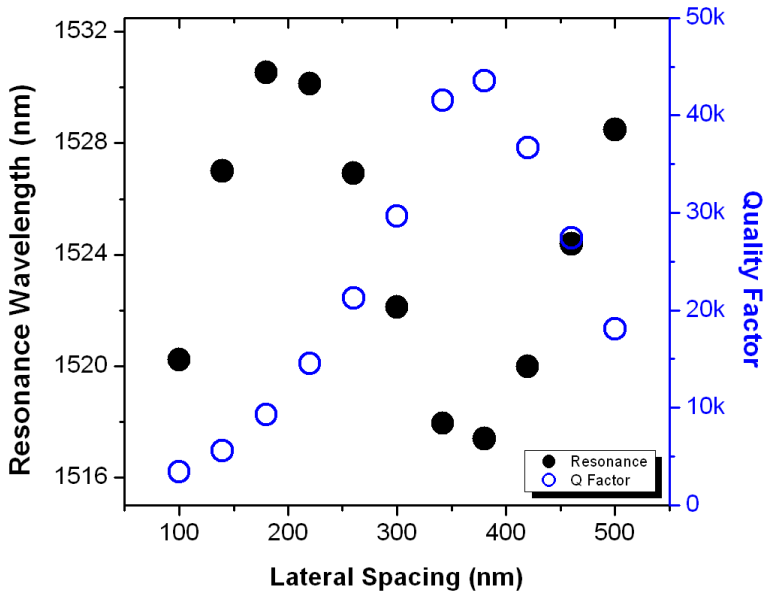

Figure 2.15: Simulated resonance wavelength (black, filled circles) and quality factor (blue, open circles) for various lateral spacings of side defect holes in the 3-hole MHD cavity.

any defect holes is 1539.5 nm, above the y-axis of the plot. The resonances of the L3 MHD cavities are all shifted to shorter wavelengths compared to the L3 cavity resonance, and the degree of shift from the baseline L3 cavity corresponds to a larger degree of LMI. Recall that the spatial overlap of the defect hole and modal field intensity comprises the amount of perturbation to the L3 cavity, and thus the sensitivity of the resonance wavelength to perturbation increases when LMI increases. Starting from the lateral spacing of 180 nm, with increasing lateral hole spacing the defect holes cross over the zero field points in the modal field, and begin to overlap with the secondary intensities. As the spacing approaches 380 nm, the resonance increasingly blue-shifts away from the L3 baseline resonance wavelength, and LMI is maximized for the lateral hole spacing of 380 nm. Beyond 380 nm, the holes pass the location with maximum intensity and the degree of LMI is reduced, causing the resonance to shift back towards the L3 cavity baseline value. For completeness, lateral spacings of 100 and 140 nm were also simulated. At these spacings, the resonance

blue-shift again increases relative to the L3 baseline resonance wavelength, this time due to the overlap with the central intensity lobe of the mode. It is found that the smallest lateral defect hole spacing (100 nm) and an intermediate spacing of 380 nm produce the largest shifts. This shows that the degree of the LMI due to defect hole overlap with modal regions of high intensity does indeed correlate to an increased sensitivity. Furthermore, as the holes cross over the zero-intensity points at 180 nm and 500 nm, the sensitivity is found to be minimized. The ideal MHD cavity design, therefore, should have defect holes placed at $d = 100$ nm or $d = 380$ nm, which causes the largest resonance shifts.

However, the cavity Q should be considered as well for a fully optimized design. The blue, open circled points in Fig. 2.15 show the Q values for the respective lateral spacings of the defect holes in the L3 MHD cavities. For reference, the Q of the baseline L3 cavity is 27,000. While two lateral spacings were found to maximize the resonance shift, the maximum value of Q exists only at the $d = 380$ nm design. The other hole location which leads to largest resonance shift, $d = 100$ nm, has a value of Q which is drastically reduced to around 3,000, nearly an order of magnitude lower than the baseline L3 cavity Q. There are two important observations to make here. First, the value of the maximized Q for the L3 MHD cavity with lateral defect hole spacing of 380 nm is over 43,000, which is higher than the Q of the L3 cavity without any MHD defect holes (27,000). This can be explained by the so-called "slot waveguide effect," which is the concentration of field in narrow, low index regions due to the discontinuity of the electric field at high contrast dielectric interfaces [75]. Positioning the defect holes precisely at the field maxima can potentially intensify the field inside of the defect holes, creating higher Q resonances.

Second, the drastic reduction in Q for the $d = 100$ nm spacing can be associated with the formation of singular regions of lower effective index when the spacing between defect holes becomes too small. Consider the case where the defect holes are spaced apart

by an amount larger than the diameter of the holes themselves. In this case, the holes are surrounded by enough high-index material that the sum of the individual low-index contributions is minimized. The result is a slight overall lowering of the effective index in the entire cavity, with minimal scattering. When the spacing between the holes approaches the order of the hole diameter (in this case $\sim$60 nm), the small region containing 3 holes contributes a more significant lowering of the effective index. This can be likened to the 3 holes combining into an oblong-shaped low index region in the cavity. Hence, the intention of minimizing low-index contributions is destroyed, and the effective-index approximation cannot be applied, creating a significant source of scattering losses in the cavity. A similar trend is seen in the 2D FDTD simulations of the H1 PhC cavities in section 2.3.3, where the Q is reduced as the effective MHD region is enlarged. The limitation of the simulation resolution can also be a factor when the defect hole spacing becomes too small. If only a small amount of material is left separating the holes, it is possible that the index contrast cannot be resolved with the FDTD grid spacing. However, for the case of 100 nm lateral spacing and higher, sufficient grid points are available to resolve the separation.

In summary, the spatial aspect of the light matter interaction can be improved by the integration of defect holes within a L3 cavity. The amount of overlap between the defect holes and the cavity field dictates the amount of shift in the resonance, and indicates the presence of a location where maximum perturbation occurs. The reduction of Q with crowding of defect holes is verified in experiment results and will be addressed in Chapter 3.

CHAPTER 3

MULTIPLE-HOLE DEFECT FABRICATION AND MEASUREMENT

3.1 Design Rules

The design rules used to set the various dimensions of the PhCs are restricted by the measurable range of wavelengths by the available sources/detectors, material absorption/transparency, and polarization considerations. In the sections below, we outline the acceptable ranges of device dimensions and their impact on device performance.

3.1.1 Substrate and Waveguide Design

For fabrication of nanophotonic devices on a silicon platform, silicon-on-insulator (SOI) wafers, which consist of a thin silicon device layer on top of a buried silicon dioxide layer, are an optimal choice of substrate. The buried oxide (BOX) serves to optically isolate the guided modes from the bulk wafer below, and must be at least 1 μm thick. SOI wafers from SOITEC with a 220 nm-thick device layer and a BOX thickness of 2 μm are used for all of the measured devices. The chosen device layer thickness helps to suppress TM mode propagation in the 500 nm-wide single mode access waveguides at longer wavelengths. Device operation above the cutoff (the wavelength above which a mode is no longer supported) of the first TM mode is desirable; the cutoff wavelength is a function of the waveguide width and thickness [76].

The overall layout of the devices on chip is as follows. PhC device regions and W1 waveguides are placed in the middle of the chip in a linear fashion, to ease observation of scattered surface light. Devices are grouped according to similar types of designs. Baseline L3 cavity devices are offset from other devices in order to differentiate them easily in the

microscope view. Strip waveguides extend out from the W1 coupling waveguide for each device and bring the signal to the edges of the $\sim$1 cm long chip for measurement. Two tapered sections are employed in the strip waveguides in order to reduce coupling losses. First, at the edge of the chip the waveguides inversely taper down to a width of 200 nm over a length of 300 µm to facilitate mode-matching to fibers during measurement. Coupling using only the nanotapers, however, requires polishing down the excess length of substrate in order to bring the tapers closer to the chip edge [77]. Because the polishing process can potentially damage and/or contaminate devices, polymer spot size converters are employed on the PhC MHD chips to increase coupling efficiency to the devices [27]. These consist of straight polymer waveguides with a cross section of approximately 3x2 µm which are deposited directly over the 200 nm silicon waveguide nanotapers. The increased size of the polymer waveguides allows for a better match with the tapered lensed fibers, which have a spot size of approximately 2.5 µm. Light is then gradually coupled into the silicon strip waveguides along the overlapped portion. The 2.3 mm long polymer couplers accommodate a large amount of error for device cleaving. Second, as the strip waveguide approaches the PhC region, the width is tapered out to 710 nm, which matches the distance between the two lattice holes on either side of the W1 coupling waveguides. The termination plane of the PhC lattice at the interface is also important, and has an effect on the insertion losses due to reflection [78]. Therefore the strip waveguide meets the PhC W1 waveguide at a distance of $0.75a$ into the lattice in order to minimize losses, which corresponds to one quarter of the lattice constant beyond the last lattice hole plane.

3.1.2 Photonic Crystal Design Parameters

The lattice constant in the photonic crystal is the most critical design parameter. The choice of lattice constant determines the frequency range of the bandgap, and subsequently, the

low-loss guiding region of the W1 PhC waveguides. The infrared C-band (1.53-1.57 μm), which is commonly used in fiber-optic communications links, is a good choice for silicon photonics applications as well, due to silicon's transparency in this range and readily available sources and detectors [41, 73]. In order for the bandgap to fall within the C-band, the lattice constant must be in the range of 400-420 nm.

For the PhC designs in this thesis, a lattice constant of 410 nm is chosen. Choosing a larger lattice hole size relative to the spacing (r/a ratio) results in increasing and shifting the spectral width of the bandgap, translating to a wavelength blueshift in all spectral features. W1 waveguides with this lattice constant have a cutoff occurring around 1600 nm. In the case of PhC waveguides, cutoff occurs due to the forbidden bandgap, whereas in strip waveguides the cutoff is due to the dimensions of the waveguide no longer able to support a mode. With the lattice constant fixed, the relative sizes of the defect holes are restricted on the lower limit due to fabrication limitations. At the larger limit, the defect hole must be smaller/larger than the lattice hole, but unequal to the lattice hole size. When creating a defect hole of size larger than the lattice holes, modification of the surrounding lattice holes may be necessary to prevent hole overlap. For sensor applications, the number of defect holes and layout of the MHD should be chosen by taking into consideration the type of analyte to sense. Detection of small molecules may require pushing the boundaries of lithography critical dimension (CD), while larger molecules may have more relaxed tolerances for fabrication. This is due to the size-specific filtering inherent in fabricating holes of a certain size, as well as the necessity to fill as much of the hole surface as possible for efficient light matter interaction. Fabricating defect holes which are too large for the molecules or particles of interest reduces the efficiency of filling due to an excess fraction of air inside the holes.

In this thesis, several designs of MHD cavities are fabricated on-chip, with variations

in defect hole position, radius, and spacing. These parameters are modulated in order to explore the relationships between different designs and the resulting cavity sensitivity and quality factor. Strip waveguides and PhC W1 waveguides are also fabricated for transmission normalization and lattice characterization purposes, respectively. Normalized transmission measurements report the relative transmission with respect to the strip waveguide, by dividing all traces by the strip waveguide data. The W1 waveguide serves as a guide towards PhC characterization due to the cutoff wavelength being affected by the lattice hole size. Measuring the cutoff and the quality of the low-loss propagation spectrum in the W1 waveguides gives an indication of the lattice hole uniformity and size.

3.2 Device Fabrication

Although an advantage of MHD PhC devices is the compatibility with well-known CMOS silicon processing techniques, several challenges exist for creating uniform, sub-wavelength sized features within a lattice that requires uniform hole radii and spacing. In this section, several fabrication challenges and their solutions are presented, as well as details outlining each step of the fabrication process.

3.2.1 EBL Challenges

In order to create small features with high resolution in the MHD PhC devices, electron-beam lithography (EBL) must be utilized in the patterning step. Typically, modern EBL tools are capable of producing features less than 10 nm in diameter with process optimization. One of the main challenges to achieving closely spaced small features using EBL is the so-called "proximity effect," which has been previously reported in the literature [79, 80]. Proximity effect is especially severe at high acceleration voltages, which are required to achieve high resolution features due to the directionality of the focused beam.

Electron backscatter from underneath the resist can over-dose the surrounding patterns in the MHD structures, resulting in non-uniform lattices. This effect can be seen in Fig. 3.1, which shows the result of a photonic crystal waveguide pattern written with EBL at a single dose. The lattice holes are generally under-dosed, resulting in patches of holes that are not properly exposed. The improperly exposed holes occur in a seemingly random fashion, due to the nature of electron backscattering from the substrate. The holes near the strip waveguide interfaces at the input/outputs tend to be well-resolved due to an added indirect exposure from the adjacent large area features. Conversely, holes towards the bottom and top edges of the pattern are nearly non-existent due to less proximity effect at these locations. In order to overcome these patterning errors, compensation is performed in all subsequently fabricated devices by self-biasing the dose of individual shapes during pattern editing or by using automated Proximity Error Correction (PEC) to modulate the exposure dose depending on the feature positioning throughout the pattern layer. When using dose biasing, the defect holes within the MHD region generally require a dose that is 200-300% increased with respect to the base dose. This is due to the EBL pattern generation process, which translates the design from a GDS-II layout type to a EBL tool-specific format by filling the patterns with equally-spaced "shots." Each shot represents one location at which the electron beam will be held stationary, and the dwell time at each spot is dependent on the dose. Because the 40-60 nm defect holes only contain a few shots, the beam must be held there for much longer in order to fully expose the resist.

3.2.2 Fabrication Steps

The fabrication process steps for the PhC MHD sensor devices are outlined in Fig. 3.2. Devices were fabricated at the Center for Nanophase Material Sciences at Oak Ridge National Laboratory, Oak Ridge, TN for exploratory and design purposes, and at the Microelectron-

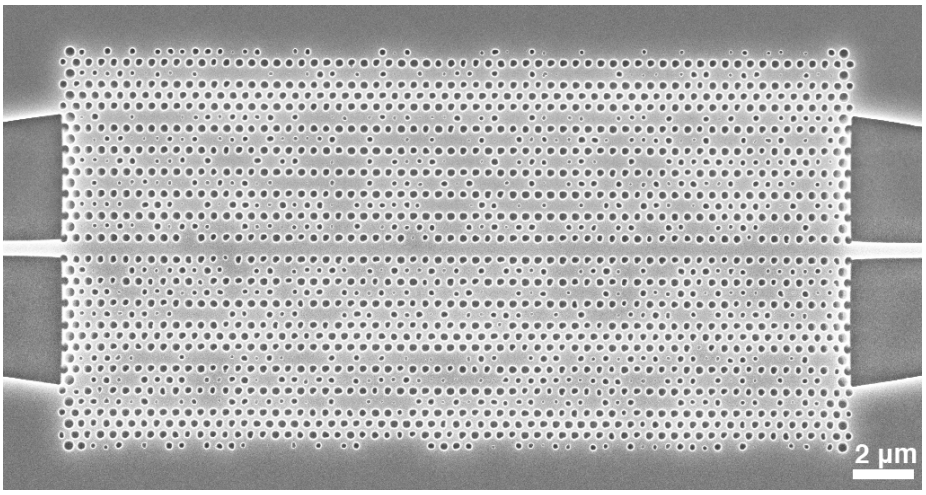

Figure 3.1: Pattern errors in photonic crystal waveguide patterned using electron-beam lithography without proximity error correction or dose biasing.

ics Research Laboratory (MRL) at IBM T. J. Watson Research Center in Yorktown Heights, NY for experiments. The devices fabricated at IBM were processed on a standard 200 mm CMOS fab line. Two differences exist in the processes used at each facility, which are the e-beam resist used (CNMS: ZEP-520A, MRL: PMMA) and the use of an oxide hard mask layer only at MRL. The oxide hard mask is required when using PMMA due to its poor etch selectivity. All patterns were laid out by hand in the GDS-II format using Tanner L-Edit or IBM's proprietary layout software.

The following description is for the devices fabricated at MRL. First, a 50 nm-thick oxide hard mask layer is deposited by LPCVD on a silicon-on-insulator (SOI) substrate with 220 nm silicon device layer thickness and 2 µm buried oxide (BOX) layer. PMMA resist is spin-coated onto the hard mask surface, and a Leica VB6-HR 100 kV electron beam lithography system is used to expose the PhC regions and access waveguides in a single step. The oxide mask and silicon device layers are then etched using a two-step RIE, with CF_4/CHF_3/Ar and HBr chemistries, respectively. After the resist is stripped, polymer mode couplers were fabricated using spun on negative resist (SU-8) and aligned

lithography on top of the tapered bus waveguides.

Once the devices and polymer couplers are defined at IBM, the final processing steps are required to create the air bridge structures necessary for symmetric air/silicon/air slabs are performed at the Vanderbilt Institute of Nanoscale Science and Engineering (VINSE) cleanroom. The symmetric vertical structure in the photonic crystal slab is important for opening the photonic bandgap in the plane, as discussed in Section 1.2.4. The removal process of the oxide underneath the PhC slabs is referred to as the "undercut" process. For the undercut step, Shipley 1813 photoresist is first spin-coated at 3000 rpm onto the samples and then windows in the photoresist are opened over the PhC device regions only via optical lithography. The lithography step is carried out as follows. An iron oxide optical mask, which is semi-transparent in the visible wavelengths for ease of alignment, was designed in-house and sent out for fabrication. The masked sample is exposed to a dual-source (*g* and *i*-line) UV light for 8 seconds in hard-contact mode on a Karl Suss MA6 mask aligner. After exposure, the sample is developed in a TMAH-based solution (AZ-300 MIF) for 30 seconds, rinsed with DI water, and dried with nitrogen gas. The underlying BOX was then etched away using a 9:1 buffered oxide etch (BOE). The BOE solution is drop-casted onto the chips for 3 steps of 10 minutes each and 1 additional step of 5 minutes, rinsing with DI water and drying with nitrogen in between each step, forming air-bridge PhCs with air cladding above and below the devices.

After the BOX undercut, the samples are cleaved through the polymer couplers. The undercut resist mask that remains in the region outside the PhC is retained in this step to protect the waveguide surfaces from any contamination during the cleaving process. Cleaving through the waveguides provides a clean edge to minimize reflections and facilitate efficient coupling of light to and from the PhC chip. Finally, the resist layer is removed by a 10 minute soak in acetone, rinsed with acetone and isopropyl alcohol, and dried with

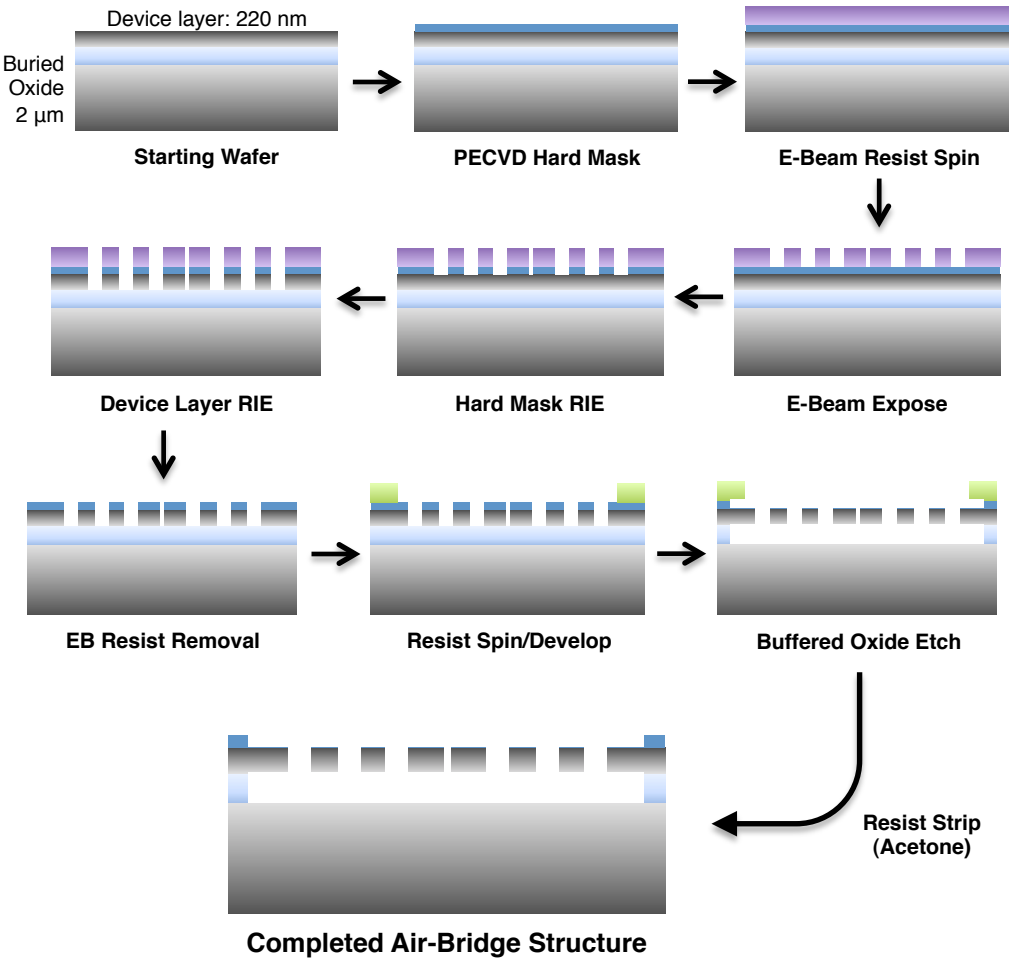

Figure 3.2: Fabrication steps for the multiple-hole defect photonic crystal structures.

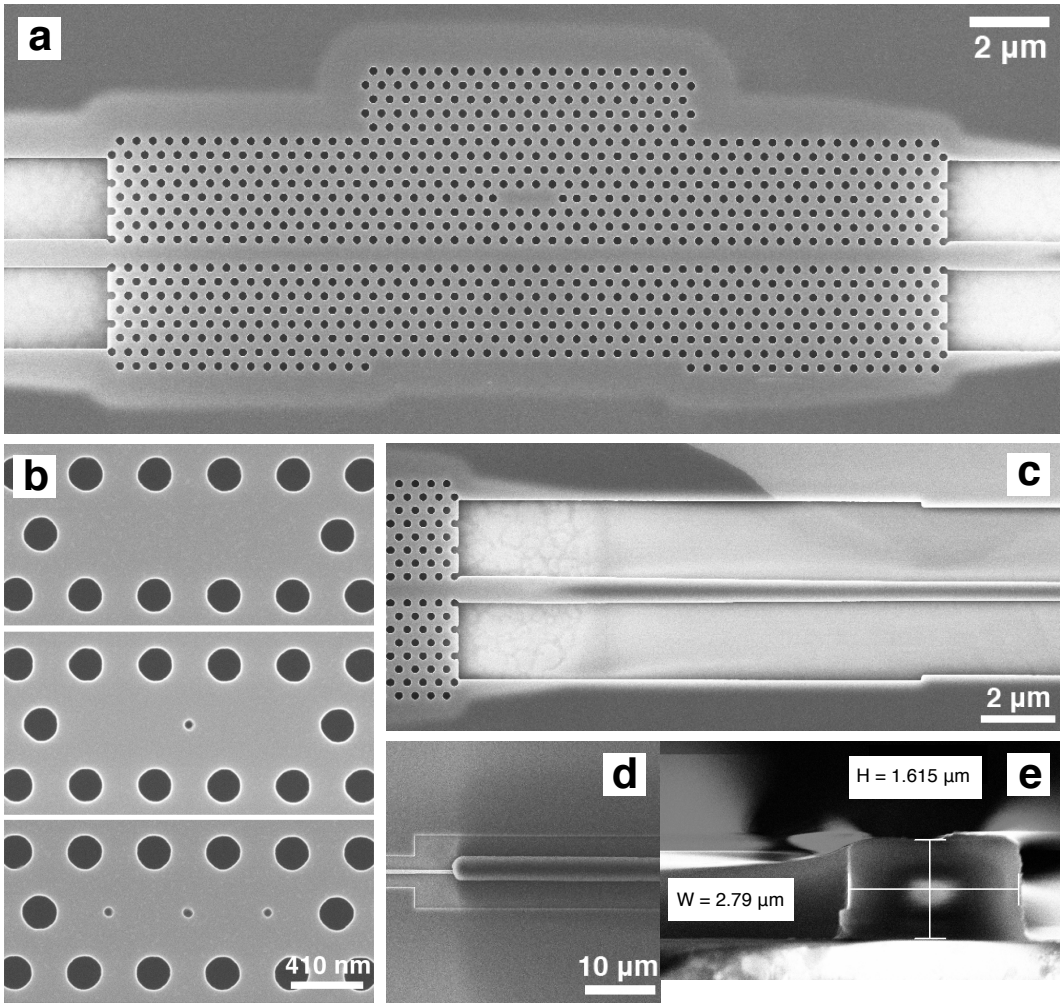

Figure 3.3: SEM micrographs of fabricated MHD PhC devices, showing (a) overall device region showing strip waveguide input/outputs and W1 waveguide coupling to PhC L3 cavity, (b) close-up inspection of (top to bottom): L3 cavity, SHD cavity, 3-hole MHD cavity, (c) strip waveguide tapering to match W1 PhC waveguide width, (d) SU-8 polymer coupler and (e) coupler cross-section.

nitrogen. SEM images of the completed devices are shown in Fig. 3.3. Variation of the base dose in the EBL write step produce PhC lattice holes between 200-220 nm in diameter, and MHD with defect holes between 50-90 nm in diameter.

3.3 Measurement Setup

The optical measurement setup used to characterize the PhCs is shown schematically in Fig. 3.4, and a photo of the setup is shown in Fig. 3.5. The photonic chips are mounted on a brass sample carrier fabricated in-house, which sits on a Y-Z stage for positioning. Tapered, polarization-maintaining fibers with $2.5\pm0.5\,\mu$m spot size and $14\pm2\,\mu$m working distance couple light in/out of the device. The fibers are aligned on either side of the chip and mounted on XYZ stages with piezo controlled actuators for accurate positioning. A broadband LED source (Agilent 83437A) with FC/PC fiber output provides an input spectrum ranging from 1200-1700 nm, suitable for the designed wavelength ranges of interest. A polarization stage before the input tapered fiber selects the TE or TM polarization, and all fibers are polarization-maintaining. The transmission spectrum of the PhCs is measured by an optical spectrum analyzer (OSA, Agilent 86140B); resonances of the MHD devices within the excitation bandwidth can be observed. All transmission spectra are normalized to a single-mode strip waveguide that is measured separately using the same optical measurement setup. For measurements which require higher spectral resolution, a germanium detector and optical power meter are used with tunable diode lasers (NewFocus Velocity) to scan from 1470-1570 nm with 0.01 nm resolution. As shown in Fig. 3.5, a NIR-transparent 20x microscope objective with long working distance (Mitutoyo) is positioned directly above the sample to assist with coupling and alignment. An IR-sensitive InGaAs sensor camera (Sensors Unlimited SU320M) is used to collect the image, which can be viewed on a monitor via a BNC cable connection.

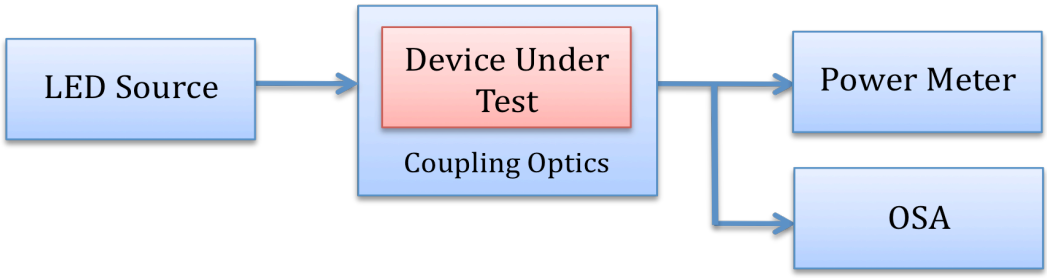

Figure 3.4: Illustration of PhC measurement system.

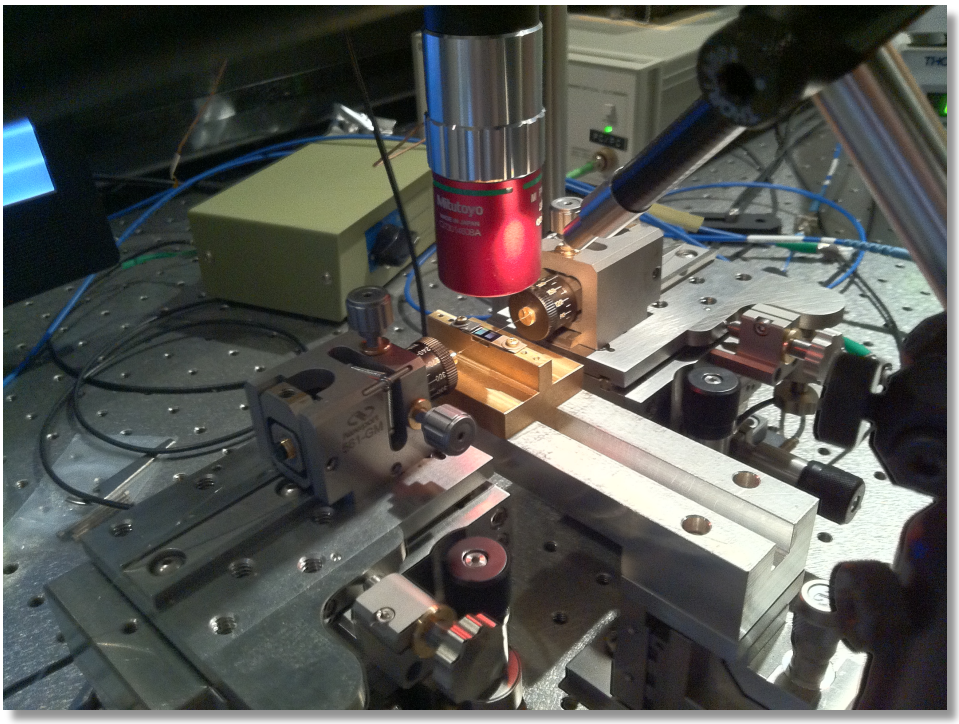

Figure 3.5: Measurement showing device under test (DUT) and input/output fibers. A microscope objective optimized for near-infrared transmission is used for observation above the DUT.

3.4 Passive Device Characterization

Before the effect of surface perturbations is explored in Chapter 4, passive device measurements are conducted and presented here to confirm the simulated device properties such as waveguide cutoff, quality factor, and sensitivity to defect hole placement. The transmission spectrum of the fabricated cavities is measured in air ambient.

3.4.1 Photonic Crystal Waveguides

As discussed in Chapter 1, PhC W1 waveguides possess a low-loss guiding region which can be calculated using PWE simulations (`mpb`). For the purposes of coupling to PhC defects, the bandwidth of the low-loss guiding region must overlap with the cavity mode resonance frequency to ensure that light is guided in and out of the structure. The spectral overlap can be verified by first simulating with `mpb` using the fabricated dimensions measured by SEM, to find the low-loss region. By then simulating an L3 cavity with the same lattice parameters, it is found that the resonance frequency of the L3 cavity is located close to the cutoff of the W1 waveguides. Therefore, the cutoff wavelength of the W1 waveguides alone can be measured first to ensure that the cavity resonances are located within the measurable range of the available sources and detectors. Also, measuring W1 waveguides without adjacent cavities helps to characterize the quality of the fabricated lattice holes and their size, which directly affects the cutoff wavelength. Because the fabrication process can result in a narrow spread in the lattice hole size/spacing, the effective lattice size is reflected in the location of the W1 cutoff. The location of the W1 cutoff is confirmed by PWE simulations in `mpb`, where the measured parameters from the fabricated devices are inputted as normalized dimensions. Fig. 3.6 shows normalized transmission spectra of 3 different lattice hole sizes, achieved by simply modulating the EBL exposure dose. As expected,

the waveguide cutoff blue-shifts with increasing dose, as the bandgap is pushed to higher frequencies for larger hole radius relative to a. Increasing the size of the lattice holes can be considered as effectively removing a thin layer of material from the inside of the holes, which reduces the effective index of the hole and shifts the bands to higher energies (lower wavelengths). Adding material, or effectively shrinking the lattice radii, results a shift to lower energy (higher wavelengths). Note that although the band edge shifts demonstrated here are due to permanent changes to the lattice hole dimensions, the same concept applies for active sensing applications when chemical or biological material is added to the lattice holes, which will shift the waveguide cutoff by an amount proportional to the effective refractive index change induced by the presence of the target material.

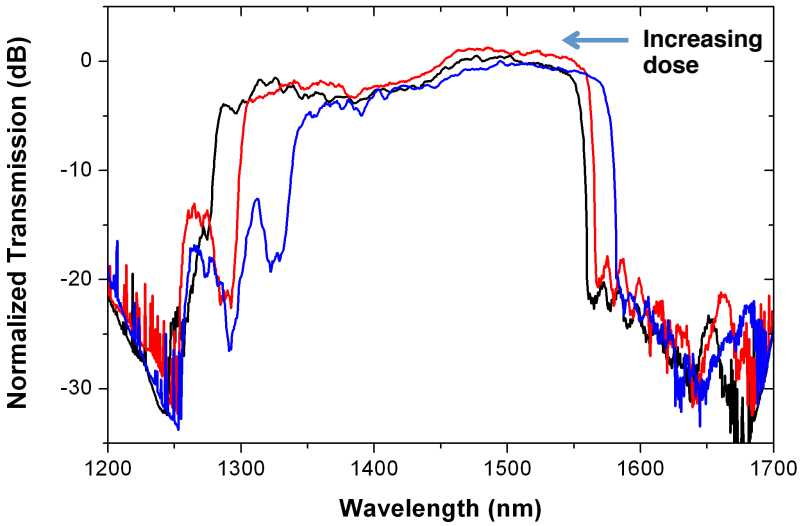

Figure 3.6: Transmission of W1 PhC waveguide for varying EBL lithography dose.

The comparison of measured transmission and calculated bands is shown in Fig. 3.7. In order to align the spectral features, the x-axis for the measured transmission wavelength is reversed, and the bands are plotted with the x and y-axes inverted (wave vector as the y-axis, mode frequency as the x-axis). Several important points are circled in red and labeled (a-d) in the figure. The region between points (a) and (b) is the cutoff due to the mode gap which

occurs between the guiding states above (b) and the extended states at (a). This causes the sharp cutoff in transmission above 1580 nm. Points (b) and (c) in Fig. 3.7 are the cutoff and multi-mode frequencies, respectively. Between these points is the low-loss guiding region, which corresponds to the highest measured transmission in Fig. 3.7, occurring in the region from approximately 1500-1580 nm. Between (c) and (d), where the extended modes meet the light line, transmission is reduced due to the increased density of states both in the gap and above the light line (gray region). Point (d) represents another cutoff due to the light

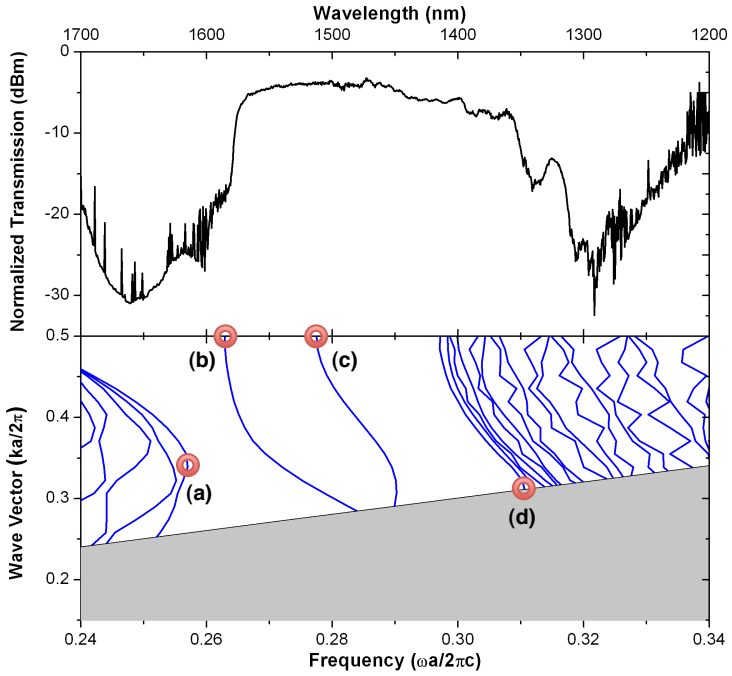

Figure 3.7: Comparison of W1 measured waveguide transmission to dispersion calculated by `mpb`. The gray region is the light cone, where modes are radiated and not guided. Special points (a-d) correspond to: (a) onset of extended modes, (b) mode gap cutoff frequency, (c) onset of multi-mode guiding, and (d) light line cutoff.

line, which is represented by a drop off in transmission at 1350 nm. Because the L3 cavity modes are close to the W1 cutoff wavelength, the W1 transmission measurements confirm that the cavities will be in the range of the high-resolution tunable laser source, which is limited to 1470-1570 nm.

3.4.2 Effect of Defect Hole Size

As discussed in the previous section, modulating the radius of the PhC lattice holes has the effect of changing the sensitivity of the slab to surface perturbations. A similar effect occurs for the small MHD holes fabricated within an L3 cavity: changing the radius of the defect hole will shift the defect resonance frequency within the band gap. Note that at the resonance wavelength, the modal field is mostly confined to the defect region, so the spatial overlap is increased for the defect holes compared to the lattice holes. In order to experimentally verify the resonance shift for modulated defect hole radius, several different L3 PhC cavities with defect hole diameters were designed and fabricated. All cavities were fabricated on the same chip. The as-designed dimensions are slightly different from the defect hole radii measured by SEM, likely due to dose biasing, PEC effects, and variability in reactive ion etching. For example, designs with defect hole diameters of 30, 50, 70 nm in the pattern are fabricated as 57.1, 57.4, and 69.1 nm diameter holes, respectively, in the SHD, and as 53.5, 54.6, 71.1 nm respectively, for the MHD cavities. The defect hole diameters measured by SEM metrology, and are assumed to be accurate within 5 nm. Note that the MHD designs consisted of three holes, with the side defect holes placed at a constant lateral spacing of 470 nm from the center defect hole that was located in the middle of the L3 cavity. The measured resonances in the transmission spectrum are shown in Fig. 3.8 for SHD and MHD designs with nominal defect hole diameters of 30, 50, and 70 nm, as well as two baseline L3 cavities with no defect holes.

The magnitude of the relative resonance shifts for L3 cavities with the same lattice hole diameter and different defect hole diameters is directly proportional to the defect hole diameter. When the defect hole diameter is increased, the effective index of the cavity mode accordingly decreases, which leads to the resonance wavelength blue-shift. The magnitude

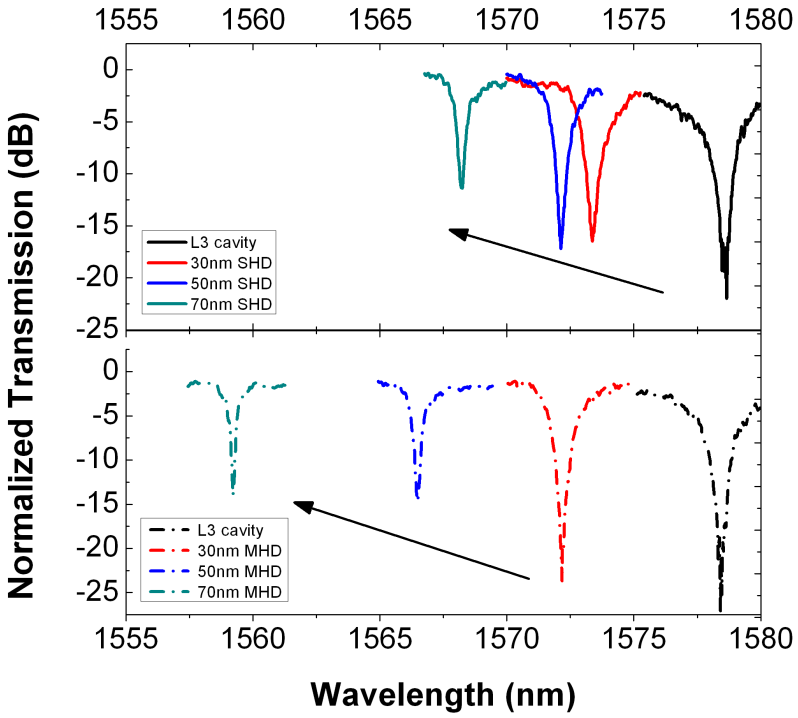

Figure 3.8: Comparison of cavity resonances for same as-designed sizes of defect holes for SHD (top) and MHD (bottom).

of the blue-shift of the MHD resonances is greater compared to the SHD cavities with the same as-designed defect hole sizes because more of the overall cavity index changes as material is removed from the inner surface of the defect hole. Conversely, when material is added to the inner surface of each defect hole, the MHD should have a larger red-shift when compared to a SHD or L3 cavity. Thus, the passive measurements for hole radius modulation are an indication of the potential sensitivity of the PhC to surface perturbations.

Fig. 3.9a shows measured resonances for a solid L3 cavity, as well as for SHD and MHD cavities with defect hole diameters of 57 nm and 54 nm, respectively. It should be noted that the trend of resonance shift due to defect hole size modulation follows that of FDTD simulations which utilize the dimensions of the fabricated devices. The addition of a single defect hole (SHD) blue-shifts the L3 resonance by 6.46 nm; the MHD cavity resonance is blue-shifted by 11.94 nm compared to the L3 resonance. Based on multiple measurements and Lorentzian curve fitting, we estimate the precision of the cavity resonance wavelength measurements to be 0.003 nm. Lorentzian curve fits were also used to extract the "loaded" Q (Q_{load}) of each resonance by calculating $\lambda_0/\Delta\lambda$. Q_{load} is a measurable quantity, which is degraded from the intrinsic Q found in simulation due to waveguide leakage. We found a similar Q_{load} of 6500$\pm$200 for the different cavity configurations. We note that the blue-shift of the resonance after addition of defect holes and the similarity of the Q_{load} among all three cavity configurations is expected from our simulation results in 2.4.2.

Here it is emphasized that the measurable quantity Q_{load} is lower than the intrinsic, simulated Q (Q_{intr}) as a result of two loss factors: (1) losses associated with fabrication errors, and (2) the bus waveguide coupling loss. Both of these are related by an "experimental" Q (Q_{exp}), which can be calculated from Q_{load} by the minimum transmittance at resonance T_0 as described by Eqn. 3.1. The losses due to fabrication (Q_{loss}) in Eqn. 3.2 result from inaccuracies in lattice hole radius and uniformity, as well as any surface roughness that results

from etching processes. Q_{loss} can be reduced by rigorous process engineering, but this is costly from a time and monetary standpoint [42]. The loss due to coupling is a function of the separation between cavity and waveguide. As shown in Fig. 3.3, all of the designed cavities are separated from the access PhC waveguides by 3 rows of lattice holes. A trade-off must be taken into consideration when designing the cavity-waveguide system. Placing the cavity too close will reduce the Q_{load} due to light leakage to the waveguide, and placing the cavity too far away will reduce the dropped signal in the transmission, making it hard to resolve the resonance even though Q_{load} is high. The measured Q_{load} for the PhC reported in this chapter is suitable for sensing small molecules, as will be discussed in Chapter 5.

$$Q_{exp} = Q_{load}/\sqrt{T_0} \tag{3.1}$$

$$\frac{1}{Q_{exp}} = \frac{1}{Q_{intr}} + \frac{1}{Q_{loss}} \tag{3.2}$$

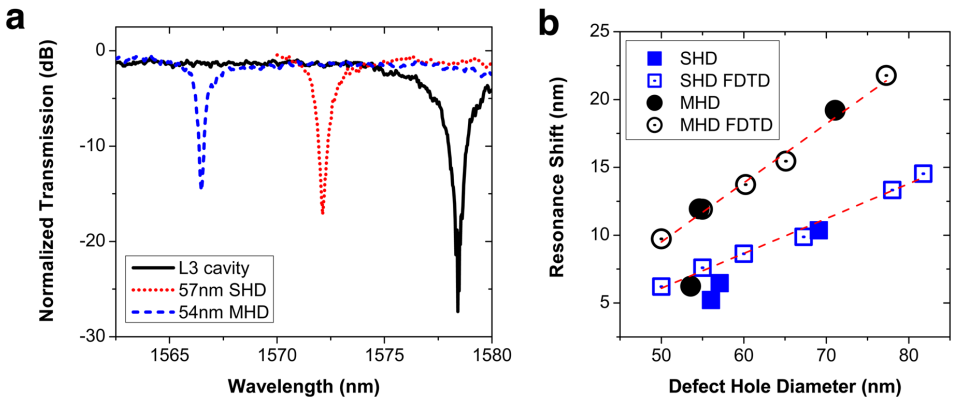

Figure 3.9: (a) Transmission spectra comparing the resonance of an L3 cavity (solid) to those of SHD (dotted) and MHD (dashed) cavities with similar defect hole diameter, (b) Resonance shift relative to L3 cavity for SHD and MHD cavities as a function of defect hole diameter. Measured results are shown as solid squares/circles (SHD/MHD), data from FDTD simulations are shown in open squares/circles, and a linear fit (dashed line) is provided as a guide to the eye.

A summary of the resonance shifts for SHD and MHD cavities with different defect hole diameters is shown in Fig. 3.9b. FDTD simulations were performed on cavities with similar defect hole diameters, and these data are also shown in Fig. 3.9b. The experimental and calculated data have good agreement overall. The error between experiment and calculation for the smallest MHD cavity is probably due to the difficulty in etching high aspect ratio holes of this size with vertical sidewalls as well as a likelihood of increased sidewall roughness.

Hence, these measurements and simulations have verified that high quality factor can be maintained after the addition of small holes within the defect region of PhCs, which opens the door to improved molecular detection using the increased surface area available for analyte interaction.

3.4.3 Optimized Designs

After experimenting with different defect hole sizes and a fixed MHD defect hole spacing of 470 nm, MHD PhCs with a fixed defect hole size and variable defect hole spacings were fabricated. Following the discussion in Section 2.4.3, it is expected that the placement of the defect holes within the L3 cavity will have a large effect on both the resonance wavelength and the cavity Q. The fabricated MHD PhCs have the same defect hole spacings as the simulated cavities in Section 2.4.3, over the range of 180-500 nm in steps of 40 nm. Although defect hole spacings of 100 and 140 nm were simulated, they were not fabricated as the predicted Q is highly degraded for these designs, as shown in Fig. 2.15. The diameters of the defect holes in all the fabricated devices were measured to be 58.5 ± 3.5 nm using SEM metrology. The measured transmission spectra for the range of defect hole spacings are shown in Fig. 3.10, alongside the SEM images of their respective cavities.

Fig. 3.11 summarizes the experimental results, showing the resonance wavelength and

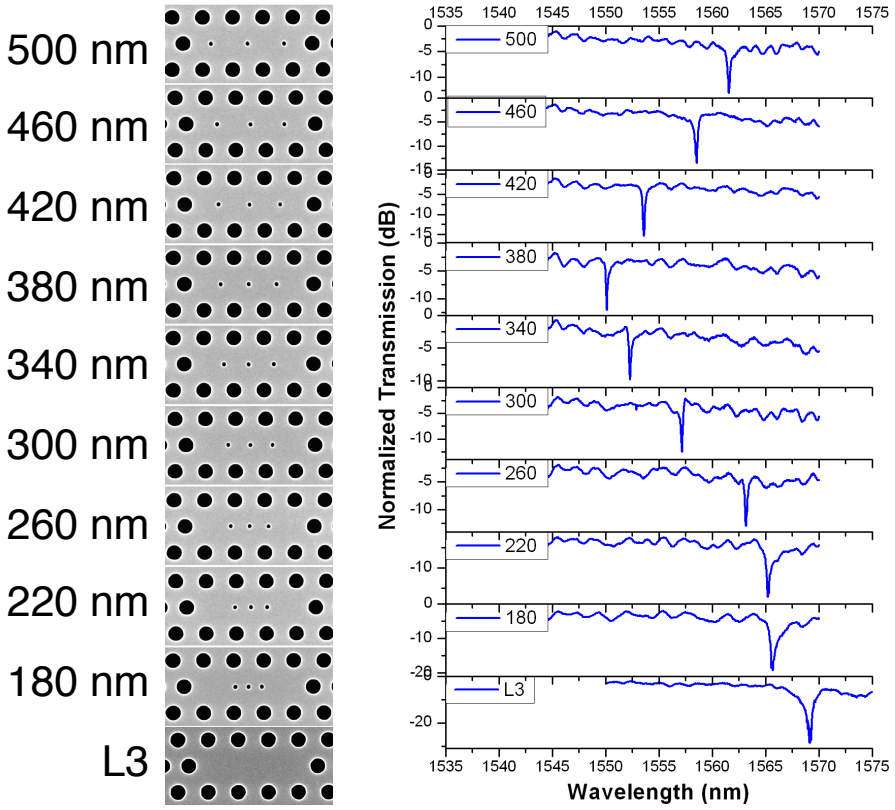

Figure 3.10: SEM images of fabricated defect hole lateral spacings (left), and their respective transmission spectra showing the trend of resonance shift (right).

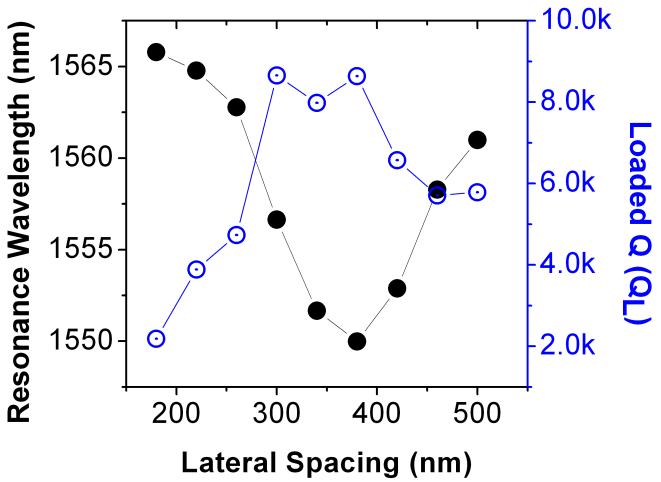

Figure 3.11: Resonance wavelengths (black, closed) and quality factors (blue, open) for fabricated MHD PhCs with varying lateral spacing.

Q_{load} for each of the measured cavities. From the simulated results in Section 2.4.3, recall that the intrinsic Q is maximized for a defect hole spacing of 380 nm. The experimental results show good agreement with the maximum measured value of Q_{load} = ∼9,000 occurring for a lateral spacing of about 300-380 nm lateral spacing. Note that slight deviation in the predicted trend of Q_{load} with different defect hole spacings may be due to slight imperfections and roughness that arise during the fabrication process. The largest resonance blue-shift compared to the L3 cavity with no defect holes ($\lambda = 1569$ nm) is nearly 20 nm and occurs at 380 nm spacing. The shift is about 2.5 times greater than the unoptimized design with 500 nm lateral spacing, and is a significant blue-shift. The measurement results confirm the simulated findings that for a lattice constant of 410 nm and lattice hole diameter of 210 nm, 380 nm is the ideal defect hole spacing for the MHD designs. This defect hole spacing corresponds to the maximized spatial overlap between the cavity mode intensity and the defect hole location. It is important to also note here that the quality factor trend in Fig. 3.11 shows the predicted result of enhanced Q for the ideal defect hole spacing. For reference, the Q_{load} of the L3 cavity is only ∼1,000. Therefore, the spatial and temporary overlap of the LMI is simultaneously enhanced for the ideal spacing. It is important to note that the ideal spacing of defect holes depends on the PhC lattice hole radius, due to the changing spatial confinement of the cavity mode. For a simulated PhC slab cavity with lattice hole radius of 137 nm, for example, the ideal spacing shifts to 340 nm instead of 380.

CHAPTER 4

BULK INDEX SENSING

Quantifying the improvement of light matter interaction in PhC MHD sensor devices involves perturbing the refractive index of the matter inside the defect holes, and measuring the resonance shift compared to a baseline L3 cavity with no defect holes. The simplest manner of refractive index perturbation is a *large-signal* "bulk" change, which is induced by infiltrating all low-index (air) regions in the slab PhC with another material, usually a fluid or gas which can be considered isotropic. The applications of bulk sensing are limited from a specific detection standpoint, because the refractive index does not necessarily have a one-to-one correlation with the composition of the analyte. Bulk index change is a common metric used to benchmark the sensitivity of sensor devices and is especially useful for evanescent-wave sensors such as the well-known surface plasmon resonance (SPR) based sensors [81]. SPR sensors are well-suited towards bulk sensing due to the long evanescent tail which extends into the cladding. In PhC slab point and line defects, the majority of the field is localized within the slab, which creates a disadvantage for bulk sensing. At resonance, field penetration into the low-index region is limited to the evanescent field leaking into the cladding above and below the slab, and in the leaky regions of the cavity mode in the surrounding lattice. When defect holes are incorporated, an increased volume is available for direct overlap with the cavity mode, which should increase the relative sensitivity compared to a device without MHD. It should be noted, however, that this additional increase in sensitivity is small given the small relative volume of the MHD compared to the surrounding volume in the lattice holes and the regions above and below the slab. In this section, the sensitivity figure of merit for bulk changes is considered, and sensitivity

results for MHD cavities are shown in simulation and experiment. The devices are exposed to several different analytes, each with different refractive index, in order to determine the sensitivity.

4.1 Sensitivity Figure of Merit

The sensitivity of sensor devices is often characterized as a change in the wavelength of a given spectral feature due to a perturbation in the refractive index:

$$\Delta\lambda = \lambda_{shift} - \lambda_0, \tag{4.1}$$

where λ_{shift} is the wavelength of the given spectral feature after refractive index perturbation, λ_0 is the initial wavelength of the spectral feature, and a redshift in Eqn. 4.1 suggests material addition. The wavelength shift is normalized to the change in bulk refractive index for the bulk index figure of merit S_{bulk}:

$$S_{bulk} = \frac{\Delta\lambda}{\Delta n} = \frac{\Delta\lambda}{n_{high} - n_{low}}. \tag{4.2}$$

Because refractive index is inherently unitless, S_{bulk} is given in terms of nanometers of resonance shift per refractive index units (nm/RIU). For all of the simulations and experiments in this chapter, it is assumed that $n_{low} = n_{air} = 1.0$. Experimentally, the cavities are measured before and after fluid infiltration in order to quantify the wavelength shift.

4.2 Methods

For all of the bulk sensing measurements performed in this work, direct drop-casting on to the sample is used. Using a digital pipette (FisherBrand Finnpippette), a consistent volume of liquid is measured out, and then deposited onto the PhC chip surface after initial fiber alignment of the optical measurement system with the PhC in place. A sufficient volume of liquid is used to fully cover the chip, approximately 100 µL per sample. Pre-alignment of the chip to the input/output fibers is necessary due to the scattered light from the surface of the chip due to the presence of the liquid, which makes alignment more difficult when monitoring with the overhead camera. Insertion loss of the device under test is also increased due to signal absorption and scattering. Care must be taken so that the on-chip fluids do not contact the fiber tapers, which can cause additional losses due to liquid bridging between the taper and the chip edge.

Material	Index
Air	1.0
Methanol	1.32
Water	1.33
Isopropyl Alcohol	1.377
Silicone Oil (DMS-T05)	1.97

Table 4.1: List of materials used for bulk index sensing.

The range of liquids used for bulk sensing is listed in Table 4.1. Each of the materials requires some special consideration to facilitate accurate measurements. For the organic solvents (methanol/IPA), the time length of the optical transmission measurement becomes a factor due to the quick evaporation from the surface. For OSA scans with resolution bandwidth 0.1 nm and sensitivity -90 dB, for example, a scan of several nanometers in width can take more than 100 seconds to complete. When sensing these materials, the surface fluid must be continuously replenished in order to create reliable results. Additionally, when

methanol and IPA are mixed to create intermediate refractive index fluids, it is possible that some error is introduced due to the different vapor pressures of each of the individual fluids in the mixture. That is, the refractive index of the initial fluid mixture may be different than the index after preferential evaporation of one of the fluids occurs. DI water can also be utilized when a relatively large index shift is desired. In this case, a lack of surface wetting due to the hydrophobic nature of the silicon slab may become a concern, which can prevent fluid penetration into the very small defect holes. Wetting can be promoted by partial oxidation of the PhC slab by thermal growth or vapor deposition of silicon dioxide, creating a more hydrophilic surface condition. A fluidic substitution method can also be used, where a small amount of solvent miscible with water (methanol or ethanol) is first deposited onto the device regions, and water is dropped onto the surface before solvent evaporation.

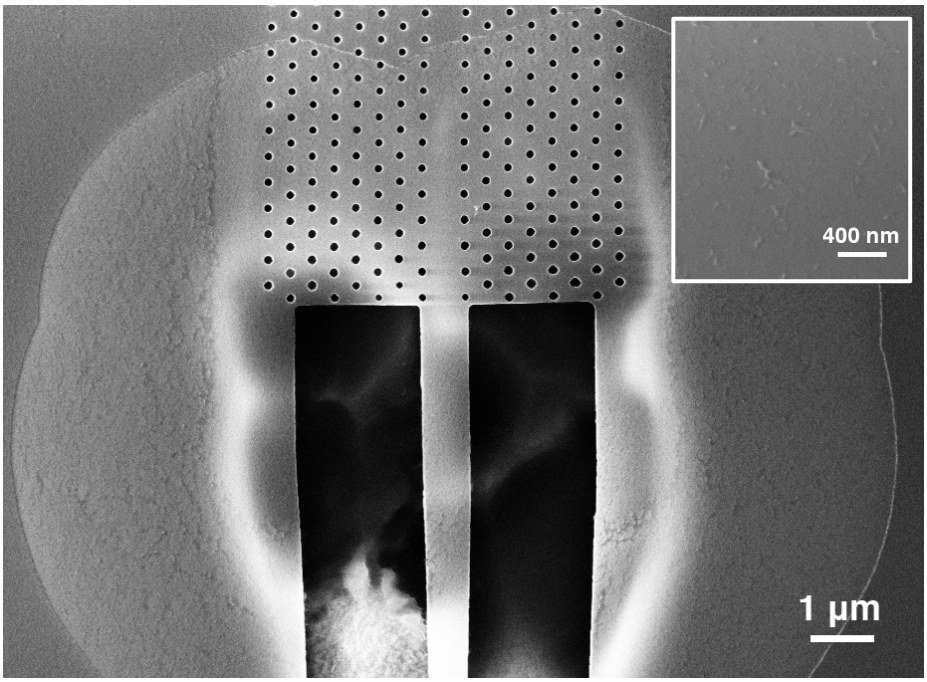

Figure 4.1: Residue at strip/W1 waveguide interface due to T05 silicone oil application and subsequent removal. Inset shows close-up of deposited polymer.

Finally, a commercially available silicone oil (Gelest Inc., DMS-T05) can be used for

reliable infiltration of the defect holes due to the easily wetting nature of the PDMS-based oil. Additionally, due to the slow rate of evaporation of the oil, long measurements can be performed accurately. Unfortunately, the use of silicone oil has the disadvantage of preventing device reusability by permanently modifying the slab surface, as shown in Fig. 4.1. Silicone oil usually leaves behind a polymer residue which is difficult to remove, even when the recommended treatment of hexane is used, which dissolves the PDMS polymer. All of these factors must be taken into consideration when performing a bulk index change experiment.

Designs consisting of single-hole defects and multiple-hole defects were tested on the same chip, along with L3 cavity baseline devices. The L3 cavity is used as the baseline for comparison due to the sensitivity to the index changes incurred primarily from analyte infiltrating the lattice holes. When the lattice holes are filled with analyte, the photonic bands shift due to reduced index contrast (i.e. silicon/air to silicon/analyte). An additional contribution occurs due to the field/analyte overlap at the evanescent field near the cavity. The large bandgap shift can also be seen by measuring the W1 cutoff wavelength shift after analyte infiltration. The total shift of the bulk index change for L3 PhCs can be attributed to both the shift of the band structure and the additional shift of the resonant state within the band gap. The additional volume contribution to the LMI due to MHD integration can be quantified by comparing the resonance shift after infiltration of fluid to the baseline L3 shift in fluid. By subtracting out the baseline L3 resonance shift from the devices with MHD, the remaining shift is the sole contribution of the defect holes, as the effect of the lattice has been normalized out.

4.3 Simulation

First, the effect of the fluid infiltration can be easily seen by modeling the bands of the PhC slab before/after fluid infiltration. `mpb` is used to model the band structure with a resolution of 16 grid points per a, which is the lattice constant normalized to 1. Fig. 4.2a shows the calculated band structure of the PhC slab with no defects, containing lattice holes with radius 105 nm and slab thickness 220 nm, in both air (blue) and silicone oil (red) backgrounds. The bands shift downward to lower frequencies in the silicone oil background, corresponding to a wavelength redshift in the dielectric band-edge. From the plot, it can be easily seen that the air-band (higher frequency) has a larger shift than that of the dielectric band, which is expected due to the large reduction of index contrast upon replacement of air with fluid. From an experimental standpoint, the W1 waveguide cutoff is more easily measured than the bandgap. The W1 bands were also simulated as shown in Fig. 4.2b, which shows the mid-gap guided modes for both air (left) and silicone oil (right) backgrounds. The x-axis is reversed on the silicone oil band plot, and the y-axis scale is equal on both plots, to more easily compare the shift in cutoff frequency. It should be noted that due to the addition of silicone oil in the cladding, the light line (light blue region) is lowered compared to that of air. Guided modes in the W1 waveguide must be below the light line, which has the dispersion equation $\omega = k_x c/n_{clad}$. Again, it is observed that the single-moded guiding region shifts to a lower frequency, which corresponds to a cutoff wavelength redshift of 43 nm after infiltration of silicone oil. Dividing this shift by the index change of 0.397 RIU results in a sensitivity of 108.3 nm/RIU for the W1 waveguide simulated by `mpb`.

For cavities, a bulk change must be simulated using the FDTD method due to the broken symmetry in the lattice. Simulation parameters are set by changing the default dielectric constant of the cell, as well as the dielectric constant of the individual lattice holes and

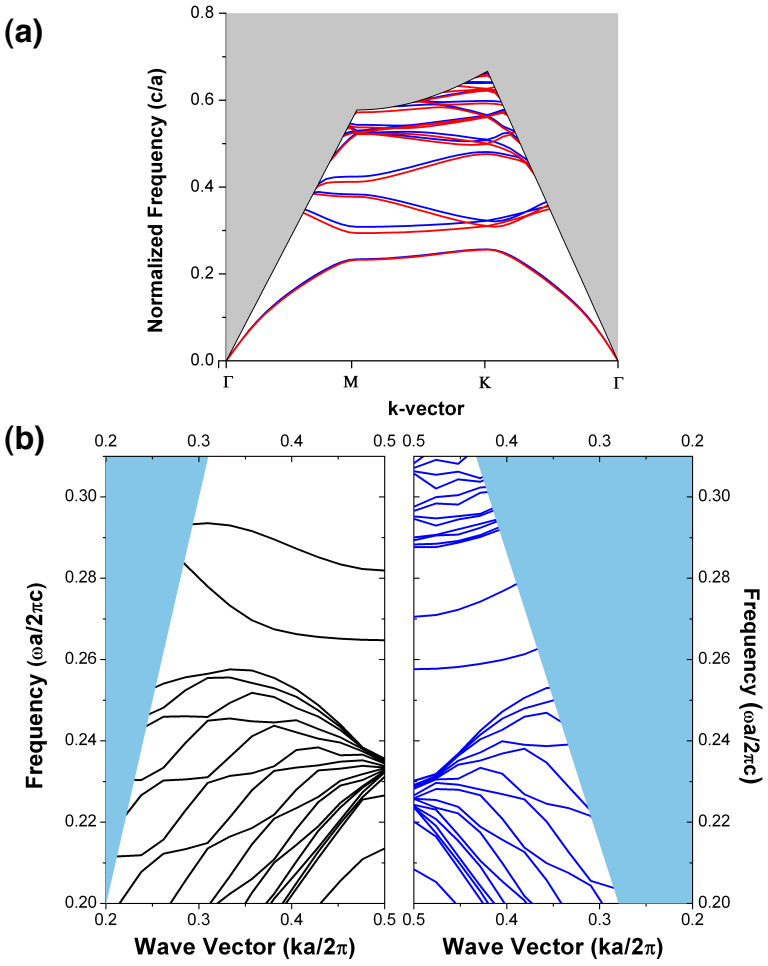

Figure 4.2: (a) Dispersion of a slab PhC with lattice hole radius 105 nm and slab thickness 220 nm in air (blue) and silicone oil (red) backgrounds, showing the downward frequency shift of the bands. (b) Comparison of PhC W1 waveguide dispersion in air (black, left) and silicone oil (blue, right) backgrounds, where the light blue regions indicate the light line. The waveguide cutoff occurs at a lower frequency for the device in oil background.

defect holes. In anticipation of experimental results, the sensitivity to any bulk change can be calculated by simulating a range of dielectric constants. The refractive index of the materials listed in Table 4.1, as well as intermediate index values below that of water, are used in the simulations.

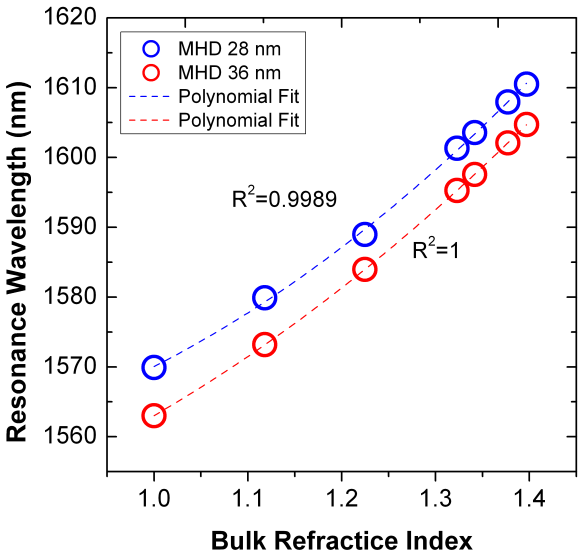

Figure 4.3: Simulated resonance wavelengths for 3-hole MHDs with 28 nm (blue) and 36 nm (red) radii and 470 nm lateral spacing in varying background refractive indices.

The resulting plots of the resonances of MHD PhCs are shown in Fig. 4.3, plotted as a function of simulated bulk refractive indices. The slope of the curve is the sensitivity in units of nm/RIU. The plot shows that the trend is not linear, but rather quadratic. Fitted polynomials for each of the two plots have R^2 values of nearly 1, showing a good agreement with a quadratic trend. From this result it should be noted that sensitivity values calculated from large bulk index changes may be underrating the device performance because the resonance trend is not linear. For example, at lower ranges of bulk index, such as the shift due to going from $n_{clad} = 1$ to $n_{clad} = 1.11$, the calculated sensitivity is 84.5 nm/RIU for the 28 nm MHD, and 86.2 nm/RIU for the 36 nm MHD. At a higher index range, the shift from IPA to silicone oil (1.377 to 1.397) results in sensitivities of 127 nm/RIU and 131 nm/RIU

for the 28 nm and 36 nm MHD cavities, respectively. Alternatively, when a larger shift of $n_{clad} = 1$ to $n_{clad} = 1.377$, is used to calculate sensitivity, this results in values of 101 and 104 nm/RIU, for 28 and 36 nm respectively. For reference, the L3 cavity with no defect holes gives a sensitivity of 94.6 nm/RIU for this shift. Therefore, previous studies such as that of Buswell et al. [40], which use an air to DI water cladding shift to quantify bulk sensitivity in a W1 waveguide, only characterize the initial large signal change. Finally, the larger holes in the MHD cavities show a larger sensitivity at both low and high values of bulk index, which is expected due to the larger volume available for analyte infiltration. It is important to note that the increase in the spatial LMI is shown by the increase in sensitivity upon adding defect holes to the cavity, even though the additional volume of the MHD is small relative to the overall volume of the PhC lattice holes. This is due to the defect holes being positioned in the region with the highest field localization, so that the degree of spatial overlap is increased inside the defect holes.

4.4 Solvent Mixtures

The limited availability of materials shown in Table 4.1 presents challenges for measuring small changes in bulk index on the same device. As shown in the previous simulation results, inducing small shifts in bulk index can potentially provide a more accurate picture of device sensitivity. Testing of more refractive index points can be achieved by using solvent mixtures, which results in a solution with an effective index in between the individual low and high index components. The bulk index change experiments were carried out using the fabricated 3-hole MHD cavity with 85 nm hole diameter by drop-casting various solvent solutions of IPA in methanol directly onto the chip before measuring. The 5 solutions of IPA in methanol had concentrations of 10/30/50/70/90% by weight, resulting in an approximately 0.0115 RIU change between each solution (after taking the weight percent

average of $n_{IPA} = 1.377$, $n_{Methanol} = 1.32$). The resonant modes in the transmission spectra after drop-casting each solution are shown in Fig. 4.4. The sensitivity of the fabricated MHD devices was found to be approximately 65 nm/RIU by linear regression, compared to the simulated sensitivity of 115 nm/RIU. Linear regression is used instead of a quadratic fit in this case, due to the relatively small changes in refractive index being considered. The difference between measured and simulated sensitivity can be explained by possible errors introduced by the fast evaporation of the solvent mixture, which requires constant replenishing of the surface fluid, and the difference in evaporation rates in the two solvents. Compared to an L3 cavity without any defect holes, the simulated sensitivity of the MHD device to the IPA/methanol mixtures represents a 10% increase.

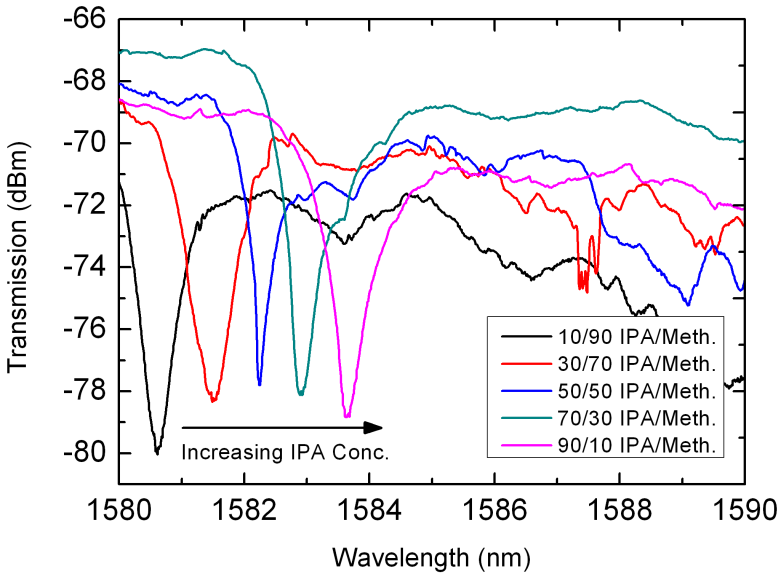

Figure 4.4: Resonance shift for a 3-hole MHD L3 cavity with as-designed defect hole diameter of 85 nm, in mixtures of IPA/methanol solvent solutions.

4.5 Index-Matching Oil

In order to overcome the difficulty of measuring fast-evaporating solvents, another set of MHD PhC devices was exposed to a silicone oil of known refractive index, which does not

evaporate over a long period of time. A pipette was again used to wet the entire surface of the chips and the refractive index of the medium surrounding the PhC slab was therefore increased by 0.397. Transmission data were acquired before and after silicone oil treatment, in both cases normalizing to the transmission spectra of strip waveguides. The L3 device is again used as a baseline for comparison in this experiment to help distinguish the relative contributions of the lattice holes and defect holes of the MHD in the overall wavelength shift measured in transmission.

From the data shown in Table 4.2, it is found that the baseline resonance redshift of two different L3 cavities is 32.75±0.15 nm. With the addition of SHDs and MHDs, the increased volume contribution provides up to an additional 18% increase in the resonance shift for the 80 nm MHD, compared to an 11% increase for the 84 nm SHD. The detection sensitivity of these MHD and SHD cavities is calculated to be 98±2 nm/RIU and 91±2 nm/RIU, respectively, compared to the L3 cavities that have detection sensitivity of 82 nm/RIU. These sensitivities are comparable to previously published work on bulk index sensing of L3 and single point defect PhC cavities [48]. Again, as the accessible volume for sensing is increased, especially in regions of high field concentration, the detection sensitivity of the PhCs improves. Hence, for volume sensing, a single large hole could potentially hold the same or improved bulk index detection sensitivity compared to multiple holes of smaller size.

	Single Hole Defect (SHD)				Multiple Hole Defect (MHD)		
Diameter	Air	Oil	Shift	Diameter	Air	Oil	Shift
(L3)	1549.8	1582.4	**32.6**	(L3)	1551.3	1584.2	**32.9**
69	1540.3	1574.6	**34.3**	61.2	1539.5	1574.7	**35.2**
73	1537.7	1573.0	**35.3**	73.6	1532.0	1568.9	**36.9**
84	1535.2	1571.5	**36.3**	80	1523.8	1562.82	**39.0**

Table 4.2: Resonance data for SHD and MHD cavities before and after wetting with silicone oil. (All units in nm)

4.6 Performance Comparison

The previous sections in this chapter presented both simulated and experimental results characterizing the performance of MHD, SHD, L3, and W1 PhCs for bulk index sensing using various fluids. For some solutions, residue left on the chip surfaces requires the use of several different chips for each bulk sensing experiment, which introduces sources of error due to the solution evaporation and chip-to-chip variation in device quality. However, the best measured sensitivities can be compared to previously reported PhC sensors fabricated by other groups to gain understanding into the sensor performance of the MHD compared to other designs. As a reference, the sensitivities to large bulk refractive index shifts (from air to IPA and air to silicone oil) are shown in Fig. 4.5a below for all types of devices (L3, SHD, MHD) investigated in this thesis. The data were gathered from two chips with identical patterned features, and the defect hole sizes were confirmed to be similar on both chips using SEM. As mentioned previously, the sensitivity calculated using the large-index shift from air to solution is usually lower than the small-index shift sensitivity due to the quadratic nature of the resonance change. Fig. 4.5b plots the sensitivity for each device using the intermediate resonance shift from IPA to silicone oil ($\Delta n = 0.02$). The effect of device variation can be seen in the two L3 cavities shown in Fig 4.5a, where the L3 in the SHD group underperforms in the silicone oil experiment, resulting in a low small-index change sensitivity of 77.3 nm/RIU in Fig 4.5b. Also, the 50 nm MHD design has a lower measured small-index change sensitivity than that of the 30 nm design, which is likely due to fabrication imperfections and possible error in volume filling. Other than these devices, the general expected trend is seen, where larger hole diameter designs have higher sensitivity, and MHD devices have higher sensitivity than the similarly sized SHD devices.

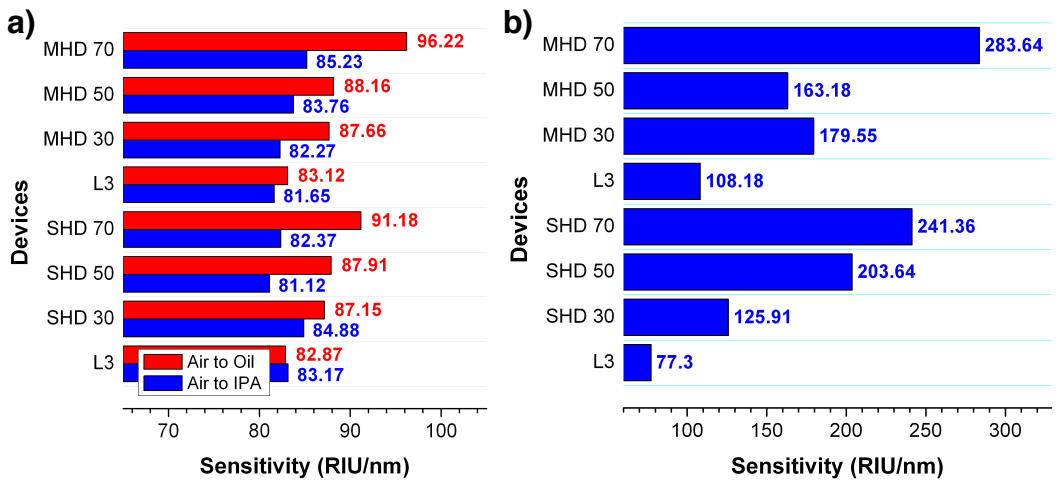

Figure 4.5: Bar graphs of (a) large index change sensitivity from air to silicone oil (red) and IPA (blue), and (b) small index change sensitivity from IPA to silicone oil, for L3, SHD, and MHD cavities.

Table 4.3 contains bulk index sensitivity data of several different PhC sensors, with the sensitivity values for MHD PhC devices included for comparison. While nm/RIU sensitivity is often taken to be the raw sensitivity merit, the quality factor of the cavity must also be considered when calculating the detection limit, or the minimum resolvable index change. For this reason, a trade-off must be considered for the desired application when choosing an appropriate sensor platform. Although H1 type cavities have a larger resonance position sensitivity, the quality factors are generally lower for the shown references. Lower quality factors indicate leaky cavity modes, which can be an advantage for bulk sensing, where a larger overlap of the field with analyte is desired per unit volume. The opposite is true for high quality factor L3-type cavities, which have lower bulk sensitivity compared to the H1 cavities. Nevertheless, improvement in sensitivity is demonstrated for the SHD and MHD devices over solid L3 cavities with no defect holes, due to the increase in field overlap with analyte. While performance is generally improved over regular L3 cavities, PhC MHD cavities are generally not optimized for volume sensing, unless large defect hole diameters are implemented. Thus, MHD PhCs with small defect holes are better suited to surface sensing

applications, where a high quality factor is maintained while simultaneously increasing the spatial overlap of the field and surface-bound analyte. The next chapter will discuss experimental surface sensing results, which demonstrate the increased sensitivity of MHD PhCs to surface perturbations compared to a bulk change.

Device Type	Notes	Sensitivity	Cavity Q	Reference
H1 Cavity	Undercut SHD, donor type	155±6 nm/RIU	400	[48]
H1 Cavity	No undercut SHD, acceptor type	<200 nm/RIU	400	[44]
H1 Laser	III-V QW SHD laser	266 nm/RIU	1000	[45]
H0 Laser	III-V QW laser	350 nm/RIU	>4000	[46]
W1 Waveguide	Cutoff shift, not undercut	88 nm/RIU	-	[40]
L3 Cavity	Undercut etched	63±9 nm/RIU	3000	[48]
L3 SHD	(This work, large index change)	91 nm/RIU	6000	-
L3 MHD	(This work, large index change)	98 nm/RIU	6000	-

Table 4.3: Comparison of bulk index sensitivities for PhC slab-based sensors.

4.7 Summary

In this chapter, the LMI enhancement of MHD PhCs was analyzed by simulation and experiment of bulk refractive index changes. The lattice and defect holes of MHD PhCs were infiltrated with fluids having various refractive indices, by wetting the surfaces using drop-casting. The reduction in the index-contrast between the slab and cladding results in a photonic bandgap shift to lower frequencies, correspondingly red-shifting spectral features to higher wavelengths. MHD PhCs simulated with FDTD were found to have a quadratic dependency for resonance shift versus bulk refractive index, resulting in higher sensitivities at larger refractive indices. Because of the quadratic trend, the simulated sensitivity of the MHD to a bulk change was found to vary from 84.5 nm/RIU to 131 nm/RIU depending on the refractive index change. MHD PhCs were then subjected to solutions of methanol/IPA and silicone oil, in order to explore small and large index changes, respectively. The methanol/IPA mixtures indicated an average sensitivity of 66 nm/RIU for an 85 nm diameter MHD PhC, representing a 10% increase over the sensitivity of the L3 cavity

with no defect holes. The reduction in sensitivity compared to simulation is potentially due to the differing rates of evaporation in the methanol/IPA mixture, resulting in measurement errors. When PhCs were infiltrated with slowly evaporating silicone oil with refractive index $n = 1.397$, the sensitivity of SHD and MHD cavities was found to be 91 ± 2 nm/RIU and 98 ± 2 nm/RIU, respectively. The MHD PhC was found to have an 18% increase in resonance shift compared an L3 cavity infiltrated with silicone oil. Both the SHD and MHD PhCs have increased sensitivity compared to previously published L3 PhC cavity devices with 63 ± 9 nm/RIU sensitivity. The results indicate increased spatial light matter interaction, due to the defect holes contributing direct modal field overlap with the analyte contained within the holes.

CHAPTER 5

SURFACE INDEX CHANGE

Several drawbacks are associated with the bulk index change methods described in the previous chapter for exploring the light-matter interaction enhancement in MHD PhCs. First, the index contrast reduction at the slab surface due to the introduction of a liquid cladding results in increased field leakage into the cladding, which lowers the effective index of the mode and results in lower values of cavity Q. Lower Q not only reduces temporal LMI, but is undesirable from the standpoint of lower detection limits for sensor applications, because a sharper resonance can resolve smaller changes in the cavity mode. Increased scattering and absorption at the fluid/slab interfaces also generally reduces device performance by increasing losses, which affects the Q as well as the signal-to-noise ratio measured at the detector. Second, the most intense field is contained within the slab at the cavity, and although the results in the previous chapter demonstrate increased sensitivity due to integration of Multiple-Hole Defects, ideally larger defect holes are necessary to increase the volume of fluid that can directly interact with the cavity mode. Unfortunately, increasing the size of the defect holes results in more scattering in the cavity and thus lower Q, as shown in Chapter 2. It is important to again emphasize that the advantage of the PhC cavity over other photonic structures is the high Q/V_{mode} ratio; hence PhC cavities are not best-suited to applications which utilize evanescent waves and radiative modes.

Surface-based sensing methods, on the other hand, cause less scattering losses due to the relatively small dimensions of the perturbations, with respect to the wavelength of interest. As a result, high Q is maintained and less field leaks from the cavity, enhancing the intensity of light inside the cavity for LMI. Also, unlike the bulk sensing measure-

ments, the amount of analyte involved in the LMI is a small amount affixed to the surface. For a monolayer coating on the slab surface, the quantity of analyte interacting with the mode is a function of the percent coverage, as well as the size/thickness of the monolayer. Therefore, surface sensing measurements can contribute information about the degree of surface attachment efficiency, and also determine the relative thickness between two different monolayers attached in succession. In this chapter, the degree of LMI improvement in MHD PhC cavities compared to L3 cavities is quantified by measuring the sensitivity to monolayers applied to the slab surface with several different thicknesses. The resonance of MHD PhCs is first measured after 5-6 nm-thick silicon dioxide deposition. Afterwards, two molecules of $\sim$1 nm thickness, which functionalize the surface for thiol-terminated biomolecules, are used to simultaneously prepare the surface for label-free sensing applications and demonstrate sensitivity to small surface perturbations. The combined thickness of the added films is small enough that the length scale of the evanescently decaying tail does not play a large role, and that the total size of the added material is much smaller than the fabricated range of defect hole sizes (40-60 nm).

5.1 Sample Preparation

For surface monolayer attachment, additional sample preparation is necessary beyond the fabrication steps mentioned in Chapter 3. After the PhC regions are exposed to BOE to remove the underlying oxide, the polymer couplers are cleaved through and the protective photoresist is removed. At this point, the surface condition must be optimized for the binding characteristics of the specific small molecules that will be exposed to the PhC slab surface. Two molecules in particular are needed to ultimately form linkers to a thiol-terminated probe molecule on the surface, and they are shown in Fig. 5.1a-b below. The first step involves forming a monolayer of 3-aminopropyltriethoxysilane (3-APTES) on

the surface, which is 0.8 nm thick [82]. Following the functionalization steps outlined in Rong and Weiss [57], an oxidized surface is necessary for 3-APTES binding. Due to the presence of the heat-sensitive polymer couplers, even low-temperature thermal oxidation at 500-800 °C is undesirable as an oxide growth method, as cross-linked SU-8 films have a glass transition temperature of $T_g = 200\,^{\circ}\mathrm{C}$ and a degradation temperature of $T_d = 380\,^{\circ}\mathrm{C}$ [83]. Ideally, the individual chips would be oxidized in-between the BOE and polymer coupler lithography steps. However, this was not possible as the SU-8 on the as-received chips was applied on a wafer-level. Therefore, for the first experiments, native oxide on the silicon surface was utilized instead of growing a more typical thermal oxide. Samples were stored at room temperature for about one week after BOE was performed, allowing an oxide layer approximately 8 Å thick to be formed on the PhC surfaces [84].

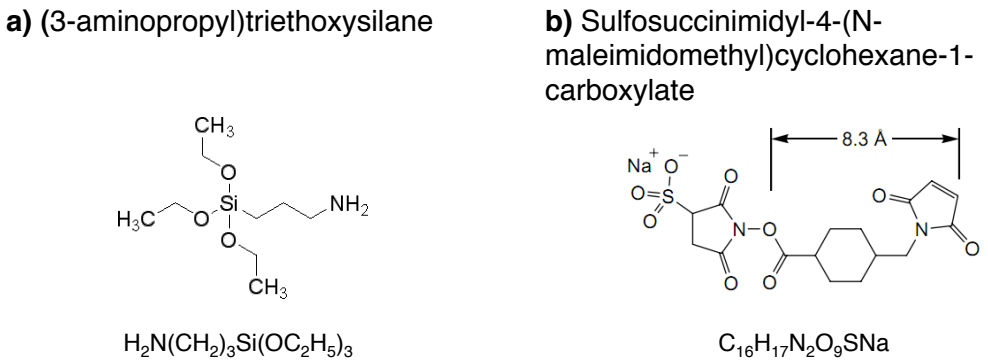

Figure 5.1: Structure and chemical formula of molecules used in functionalization: a) 3-APTES, and b) sulfo-SMCC.

For more uniform oxide coverage, a room temperature atomic layer deposition (ALD) method developed by Hatton et al. [85] was utilized. In traditional ALD tools, deposition occurs on a cycled basis, where the sample is held in a vacuum chamber and precursor gases are pumped into the chamber in succession, with nitrogen purges in between. The process is self-limiting due to the nature of the surface reactions, so the film thickness is controlled by the number of cycle repetitions. ALD is an ideal method of oxide deposition

in the case of MHD devices for two reasons in particular. First, the ability to control deposition thickness on an atomic level enables the characterization of the device's sensitivity to extremely small surface perturbations. Second, the conformality of ALD deposited films ensures that the inner surface of the defect holes as well as the underside of the PhC slab are coated with oxide. The tuning of PhC cavity resonances has been demonstrated by conformal deposition of oxides such as HfO_2 using atomic-layer deposition (ALD) [86]. Unfortunately, the tools and precursors for depositing ALD films is often costly, and need to be kept in a cleanroom environment. As an alternative, the ALD process from [85] is a room-temperature process that can be carried out in a fume-hood commonly found in laboratories, as shown in Fig. 5.2. Each "cycle," for what will be referred to here as the test tube ALD method, consists of exposing the sample to tetramethoxysilane (TMOS, $Si(OCH_3)_4$), and then ammonium hydroxide ($NH_3{\cdot}H_2O$) vapors, for 10 minutes each. 5 mL of each solution is placed into two test tubes, and the photonic chip is suspended approximately 2 cm over the surface of the liquid by a wound copper wire during deposition. The distance to the surface of the solutions dictates the deposition rate, so the length of the wire should be kept consistent. Additionally, care must be taken when inserting the sample into the test tube so that the edges of the chip, where optical coupling occurs, are not harmed. Inside the test tube, the NH_3 vapor catalyzes the hydrolysis of the methoxysilane groups, which react with surface-bound hydroxyl groups [85]. A cycle deposits approximately 2 nm of silicon dioxide, as measured by ellipsometry.

After test tube ALD oxide deposition, the sample is silanized using a 4% solution of 3-APTES, consisting of 40 μL 99% 3-APTES (Sigma-Aldrich), 500 μL DI water and 460 μL methanol, for 20 minutes. 3-APTES molecules are physiosorbed onto the silicon surface as the ethoxy groups are hydrogen bonded to the oxidized surface. A free oxygen molecule on the surface then creates a chemical bond with the Si atom, releasing a molecule of ethanol.

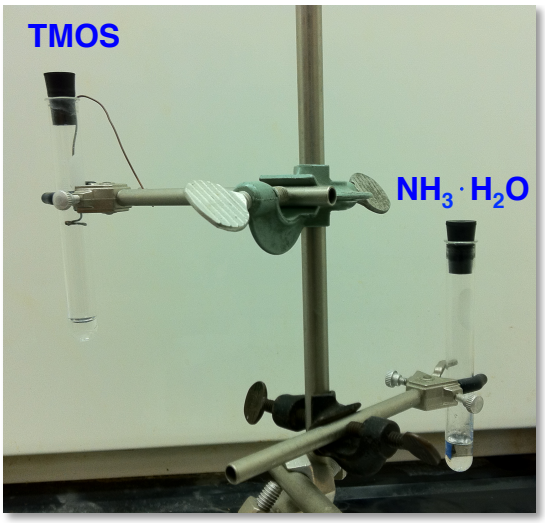

Figure 5.2: Photo of in-hood ALD set-up, with test tubes filled with TMOS and NH_3H_2O.

During the 20 minute 3-APTES soak, a humid environment is used (covered petri dish with DI water) in order to prevent evaporation of the 3-APTES solution from the sample surface. The sample is then rinsed with DI water, dried with nitrogen, and baked at 100 °C for 10 minutes to crosslink the silane monolayer and evaporate any remaining solvent. The 3-APTES monolayer provides an amine group for the linker molecule sulfo-SMCC (sulfosuccinimidyl 4-[N-maleimidomethyl]cyclohexane-1-carboxylate) to bind to, which is the intermediate step before thiol-terminated probe molecule attachment. The silanized sample is then exposed to a 2.5 mg/mL solution of sulfo-SMCC (Pierce) in HEPES buffer (20 mM HEPES, 150 mM NaCl, 5 mM EDTA, pH 7.4) for 2 hours, and then soaked in HEPES buffer for 1 hour before rinsing with DI water and drying with nitrogen. The sulfo-SMCC films form a 1.2 nm-thick monolayer on top of the 3-APTES film. The thicknesses for both films are measured by ellipsometry after attachment on a bare silicon wafer. The maleimide groups on the functionalized surface are then available for binding to thiol-terminated biomolecules such as DNA or benzenethiol.

5.2 3-APTES Detection with Native Oxide

First, the effectiveness of the native oxide for molecule attachment is explored. Although surface area available for binding is increased by MHD, the binding efficiency of each molecule attachment step is usually less than 100%, which reduces the number of available sites as more molecules are added. Thus, the surface oxide condition, and the initial 3-APTES coverage efficiency is important for maintaining high sensitivity for future analyte capture. The transmission spectra of samples with native oxide were measured before and after 3-APTES attachment, and the resonance shifts were evaluated to determine surface-based detection sensitivity, as shown in Fig. 5.3. The samples used in this experiment were unoptimized, with a lateral defect hole spacing of 470 nm. In the figure, the resonances in air are centered on the x-axis, which has the same scale for all three devices, in order to simplify comparison. The measured spectra were fit with Lorentzian curves to extract the resonance wavelength and the Q_{load}. The resonances for the solid L3 cavity, which once again reveal the baseline contribution of the PhC lattice, and two sizes of MHD are included for comparison. The maximum surface-based sensitivity improvement compared to the L3 is 44% for the 67 nm diameter MHD. The MHD cavity with the smaller defect hole diameter (56 nm) gives a 27% sensitivity increase. Both MHD cavities have a Q_{load} value of $\sim$6000. It is important to note that Q_{load} is not severely degraded after 3-APTES attachment, even though the surface condition is perturbed. The presence of the molecule within the defect holes is enough to change the resonance position, but not cause excessive scattering losses.

From the results shown in Fig. 5.3, it is clear that the additional surface area provided by the MHD enables improved surface-based sensing sensitivity without degrading the cavity Q_{load}. The relative sensitivity improvement gained by adding MHD to an L3 cavity is

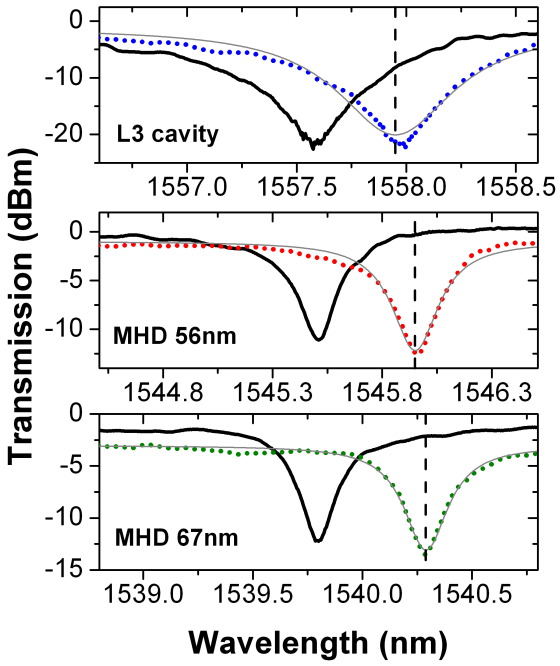

Figure 5.3: Transmission spectra for resonances of L3 cavity, 56 nm diameter MHD cavity and 67 nm diameter MHD cavity before (solid curve) and after (blue, red, and green, respectively) application of $\sim$1 nm monolayer of 3-APTES.

greater for surface-based sensing than for bulk index sensing (27% for 3-APTES compared to 18% in bulk sensing). This result is expected because the additional internal surface area provided by the MHD represents a larger fractional increase in the overall available surface area for molecular binding in the PhC compared to the small increase in volume provided by the MHD for bulk index sensing. It is important to note that due to the imperfect coverage of the native oxide, it is likely that the 3-APTES binding in the cavities does not form a uniform monolayer. Any non-uniformity in coverage would also contribute some sample-to-sample variation in sensitivity. Also, the unoptimized lateral positioning of the defect holes has the effect of limiting the total sensitivity of the device, due to reduced overlap with the highest intensity field, as discussed in Chapter 3. The largest sensitivity can thus be extracted using the optimal hole positioning in order to increase the cavity mode perturbation, and by creating a more uniform oxide to increase the number of small-molecule binding

sites per unit area. Here it should be noted that no simulations are provided for matching to experimental monolayer attachment due to the relatively small size of the monolayer thickness relative to the defect hole size. In order to resolve features on the order of several nanometers thick, the required grid in the FDTD simulation, for example, would be extremely memory and simulation time intensive. Simulation tools based on perturbation theory are currently being researched in order to achieve these results through techniques other than FDTD.

5.3 Sulfo-SMCC Detection with ALD Oxide

To overcome the reduced coverage of the native oxide on the MHD PhC surfaces, and subsequently, increase the available sites for molecular binding, the test tube ALD method is utilized. ALD oxide films of thickness 5-6 nm were applied to new chips immediately after undercutting the slabs with the HF-based BOE. The ALD oxide deposition causes a redshift in the resonance wavelength since material is added to the PhC lattice and defect region. Because the sulfo-SMCC layer binds on top of the pre-existing 3-APTES monolayer, the magnitude of the shift in each step is anticipated to be related to the relative thicknesses of each molecule. Therefore, under the assumption that oxide, 3-APTES, and sulfo-SMCC have a similar refractive index, the largest redshift should occur after ALD oxide growth (6 nm thickness), the 3-APTES (0.8 nm) should give the smallest shift, and the sulfo-SMCC (1.2 nm) shift should be larger than that of the 3-APTES.

Fig. 5.4 presents the resonance shift data for all defect hole lateral spacings of the 3-hole MHD PhC cavities (as previously shown in Section 3.4.3), for each step of functionalization. Two sizes of defect holes are shown: 55 nm (Fig. 5.4a) and 60 nm (Fig. 5.4b) diameter. The cumulative resonance shift resulting from the addition of each monolayer is shown by the black (ALD), red (3-APTES) and blue (sulfo-SMCC) bars for each MHD PhC. An L3

cavity measurement is also shown along side the 55 nm devices for comparison. The magnitude of the resonance shift for each molecule attachment in the 60 nm MHD PhC is more than the respective shift in the 55 nm MHD PhC device, which confirms that the detection sensitivity is improved for larger available surface areas. The trend shown in the design optimization passive measurements in Section 3.4.3 is maintained, as the largest cumulative shift occurs when the defect holes are located near the optimal lateral spacing. This further confirms that the spacing of 380 nm is ideal for the MHD PhC design consisting of 3 defect holes within an L3 cavity when the lattice hole radius is 100 nm. Also, as expected, the resonance shift which occurs after ALD deposition is the largest relative shift, and the binding of 3-APTES and sulfo-SMCC cause relative shifts which are much smaller due to their respective molecular sizes. It should be noted that the expected shift is not exactly proportional to the molecule size since the available surface area shrinks with each molecule attachment, due to the reduced radius of the defect hole and a surface coverage which is less than 100%.

As a comparison to the unoptimized device (lateral defect hole spacing of 500 nm) used to measure the resonances after native oxide growth and 3-APTES attachment in the previous section, Fig. 5.5 shows the normalized transmission of the two MHD cavities with 55 nm and 60 nm diameter defect holes and 500 nm lateral hole spacing after test tube ALD oxide growth and 3-APTES attachment. The resonance is plotted after each step of surface attachment, with the starting passive measurement (i.e., air-filled defect holes) shown in the black curves. Recall that the sensitivity improvement in the MHD device with native oxide and unoptimized spacing was measured to be 44% with respect to the L3 baseline cavity (also with native oxide), as a cumulative percentage increase in magnitude of resonance wavelength shift after 3-APTES binding. In the devices with ALD oxide deposited on the surface, it is found that for the unoptimized spacing, the percentage increase in the

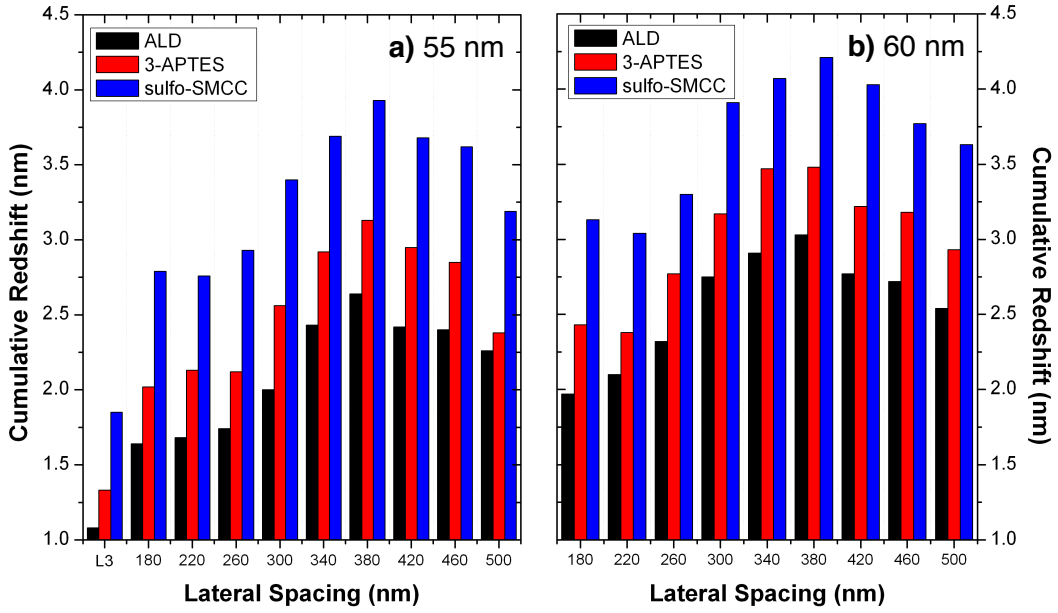

Figure 5.4: Bar graphs showing the cumulative resonance redshift for two groups of MHD devices with 55 nm (left) and 60 nm diameters (right). The redshifts due to ALD deposition (black), 3-APTES binding (red) and sulfo-SMCC binding (blue) are shown for each lateral defect hole spacing, and a L3 cavity is shown for reference.

cumulative resonance shift was 80% for the 55 nm diameter MHD, and 120% for the 60 nm diameter MHD, both with respect to the L3 cavity with the same oxide coverage. The addition of the conformal ALD oxide clearly improves the sensing capability of the device by allowing more analyte to bind to the surface of the chip. This test tube ALD method can potentially be applied to other photonic devices as well, where thermal oxidation of silicon cannot be integrated into the fabrication process due to temperature limitations. An expanded discussion of such future applications is discussed in Chapter 6.

Now using the optimized design with 380 nm lateral spacing, resonances after oxide growth, 3-APTES binding, and sulfo-SMCC binding steps are shown in Fig. 5.6 for the defect holes with 60 nm diameter. The corresponding data are shown in Table 5.1, which shows the percent increase in the cumulative resonance shift compared to the baseline L3 cavity for each functionalization step. Again, the sharpness of the resonances is maintained

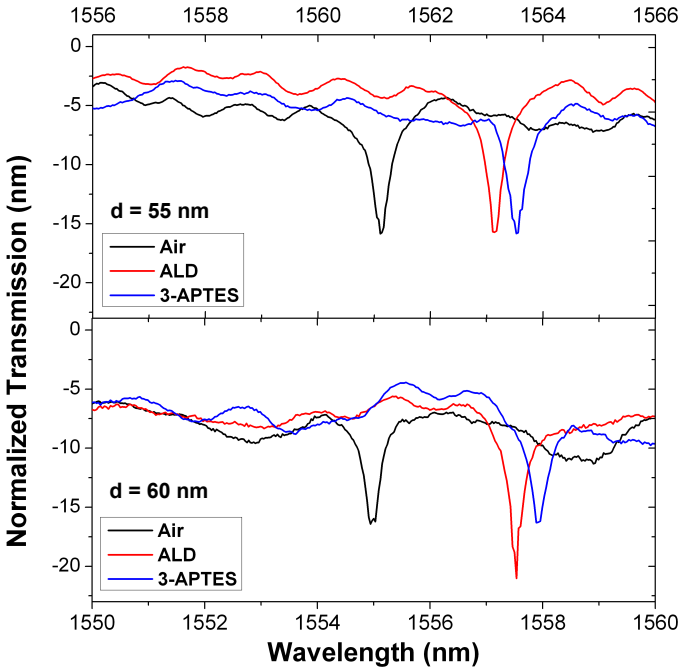

Figure 5.5: Resonances of MHD cavities with 380 nm defect hole spacing before (black) and after (red) 6 nm of in-hood ALD growth. Defect hole diameters of 55 nm (top) and 60 nm (bottom) are shown for comparison, showing sensitivity increase for higher surface areas.

throughout molecule attachment, so the quality factor is not affected adversely. The fully optimized cavity has a 160% increase in cumulative shift with respect to the L3 cavity for the 3-APTES attachment. This is more than twice the percent increase previously measured in the cavity with unoptimized lateral defect hole spacing of 500 nm with ALD oxide, and more than 4 times the sensitivity increase of the cavity with unoptimized spacing using the native oxide for molecule attachment. Although a larger defect hole diameter contributes more surface area, and thus more sensitivity, the advantage of increased binding to the ALD oxide surface results in increased sensitivity even when the defect hole diameter is smaller (60 nm for ALD oxide, 67 nm for native oxide). Thus the surface condition is vital to the ultimate sensitivity of the cavity. It is anticipated that choosing a higher quality thermal oxide growth step in between the BOE and SU-8 polymer steps will increase the sensitivity even further due to better surface coverage and film quality.

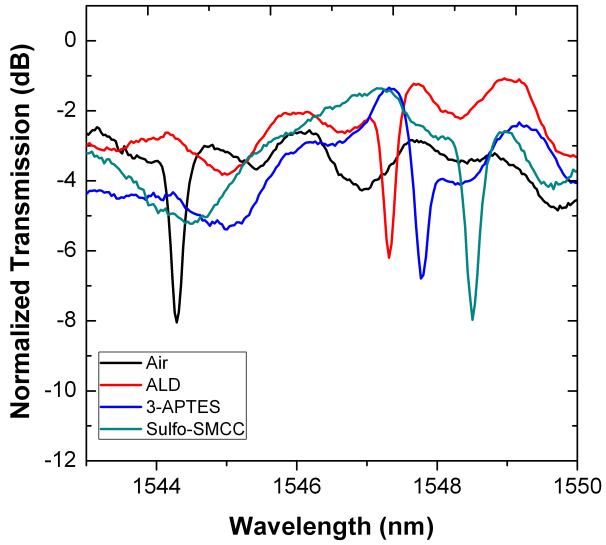

Figure 5.6: Transmission spectra for resonances of optimized MHD cavity with 60 nm defect hole diameter and a lateral spacing of 380 nm: before (black) and after (red) ALD oxide growth, 3-APTES silanization (blue) and sulfo-SMCC attachment (green).

When considering a sensitivity comparison to other published label-free sensor platforms, choosing a proper figure of merit becomes difficult, since the sensitivity of most

Material	L3 (Baseline)	60 nm MHD	Percent Increase
ALD Oxide	1.08 nm	3.03 nm	180%
3-APTES	1.33 nm	3.48 nm	162%
sulfo-SMCC	1.85 nm	4.31 nm	133%

Table 5.1: Cumulative shift of resonance wavelength for L3 cavity baseline and 60 nm MHD cavity and the percent increase in resonance shift for the MHD cavity compared to the L3 cavity at each step.

optical sensor devices are shown in terms of a bulk refractive index change or the concentration of molecules in a solution exposed to the sensor [87]. Such a comparison would be possible after specific attachment of molecules of varying concentrations. However, it is possible to examine the relationship between the resonance shift due to molecule attachment of a particular species and the estimated quantity of this molecular species bound to the defect hole walls, in order to find the minimum detectable mass of the MHD PhC sensor. The mass of the bound molecules, in this case 3-APTES, can be found by taking the product of the 3-APTES density (0.946 g/mL) and the total volume of the monolayer of 3-APTES in the region of interest. Here, the regions of interest are limited to the circular areas where defect holes are introduced. Because all aspects of the L3 cavities and MHD cavities are similar except for the addition of defect holes, the effect of the surrounding photonic crystal slab is essentially normalized out when considering the L3 as the baseline case. Therefore only the additional area/volume afforded by the defect holes need be considered for this analysis.

Here, the additional surface area due to the addition of the defect hole is considered. At each position where a defect hole is added to the PhC cavity, the surface area available for binding consists of the sidewalls of the cylindrically shaped defect holes. Therefore, the original binding area at these positions, which consists of two circular areas on the upper and lower sides of the slab, is substituted for the increased area of the cylindrical defect hole. As a result, the surface area increases from $2\pi r_{def}^2$ to $2\pi r_{def} t_{slab}$, where t_{slab} is the

thickness of the silicon slab. Taking the thickness of the monolayer of molecules t_m into account, the volume of bound molecules in both of these areas is:

$$\begin{aligned} V_{L3} &= 2\pi r_{def}^2 \cdot t_m \\ V_{MHD} &= \pi(r_{def}^2 - (r_{def} - t_m)^2) \cdot t_{slab}. \end{aligned} \tag{5.1}$$

Assuming a 60 nm defect hole diameter ($r_{def} = 30$ nm), 220 nm slab, and a 0.8 nm monolayer thickness, the density is multiplied with the volume to calculate the mass. Using Eqn. 5.1, the mass contained in the circular areas in the L3 cavity without defect holes was calculated to be $m_{L3} = 4.5(10^{-18})$ g, and the monolayer bound to the defect hole sidewalls was calculated to have a mass of $m_{MHD} = 3.3(10^{-17})$ g $= 0.03$ fg. This reflects an enhancement factor of $\sim$7 times in the surface-bound mass with respect to the L3 cavity, which corresponds to the previously mentioned increase in surface area due to defect hole aspect ratio of t_{slab}/r_{def} (220 nm / 30 nm = 7.33). Recall from Table 5.1 that the 3-APTES causes a shift of 0.45 nm for the 0.03 fg of deposited material, under the assumption of complete monolayer attachment. If the minimum resolvable wavelength shift is assumed to be 0.25 nm ($\lambda_0/Q = 1547/6000$), it is potentially possible to detect a particle with a mass of $0.03/(0.45/0.25) = 0.016$ fg. For comparison, the mass of a single HIV-1 particle is $\sim$80 attograms [88]. The detection limit in the optimized MHD cavity is smaller than the limit found by Lee and Fauchet [50] of 0.05 fg, which is for a PhC with a single-hole defect (H1-type cavity) of diameter 140 nm, without undercut etch.

5.4 Summary

The enhancement of light-matter interaction in MHD PhCs was explored by adding surface perturbations to the inside of the defect holes by way of several conformal monolayer attachment steps. Two biomolecules, 3-APTES and sulfo-SMCC, were used to demonstrate

sensitivity to monolayers of $\sim$1 nm in thickness, as well as prepare the surfaces for label-free detection of thiol-bound molecules. The devices were first tested using the native oxide on the silicon slab surface, which resulted in a 44% increase in sensitivity to 3-APTES attachment for the MHD PhC with 67 nm diameter defect holes, with respect to a L3 cavity without defect holes. In order to increase the surface binding efficiency, a test tube ALD method was utilized to conformally coat the surfaces of the slab with 5-6 nm of silicon dioxide. The resulting MHD PhCs with improved oxide coverage and 500 nm defect hole lateral spacing demonstrated up to 120% improvement in cumulative resonance shift after 3-APTES attachment, with respect to L3 cavities with no defect holes. By further optimizing the cavity design and placing the defect holes at 380 nm lateral spacing, corresponding to the optimal position of the holes relative to the cavity mode, the sensitivity to 3-APTES attachment was increased to 160% with respect to the L3 cavity. The addition of the defect holes have clearly shown that for surface sensing, small defect holes placed at the optimal locations can significantly increase the sensitivity of the device to molecule attachment.

CHAPTER 6

CONCLUSION

6.1 Summary

In this work, photonic crystal (PhC) slabs with multiple-hole defects (MHD) were investigated by carrying out device simulation, design, fabrication, and measurement. The integration of MHD into PhC cavities is motivated by the desire to increase light-matter interaction (LMI) by creating high surface area regions which directly overlap spatially with the highest intensity regions of the modal field. Photonic crystal slab cavities are chosen due to their high quality factors and small mode volumes, which increase the time duration of light matter interaction while keeping a small device footprint. FDTD simulations were first carried out in two dimensions to examine the effect of integrating sub-wavelength sized holes that are smaller than the lattice holes directly into a PhC cavity. The size, spacing, and placement of these defect holes were generated by using a `python` script in order to create circular MHD regions, in the place of a single removed photonic crystal lattice hole. High-resolution simulations were used in order to resolve the very small defect holes, and various defect hole sizes and spacings were simulated in order to understand the trade-offs in device design. By changing the dielectric constant of the defect holes in the cavity, thereby changing the effective index of the defect region, the sensitivity of various designs can be measured by tracking the change of the resonance frequency. It was found increasing the radius of the effective defect region from of $r = 0.2a$ to $r = 0.4a$ (where a is the lattice constant), the slope of the resonance frequency shift due to changing dielectric constant is increased. This is expected, since creating a larger MHD region requires the addition of more holes, which lowers the overall modal index more efficiently. Although a larger

frequency shift and accordingly a large device sensitivity are desired, it was found that this trend comes with a trade-off of decreasing cavity Q. When the effective size of the MHD region becomes too large, the modal frequency shifts towards the air-band edge, creating more leakage in the cavity. Therefore it was concluded that although surface area can be improved by several times compared to a single hole defect, depending on the application, the proper MHD design should be chosen to most appropriately balance requirements for high Q or high sensitivity. To further explore the sensitivity of MHD PhCs, the resonance shift due to surface monolayer attachment, which can represent molecular binding in the defect holes, was compared for two cavities: a SHD with a defect hole radius of $0.2a$, and a MHD with effective radius $0.2a$. A single monolayer of material was modeled inside of the defect holes by assuming an effective medium in the defect holes, due to the relative thinness of the monolayer with respect to the defect hole radius. As a result, the effective index of the defect holes increases with the optical thickness of the monolayer. It was found that for the similar sized cavities addition of a monolayer of material leads to an approximately 3 times larger resonance shift for the MHD compared to the SHD due to the increased surface area in the cavity. The Q trend of the cavities was found to converge to a maximum value as the dielectric constant of the defect holes reaches $\varepsilon = 12$. Also, the slope of the Q as a function of defect hole ε was found to vary depending on the effective defect radius of the MHD. Smaller effective radii (less defect holes) had higher Q values in general due to less perturbation inside of the cavity, while larger effective radii (and more defect holes) reduced the Q significantly. Through this simulated experiment, it was confirmed that MHD cavities can offer a significant increase in sensitivity to surface perturbations, and that light matter interaction is improved.

The 2D simulations of H1-type MHD PhC cavities demonstrated increased LMI and sensitivity to surface perturbations relative to traditional SHD PhC defects. However, the

dimensions of the features necessary to fabricate these simulated devices are limited from a design standpoint. Because the ideal measurement wavelength range is in the near-IR, some of the smallest features in the simulated cavities would require defect holes with 8 nm radius and ∼30:1 aspect ratios, which are extremely difficult to realize in the current CMOS fabrication process. Therefore, a new design was chosen using L3 cavities in air-clad silicon PhC slabs, which have a larger sensing area for the placement of defect holes and are known for their previously well-studied high Q characteristics. To understand the effect of increasing the number, size, and location of the defect holes within the L3 cavity, 3D FDTD simulations were performed to find the modal field distribution first for the L3 cavity without defect holes, as well as the resonance wavelength and Q_{int} of the L3 cavity. For a lattice constant of 410 nm, lattice hole radius of 105 nm, and slab thickness of 220 nm, the L3 cavity had a resonance wavelength of 1539.5 nm and a Q_{intr} value of 25,300. The simulated field showed three main regions of peak field intensity within the cavity. Accordingly, three defect holes located in these regions were chosen as the main design for the MHD cavities. The degree of spatial LMI depends on the positioning of the defect holes and the intensity of the field overlapping with them. Therefore in order to optimize the defect hole location within the vicinity of the peak field regions inside the L3 cavity, simulations are run in which the lateral spacing of two defect holes on either side of a central defect hole is changed from 180-500 nm in steps of 40 nm. It was found that for the lattice hole radius of 105 nm, the optimal defect hole location in the L3 cavity is a lateral spacing of 380 nm from center, which causes the largest resonance blueshift of 22 nm. This also corresponds to the largest device sensitivity, since the shift is a result of the reduced modal index due to material removal, and the shift due to material addition follows the same trend. The simulated Q_{intr} of the cavities was also maximized to a value of 43,500 at 380 nm, which is nearly twice the value of the L3 cavity Q_{intr}. The improvement

in Q is attributed to the discontinuity of the electric field at the air/silicon interface, which causes a concentrated field intensity in the air region due to the direct overlap of the defect holes and the highest intensity of the mode. With the proper placement of defect holes, the field in a PhC cavity can potentially be enhanced. Hence, for the MHD designs of three properly placed defect holes in an L3 cavity, it is possible to both increase the surface area of the PhC, which will lead to higher sensitivity detection of molecular binding events, and increase the Q of the cavity.

Devices were fabricated on SOI substrates using e-beam lithography, with designs consisting of L3 cavities with SHD and MHD, and measured in an air cladding background. The first designs consisted of 3-hole MHD cavities with an unoptimized spacing of 470 nm. Different doses were used on the same wafer, in order to produce a variety of lattice hole sizes and defect hole radii. The fabricated L3 MHD cavities had resonances ranging from 1550-1580 nm depending on the defect hole size, and had Q_{load} values as high as 6,500$\pm$200 for the initial designs. The Q_{load} value is diminished compared to the simulated intrinsic Q due to the coupling loss to the waveguide, as well as scattering from fabrication imperfections. Several general trends were confirmed by measuring the MHD PhC devices with various defect hole sizes and spacings. Due to the decreasing cavity effective mode index, as the defect hole radii is increased the resonance blue-shifts in wavelength. Cavities fabricated with several different lateral spacings in the MHD confirmed that for a defect hole lateral spacing of 380 nm, corresponding to the spatial location of the maximum cavity mode intensity, the resonance blueshift as well as the Q_{load} are maximized. The value of Q_{load} can potentially be increased compared to the L3 cavity without defect holes, as shown by the measured Q_{load} of 8,000 in the case of the optimized location compared to the L3 cavity Q_{load} of $\sim$1,000. Through the passive measurements, it was shown that defect holes, and increased surface area, can be integrated directly into a PhC cavity without

severe degradation of quality factor.

Next, sensing measurements were carried out to quantify the sensitivity of the light matter interaction in the cavity region, and the enhancement due to addition of MHD with the L3 PhC cavity. First, bulk sensing performance was investigated by infiltrating the air cladding regions, lattice holes, and defect holes in the PhC slab using various solutions of DI water, isopropyl alcohol, methanol, and index-matching silicone oil. FDTD simulations of MHD PhCs with different index backgrounds showed a quadratic dependence on the bulk refractive index for the resonance wavelength of the cavity. Because of the quadratic trend, analyzing the resonance wavelength shift due to a large index contrast change (e.g., air to water) can underestimate the expected small signal sensitivity of the MHD PhC to small index perturbations such as those due to binding of small molecules. For a large index change shift (air to silicone oil), sensitivity values were measured to be 91 nm/RIU for the SHD PhC and 98 nm/RIU for the MHD PhC. Both SHD and MHD PhCs were found to have greater sensitivity than the L3 cavities without defect holes (83 nm/RIU), showing that even the addition of a single hole is beneficial for bulk sensing. The expected trend of increasing sensitivity with larger defect holes was also confirmed through measurements. In comparison to similar L3 cavity-based sensors, the MHD and SHD cavities outperform previously published values, and the high-Q of the cavity offers higher detection limits. However, the small, sub-wavelength sized defect holes in the MHD are not optimized for bulk sensing, as the volume of direct interaction between the modal field and fluid is limited in a small hole, and the Q is reduced significantly due to increased scattering and absorption. Subsequently, surface sensing measurements were carried out next using 3-APTES (0.8 nm molecule) and sulfo-SMCC (1.2 nm molecule) monolayer attachment to the silicon slab surface. Initially, the native oxide was used for the 3-APTES attachment step, which showed a 44% increase in resonance shift in the unoptimized MHD cavity (500 nm spac-

ing) with 67 nm defect hole diameter, with respect to the L3 cavity baseline. The oxide coverage on the surface was further improved by using an in-hood room temperature silicon dioxide ALD process, which enabled the deposition of 6 nm of conformal oxide on the surface. With the ALD oxide coverage, the sensitivity of the unoptimized device to 3-APTES attachment was increased to 80% for a 55 nm defect hole diameter, and 120% for 60 nm diameter. Finally, for the fully optimized device with 380 nm defect hole spacing, the resonance shift was measured to have a 160% percent increase with respect to the L3 cavity. This result clearly demonstrates that the sensitivity to surface perturbation is increased due to the enhanced binding from ALD oxide coverage, the added surface area afforded by MHD, and the direct overlap with analyte and the cavity mode.

6.2 Future Work

6.2.1 Device Improvements

Although this work represents a significant contribution to the understanding of LMI in PhC structures and provides guidelines for developing PhC-based sensors with increased sensitivity to surface perturbations, several opportunities exist for improvements and new directions. In particular, tuning the parameters of the fabricated photonic lattice can potentially increase the Q of the measured cavities. Initial simulations have shown that for a lattice constant of 410 nm, a lattice hole radius of 137 nm can increase the Q_{intr} of the L3 cavity to $\sim$37,500, compared to 25,000 for the lattice with 105 nm radius holes. This would blueshift the resonance to 1453 nm, so appropriate sources are necessary to measure the transmission. Different configurations of the currently used waveguide/cavity coupling mechanism can also be explored. Currently, the devices are fabricated in a drop-cavity configuration, with the cavity located 4 rows of holes away from the waveguide. Previously it has been shown that adding another access waveguide to the other side of the cavity can

allow the dropped resonant mode to couple to a separate output, allowing only the resonant mode to be measured. Measuring the Q_{load} of the isolated resonance can be easier than measuring from a dip in the transmission, because the peak of the resonant wavelength is easily resolved and not corrupted by the noise floor of the detector or OSA. Alternatively, the vertically emitted modal field can be collected by positioning an objective directly over the cavity region and measuring the light with a spectrometer, which allows direct analysis of the cavity Q. For measuring high Q cavities this may be the preferred method, as adding a separate access waveguide introduces additional Q_{loss}. Methods have also been developed which use a IR-sensitive camera to measure the scattered light from the surface of photonic devices and correlate the intensity of the pixels as a function of wavelength to the cavity resonance spectrum. Finally, fabrication using electron beam lithography is accurate yet costly, so the development of more conventional processing using optical lithography and stepper technology can be applied for cheaper device production on a larger scale. In particular, this may prove difficult to apply to photonic crystals, because the accuracy in the lattice and defect hole sizes is critical for repeatability and any errors can cause losses in the device.

6.2.2 Specific Label-Free Detection

Specific detection using MHD PhCs presents several challenges which need to be overcome. Although the functionalization of the surface for thiol-bound molecules has been demonstrated here, the chemistries which enable small-molecule attachment in other platforms may not necessarily apply to MHD PhCs. New recipes for binding molecules to the small defect region may need to be developed, specific to the SOI material platform and the air-bridge construction of the devices. In particular, the label-free detection of DNA probe/-target molecules would demonstrate the sensitivity of MHD PhCs. Unfortunately, because

the surface area of the defect region is limited, fluidics or other methods may be necessary to specifically target the cavity region of MHD PhCs, in order to ensure effective molecule binding. Also, the binding steps necessary for surface functionalization reduce the overall radius of each defect/lattice hole, and the binding efficiency of successive attachment steps is reduced. For effective label-free sensing, care must be taken that the amount of attachment sites is not degraded by the functionalization steps; that is, the functionalization efficiency should be kept to a high value.

6.2.3 MHD in Other Photonic Devices

Opportunities exist for the application of the MHD concept to other silicon photonics devices such as PhC heterostructure cavities, resonant rings and disks, or interference structures such as Mach-Zehnder interferometers. In particular, the PhC heterostructure devices have shown the highest values of Q, which can potentially drive smaller detection limits for sensing applications. The drawback to using these types of cavities is the precise fabrication tolerances necessary, as previously mentioned. Integrated photonic waveguides have potential for MHD integration as well, since the spatial overlap with surface perturbations is limited because the majority of the mode is localized inside the core of the waveguide. Adding defect holes would increase the light matter interaction in any device which is fundamentally waveguide-based such as ring resonators and would enable delivery of analyte directly to the waveguide mode for sensing applications. Furthermore, disk and square-shaped compact resonators can potentially bring even larger initial surface areas for analyte binding. The location of the defect holes in these cases would require much study, because unlike PhC cavities they are multi-moded due to being traveling wave cavities, and the ideal placement of holes is not so obvious. One approach may be to analyze the average field over several time steps for a finite number of modes using FDTD. The consequences of

using such devices may be limited bandwidth over which the mode has the highest average spatial overlap with the defect holes. Finally, functionalization of photonic device surfaces based on other material systems such as silicon nitride or III-V materials, can potentially be enabled using the ALD oxidation method used in Chapter 5. Once ALD oxide is deposited, known methods for oxidized silicon surfaces can be utilized in sensing measurements.

6.2.4 Microfluidics Integration

While sensing experiments in laboratory conditions can be carried out easily in real-time, tests which occur in a hospital environment or in the field would require quick, easy to use sensors which simplify measurement procedures. A single-chip system with integrated microfluidics which can be easily transported would be advantageous over current solutions such as surface plasmon resonance, which currently can only be carried out using laboratory-size apparatus. Microfluidic reservoirs on-chip also help to prevent the waste of analyte which needs to be conserved. Work such as that of Erickson et al. [89] and Smith et al. [90] have previously shown that integration of photonics with microfluidics is possible, in order to create lab-on-a-chip systems [39, 91–93].

MHD PhC devices with microfluidics are proposed in order to create a highly sensitive device that can detect biomolecules in real-time. Polydimethylsiloxane (PDMS), which has been shown to be useful in fast and easy fabrication of flexible elastomer layers which can bond to silicon, can be used to create layers of microfluidic channels for carrying analyte in/out of the PhC MHD regions. If PhC devices are laid out in a linear fashion on a photonic chip, a single channel can be used for several different measurements at once. Alternatively, separate openings in the PDMS can be used to access each cavity individually. The ability to probe multiple devices at once could open the door to several individually functionalized devices which can detect different analyte molecules at the same time. By using a drop

filter configuration as mentioned in the previous section, multiple resonances from several devices can also be combined into one signal in the output. This method of multiplexing multiple resonators has been previously used in devices using ring resonators as the drop filter [94, 95]. By isolating the resonance mode using a drop cavity, on-chip integrated detectors can be placed at each device's output waveguide, enabling fingerprinting of the analyte solution depending on which molecules are specifically captured by examining the resonance shift of each device. Advances in silicon processing technology have enabled on-chip, monolithic fabrication of both silicon photonic and CMOS components together, which would enable real-time detection using electro-optic signals.

APPENDIX A

SIMULATION CODE

For all code, an ellipsis ('...') denotes a continuing line. All dimensions are normalized to the lattice constant, so that $a = 1$ in the resulting code.

A.1 gen_phc_rect.py

`gen_phc_rect.py` generates PhC lattices in a triangular basis for importing to `meep`.

```
#! /usr/bin/env python

# output to file, meep geometries for a photonic crystal slab
# in a triangular basis.

# input variables:
#       xlen, ylen - number of holes in each direction (odd numbers)

def gen_phc_rect(xlen, ylen):
    xrange, yrange = (xlen - 1)/2, ((ylen - 1)/4)*3**0.5

    for i in range(-2*xlen, 2*xlen):
        for j in range (-2*ylen, 2*ylen):
              xcoord = i*(0.5)+j*(0.5)
              ycoord = i*(-3**0.5 / 2)+j*(3**0.5 / 2)

              if abs(xcoord) <= xrange:
                  if abs(ycoord) <= yrange:
                      print '(list (make cylinder ...
                          (center %f %f)(material air)(radius r) ...
                          (height ts)))' % (xcoord,ycoord)

gen_phc_rect(15,9)  # example usage
```

A.2 mpb_pcs_bands.ctl

`mpb` code for generating band structures of slab PhCs. A unit cell consists of a single lattice hole in the slab.

```
(set! num-bands 30)
(set! tolerance 1e-8)
(set! k-points (list (vector3 0 0 0)
                     (vector3 0 0.5 0)
                     (vector3 (/ -3) (/ 3) 0)
                     (vector3 0 0 0) ))

; command line parameters entered in nm for convenience
(define-param r-nm 105) ; hole radius
(define-param a-nm 410) ; lattice constant
(define-param h-nm 220) ; slab thickness

; normalizing to lattice constant for internal use
(define-param h (/ h-nm a-nm))
(define-param r (/ r-nm a-nm))

(define-param epssi 11.9)   ; refractive index of the slab
(define-param epsox 1)    ; refractive index of surrounding

(set! default-material (make dielectric (epsilon epsox)))

(set! k-points (interpolate 16 k-points))

(set! geometry-lattice (make lattice (size 1 1 4)
                         (basis1 (/ (sqrt 3) 2) 0.5)
                         (basis2 (/ (sqrt 3) 2) -0.5)
))

(set! geometry (list
       (make block
               (center 0 0 0) (size infinity infinity h)
               (material (make dielectric (epsilon epssi))))
       (make cylinder
               (center 0 0 0) (radius r) (height h)
               (material (make dielectric (epsilon epsox))))
))

(set! geometry (append
       (geometric-objects-lattice-duplicates geometry 1 1 4)
))

(set-param! resolution 16)

; calculate both polarizations
(run-te)
(run-tm)
```

A.3 mpb_pcs_w1_bands.ctl

mpb code for generating band structures of slab PhCs W1 waveguides. Because of the broken symmetry, the unit cell consists of one row of the PhC, normal to the direction of guiding, with one hole filled in.

```
; command line parameters entered in nm for convenience
(define-param r-nm 105) ; hole radius
(define-param a-nm 410) ; lattice constant
(define-param h-nm 220) ; slab thickness

; normalizing to lattice constant for internal use
(define-param h (/ h-nm a-nm))
(define-param r (/ r-nm a-nm))

(define-param epssi 11.9)   ; refractive index of the slab
(define-param epsox 1)    ; refractive index of surrounding

(set! default-material (make dielectric (epsilon epsox)))

(set! num-bands 30)
(set! tolerance 1e-8)

(set! k-points (list (vector3 0 0 0)
                     (vector3 0.5 0 0)))
(set! k-points (interpolate 20 k-points))

(set! geometry-lattice (make lattice (size 1 16 4)
                         (basis1 (/ (sqrt 3) 2) 0.5)
                         (basis2 (/ (sqrt 3) 2) -0.5)))

(set! geometry (list
       (make block
             (center 0 0 0) (size infinity infinity h)
             (material (make dielectric (epsilon epssi))))
       (make cylinder
             (center 0 0 0) (radius r) (height h)
             (material (make dielectric (epsilon epsox))))
))

(set! geometry
           (geometric-objects-lattice-duplicates geometry 1 1 4))
(set! geometry
           (append geometry (list (make cylinder (center 0 0 0)
           (radius r) (height h)
           (material (make dielectric (epsilon epssi)))
```

```
))))

(set-param! resolution (vector3 16 16 16))

; calculate both polarizations
(run-te)
(run-tm)
```

A.4 meep_cavity_varepsilon_mhd.ctl

meep code for calculating the resonance frequency and quality-factors of L3-type MHD PhCs. harminv is called after the initial simulation time in order to extract ω_0 and Q. The output of gen_phc_rect.py must be copied/pasted into the specified lines.

```
(define-param t-nm 220)
(define-param a-nm 410)
(define-param r-nm 100)
(define-param r-defnm 30.0)
(define-param mhd-nm 503)

(define-param ts (/ t-nm a-nm))
(define-param a 1)
(define-param r (/ r-nm a-nm))
(define-param rdef (/ r-defnm a-nm))
(define-param mhd-x (/ mhd-nm a-nm))

(define-param dpml 2.0)
(define-param fcen 0.26)
(define-param df 0.05)
(define-param eps 11.56)
(define-param epsair 1.0)  ;eps of holes
(define-param epsbkgnd 1.0) ;eps of default
(define-param epsdh 1.0) ;eps of defect holes
(define-param size-x 25)
(define-param size-y (* 8 (sqrt 3)))
(define-param size-z (* (+ ts dpml) 2))

(define-param res 16)

(set! default-material (make dielectric (epsilon epsbkgnd)))

(set! geometry-lattice (make lattice (size size-x size-y size-z)) )

(set! geometry (append
(list (make block
```

```
           (center 0 0 0)(size infinity infinity ts)
           (material (make dielectric (epsilon eps)))
))

;;;;;;;;;;;;;;;;;;;;;;;;;;;;;;;;;;;;;;;;;;;;;;;;;;;;;;;;;;;;;;;;;;;;
;;;;;;;;;;; OUTPUT FROM gen_phc_rect.py HERE ;;;;;;;;;;;
;;;;;;;;;;;;;;;;;;;;;;;;;;;;;;;;;;;;;;;;;;;;;;;;;;;;;;;;;;;;;;;;;;;;

; add SHD
(list (make cylinder (center 0 0)
      (material (make dielectric (epsilon epsdh)))
      (radius rdef)(height ts)))
; add MHD
(list (make cylinder (center mhd-x 0)
      (material (make dielectric (epsilon epsdh)))
      (radius rdef)(height ts)))
(list (make cylinder (center (* -1 mhd-x) 0)
      (material (make dielectric (epsilon epsdh)))
      (radius rdef)(height ts)))

)) ; end set-geometry

(set! sources (list
      (make source
         (src (make gaussian-src (frequency fcen)(fwidth df) ))
         ;uncomment for CW source:
         ;(src (make continuous-src (frequency fcen)))
         (component Ey)
         (center -0.15 -0.15 0))
))

(set! symmetries (list
        (make mirror-sym (direction Z))
))

(set! pml-layers (list (make pml (thickness dpml))))

(set-param! resolution res)

(use-output-directory)

;;;;;;;;;;;;; gaussian pulse, find resonance
(run-sources+ 1000
     (at-beginning output-epsilon)
     (after-sources (harminv Ey (vector3 0.0 0.0 0.0) fcen df)
     (harminv Ey (vector3 0.15 0.15 0.0) fcen df)))
```

```
(run-until (/ 1 fcen)(at-every (/ 1 fcen 40) output-efield-y))

;;;;;;;;;;;;; cw, show fields in cavity
;(run-until (/ 1 fcen) (at-every (/ 1 fcen 40) output-efield-y))
```

BIBLIOGRAPHY

[1] C. A. Barrios, V. R. Almeida, R. Panepucchi, and M. Lipson. Electrooptic modulation of silicon-on-insulator submicrometer-size waveguide devices. *J. Lightwave Tech.*, 21(10):2332–2339, 2003.

[2] W. M. J. Green, M. J. Rooks, L. Sekaric, and Y. A. Vlasov. Ultra-compact, low rf power, 10 gb/s silicon mach-zehnder modulator. *Opt. Express*, 15(25):17106–17113, 2007.

[3] Q. Xu, B. Schmidt, S. Pradhan, and M. Lipson. Micrometre-scale silicon electro-optic modulator. *Nature*, 435(7040):325–327, May 2005.

[4] V. R. Almeida, Q. Xu, and M. Lipson. Ultrafast integrated semiconductor optical modulator based on the plasma-dispersion effect. *Opt. Lett.*, 30(18):2403–2405, 2005.

[5] K. Sokolowski-Tinten and D. von der Linde. Generation of dense electron-hole plasmas in silicon. *Phys. Rev. B*, 61(4):2643–2650, 2000.

[6] E. Krioukov, D. J. W. Klunder, A. Driessen, J. Greve, and C. Otto. Sensor based on an integrated optical microcavity. *Opt. Lett.*, 27:512–514, 2002.

[7] F. Vollmer, D. Braun, A. Libchaber, M. Khoshsima, I. Teraoka, and S. Arnold. Protein detection by optical shift of a resonant microcavity. *Appl. Phys. Lett.*, 80:4057–4059, 2002.

[8] A. Ksendzov and Y. Lin. Integrated optics ring-resonator sensors for protein detection. *Opt. Lett.*, 30:3344–3346, 2005.

[9] K. De Vos, I. Bartolozzi, E. Schacht, P. Bienstman, and R. Baets. Silicon-on-insulator microring resonator for sensitive and label-free biosensing. *Opt. Express*, 15:7610–7615, 2007.

[10] A. L. Washburn, L. C. Gunn, and R. C. Bailey. Label-free quantitation of a cancer biomarker in complex media using silicon photonic microring resonators. *Anal. Chem.*, 81:9499–9506, 2009.

[11] C. A. Barrios, M. J. Bañuls, V. Gonzáles-Pedro, K. B. Gylfason, B. Sánchez, A. Griol, A. Maquieira, H. Sohlström, M. Holgado, and R. Casquel. Label-free optical biosensing with slot-waveguides. *Opt. Lett.*, 33:708–710, 2008.

[12] T. Claes, J. G. Molera, K. De Vos, E. Schacht, R. Baets, and P. Bienstman. Label-free biosensing with a slot-waveguide-based ring resonator in silicon on insulator. *IEEE Photonics Journal*, 1:197–204, 2009.

[13] R. G. Heideman, R. P. H. Kooyman, and J. Greve. Performance of a highly sensitive optical waveguide mach-zehnder interferometer immunosensor. *Sens. Act. B*, 10:209–217, 1993.

[14] E. F. Schipper, A. M. Brugman, C. Dominguez, L. M. Lechuga, R. P. H. Kooyman, and J. Greve. The realization of an integrated mach-zehnder waveguide immunosensor in silicon technology. *Sens. Act. B*, 40:147–153, 1997.

[15] B. J. Luff, J. S. Wilkinson, J. Piehler, U. Hollenback, J. Ingenhoff, and N. Fabricius. Integrated optical mach-zehnder biosensor. *J. Lightwave Tech.*, 16:583–592, 1998.

[16] E. Yablonovitch. Inhibited spontaneous emission in solid-state physics and electronics. *Phys. Rev. Lett.*, 58:2059–2062, 1987.

[17] S. John. Strong localization of photons in certain disordered dielectric superlattices. *Phys. Rev. Lett.*, 58:2486–2489, 1987.

[18] J.D. Joannopoulos, S. G. Johnson, J. N. Winn, and R. D. Meade. *Photonic Crystals: Molding the Flow of Light*. Princeton University Press, 2nd edition, 2008.

[19] Y. A. Vlasov, X. Bo, J. C. Sturm, and D. J. Norris. On-chip natural assembly of silicon photonic bandgap crystals. *Nature*, 414:289–293, 2001.

[20] J. S. King and E. Graugnard C. J. Summers. Tio2 inverse opals fabricated using low-temperature atomic layer deposition. *Adv. Mater.*, 17:1010–1013, 2005.

[21] S. Y. Lin, J. G. Fleming, D. L. Hetherington, B. K. Smith, R. Biswas, K. M. Ho, M. M. Sigalas, W. Zubrzycki, S. R. Kurtz, and J. Bur. A three-dimensional photonic crystal operating at infrared wavelengths. *Nature*, 394:251–253, 1998.

[22] K. M. Ho, C. T. Chan, C. M. Soukoulis, R. Biswas, and M. Sigalas. Photonic band gaps in three dimensions: new layer-by-layer periodic structures. *Solid State Communications*, 89(5): 413–416, 1994.

[23] S. Noda, K. Tomoda, N. Yamamoto, and A. Chutinan. Full three-dimensional photonic bandgap crystals at near-infrared wavelengths. *Science*, 289(5479):604–606, 2000.

[24] M. H. Qi, E. Lidorikis, P. T. Rakich, S. G. Johnson, J. D. Joannopoulos, E. P. Ippen, and H. I. Smith. A three-dimensional optical photonic crystal with designed point defects. *Nature*, 429 (6991):538–542, June 2004.

[25] S. G. Johnson, S. H. Fan, P. R. Villeneuve, J. D. Joannopoulos, and L. A. Kolodziejski. Guided modes in photonic crystal slabs. *Physical Review B*, 60(8):5751–5758, August 1999.

[26] S. Assefa, P. T. Rakich, P. Bienstman, S. G. Johnson, G. S. Petrich, J. D. Joannopoulos, L. A. Kolodziejski, E. P. Ippen, and H. I. Smith. Guiding 1.5μm light in photonic crystals based on dielectric rods. *Appl. Phys. Lett.*, 85(25):1840107, 2004.

[27] S. J. McNab, N. Moll, and Y. A. Vlasov. Ultra-low loss photonic integrated circuit with membrane-type photonic crystal waveguides. *Opt. Express*, 11(22):2927–2939, November 2003.

[28] I. W. Jung, S. Kim, and O. Solgaard. High reflectivity broadband photonic crystal mirror mems scanner. In *Solid-State Sensors, Actuators and Microsystems Conference, 2007. TRANSDUCERS 2007. International*, pages 1513–1516, June 2007.

[29] M. Lipson and C. R. Pollock. *Integrated Photonics*. Kluwer Academic Publishers, 2003.

[30] A. Mekis, J. C. Chen, I. Kurland, S. Fan, P. R. Villeneuve, and J. D. Joannopoulos. High transmission through sharp bends in photonic crystal waveguides. *Phys. Rev. Lett.*, 77:3787–3790, 1996.

[31] M. Notomi, K. Yamada, A. Shinya, J. Takahashi, C. Takahashi, and I. Yokohama. Extremely large group-velocity dispersion of line-defect waveguides in photonic crystal slabs. *Phys. Rev. Lett.*, 87(25), December 2001.

[32] C. Manolatou, M. J. Khan, S. Fan, P. R. Villeneuve, H. A. Haus, and J. D. Joannopoulos. Coupling of modes analysis of resonant channel add-drop filters. *IEEE J. Quant. Elect.*, 35 (9):1322–1331, September 1999.

[33] S. Fan, P. R. Villeneuve, J. D. Joannopoulos, M. J. Khan, C. Manolatou, and H. A. Haus. Theoretical analysis of channel drop tunneling processes. *Phys. Rev. B*, 59(24):15882–15892, June 1999.

[34] V. R. Almeida, C. A. Barrios, R. R. Panepucci, M. Lipson, M. A. Foster, D. G. Ouzounov, and A. L. Gaeta. All-optical switching on a silicon chip. *Optics Letters*, 29(24):2867–2869, December 2004.

[35] V. R. Almeida, C. A. Barrios, R. R. Panepucci, and M. Lipson. All-optical control of light on a silicon chip. *Nature*, 431:1081–1084, 2004.

[36] Y. Vlasov, W. M. J. Green, and F. Xia. High-throughput silicon nanophotonic wavelength-insensitive switch for on-chip optical networks. *Nature Photonics*, 2(4):242–246, April 2008.

[37] Y. Akahane, M. Mochizuki, T. Asano, Y. Tanaka, and S. Noda. Design of a channel drop filter by using a donor-type cavity with high-quality factor in a two-dimensional photonic crystal slab. *Appl. Phys. Lett.*, 82:1341–1343, 2003.

[38] T. Hasek, H. Kurt, D. S. Citrin, and M. Koch. Photonic crystals for fluid sensing in the subterahertz range. *Appl. Phys. Lett.*, 89:173508, 2006.

[39] N. Skivesen, A. Tetu, M. Kristensen, J. Kjems, L. H. Frandsen, and P. I. Borel. Photonic-crystal waveguide biosensor. *Optics Express*, 15(6):3169–3176, March 2007.

[40] S. C. Buswell, V. A. Wright, J. M. Buriak, V. Van, and S. Evoy. Specific detection of proteins using photonic crystal waveguides. *Opt. Express*, 16:15949–15957, 2008.

[41] T. Asano, B-S. Song, Y. Akahane, and S. Noda. Ultrahigh-q nanocavities in two-dimensional photonic crystal slabs. *IEEE J. Sel. Top. Quantum Electron.*, 12:1123–1134, 2006.

[42] Y. Takahashi, H. Hagino, Y. Tanaka, B-S. Song, T. Asano, and S. Noda. High-q nanocavity with a 2-ns photon lifetime. *Opt. Express*, 15(25):17206–17213, 2007.

[43] X. Wang, Z. Xu, N. Lu, J. Zhu, and G. Jin. Ultracompact refractive index sensor based on microcavity in the sandwiched photonic crystal waveguide structure. *Opt. Comm.*, 281:1725–1731, 2008.

[44] E. Chow, A. Grot, L. W. Mirkarimi, M. Sigalas, and G. Girolami. Ultracompact biochemical sensor built with two-dimensional photonic crystal microcavity. *Opt. Lett.*, 29:1093–1095, 2004.

[45] M. Lončar, A. Scherer, and Y. Qiu. Photonic crystal laser sources for chemical detection. *Appl. Phys. Lett.*, 82:4648–4650, 2003.

[46] S. Kita, K. Nozaki, and T. Baba. Refractive index sensing utilizing a cw photoniccrystal nanolaser and its array configuration. *Opt. Express*, 16(11):8174–8180, 2008.

[47] M. Adams, G. A. DeRose, M. Lončar, and A. Scherer. Lithographically fabricated optical cavities for refractive index sensing. *J. Vac. Sci. Technol. B*, 23(6):3168–3173, 2005.

[48] D. F. Dorfner, T. Hürlimann, T. Zabel, L. H. Frandsen, G. Abstreiter, and J. J. Finley. Silicon photonic crystal nanostructures for refractive index sensing. *Applied Physics Letters*, 93(18): 181103, 2008.

[49] Y. Akahane, T. Asano, B-S. Song, and S. Noda. Investigation of high-q channel drop filters using donor-type defects in two-dimensional photonic crystal slabs. *Appl. Phys. Lett.*, 83(8): 1512–1514, 2003.

[50] M. Lee and P. M. Fauchet. Two-dimensional photonic crystal based biosensing platform for protein detection. *Opt. Express*, 15:4530–4535, 2007.

[51] M. R. Lee and P. M. Fauchet. Nanoscale microcavity sensor for single particle detection. *Opt. Lett.*, 32(22):3284–3286, 2007.

[52] V. B. Braginsky, M. L. Gorodetsky, and V. S. Ilchenko. Quality-factor and nonlinear properties of optical whispering-gallery modes. *Phys. Lett. A*, 137:393–397, 1989.

[53] D. K. Armani, T. J. Kippenberg, S. M. Spillane, and K. J. Vahala. Ultra-high-q toroid microcavity on a chip. *Nature*, 421:925–928, 2003.

[54] M. L. Gorodetsky, A. A. Savchenkov, and V. S. Ilchenko. Ultimate q of optical microsphere resonators. *Opt. Lett.*, 21(7):453–455, 1996.

[55] V. Lehmann. *Electrochemistry of Silicon: Instrumentation, Science, Materials and Applications*. Wiley-VCH, Weinheim, Germany, 2002.

[56] G. Rong, A. Najmaie, J. E. Sipe, and S. M. Weiss. Nanoscale porous silicon waveguides for label-free dna sensing. *Biosens. Bioelectron.*, 23:1572, 2008.

[57] G. Rong and S. M. Weiss. Optical dna sensing based on resonant porous silicon structures. *Proc. of SPIE*, 6477:647717–1, February 2007.

[58] G. Rong, J. D. Ryckman, R. L. Mernaugh, and S. M. Weiss. Label-free porous silicon membrane waveguide for dna sensing. *Appl. Phys. Lett.*, 93:161109, 2008.

[59] S. M. Weiss, J. Zhang, P. M. Fauchet, V. V. Seregin, and J. L. Coffer. Tunable silicon-based light sources using erbium doped liquid crystals. *Appl. Phys. Lett.*, 90:031112, 2007.

[60] S. M. Weiss and P. M. Fauchet. Porous silicon one-dimensional photonic crystals for optical signal modulation. *IEEE J. Sel. Top. Quantum Electron.*, 12(6):1514–1519, 2006.

[61] S. M. Weiss, M. Haurylau, and P. M. Fauchet. Tunable photonic bandgap structures for optical interconnects. *Opt. Mat.*, 27:740, 2005.

[62] J.-H. Park, L. Gu, G. v. Maltzahn, E. Ruoslahti, S. N. Bhatia, and M. J. Sailor. Biodegradable luminescent porous silicon nanoparticles for *in vivo* applications. *Nature Mat.*, 8:331–336, 2009.

[63] J. C. M. Garnett. Colours in metal glasses and in metallic films. *Philos. Trans. Roy. Soc. London A*, 203:385–420, 1904.

[64] O. Levy and D. Stroud. Maxwell garnett theory for mixtures of anisotropic inclusions: Application to conduction polymers. *Phys. Rev. B*, 56:8035–8046, 1997.

[65] Mpb - abinitio, 4/22/2011. URL `http://ab-initio.mit.edu/mpb/`.

[66] S. G. Johnson and J. D. Joannopoulos. Block-iterative frequency-domain methods for maxwell's equations in a planewave basis. *Opt. Express*, 8:173–190, 2001.

[67] A. Taflove and S. C. Hagness. *Computational Electrodynamics: The Finite-Difference Time-Domain Method*. Artech, 2000.

[68] Meep - abinitio, 4/22/2011. URL `http://ab-initio.mit.edu/meep/`.

[69] A. Farjadpour, D. Roundy, A. Rodriguez, M. Ibanescu, P. Bernel, J. D. Joannopoulos, S. G. Johnson, and G. Burr. Improving accuracy by subpixel smoothing in fdtd. *Opt. Lett.*, 31: 2972–2974, 2006.

[70] J. Berenger. A perfectly matched layer for the absorptino of electromagnetic waves. *J. Comput. Phys.*, 114:185–200, 1994.

[71] Harminv - abinitio, 4/22/2011. URL `http://ab-initio.mit.edu/harminv/`.

[72] V. A. Mandelshtam and H. S. Taylor. Harmonic inversion of time signals. *J. Chem. Phys.*, 107:6756–6769, 1997.

[73] Y. Akahane, T. Asano, B. Song, and S. Noda. High-q photonic nanocavity in a two-dimensional photonic crystal. *Nature*, 425:944–947, 2003.

[74] Y. Akahane, T. Asano, B-S. Song, and S. Noda. Fine-tuned high-q photonic-crystal nanocavity. *Opt. Express*, 13:1202–1214, 2005.

[75] V. R. Almeida, Q. Xu, C. A. Barrios, and M. Lipson. Guiding and confining light in void nanostructure. *Opt. Lett.*, 29(11):1209–1211, 2004.

[76] E. Dulkeith, F. Xia, L. Schares, W. M. J. Green, and Y. A. Vlasov. Group index and group velocity dispersion in silicon-on-insulator photonic wires. *Opt. Express*, 14(9):3853–3863, May 2006.

[77] V. R. Almeida, R. R. Panepucci, and M. Lipson. Nanotaper for compact mode conversion. *Opt. Lett.*, 28(15):1302–1304, 2003.

[78] Y. A. Vlasov and S. J. McNab. Coupling into the slow light mode in slab-type photonic crystal waveguides. *Opt. Lett.*, 31(1):50–52, 2006.

[79] M. Parikh. Corrections to proximity effects in electron beam lithography. i. theory. *Journal of Applied Physics*, 50(6):4371–4377, 1979.

[80] M. Parikh. Corrections to proximity effects in electron beam lithography. ii. implementation. *Journal of Applied Physics*, 50(6):4378–4382, 1979.

[81] J. Homola. Present and future of surface plasmon resonance biosensors. *Analytical and Bioanalytical Chemistry*, 377(3):528–539, October 2003.

[82] H. Ouyang, C. C. Striemer, and P. M. Fauchet. Quantitative analysis of the sensitivity of porous silicon optical biosensors. *Appl. Phys. Lett.*, 88:163108, 2006.

[83] N. LaBianca and J. Delorme. High aspect ratio resist for thick film applications. *Proc. of SPIE*, 2438:846–852, 1995.

[84] M. Morita, T. Ohmi, E. Hasegawa, M. Kawakami, and K. Suma. Control factor of native oxide growth on silicon in air or in ultrapure water. *Appl. Phys. Lett.*, 55(6):562–564, 1989.

[85] B. Hatton, V. Kitaev, D. Perovic, G. Ozin, and J. Aizenberg. Low-temperature synthesis of nanoscale silica multilayers - atomic layer deposition in a test tube. *J. Materials Chem.*, 20: 6009–6013, 2010.

[86] X. Yang, C. J. Chen, C. A. Husko, and C. W. Wong. Digital resonance tuning of high-q/v_m silicon photonic crystal nanocavities by atomic layer deposition. *Appl. Phys. Lett.*, 91:161114, 2007.

[87] X. Fan, I. M. White, S. I. Shopova, H. Zhu, J. D. Suter, and Y. Sun. Sensitive optical biosensors for unlabeled targets: A review. *Analytica Chimica Acta*, 620:8–26, 2008.

[88] J. Lee, W. Shen, K. Payer, T. P. Burg, and S. R. Manalis. Toward attogram mass measurements in solution with suspended nanochannel resonators. *Nano Lett.*, 10(7):2537–2542, 2010.

[89] D. Erickson, T. Rockwood, T. Emery, A. Scherer, and D. Psaltis. Nanofluidic tuning of photonic crystal circuits. *Optics Letters*, 31(1):59–61, January 2006.

[90] C. L. C. Smith, D. K. C. Wu, M. W. Lee, C. Monat, S. Tomljenovic-Hanic, C. Grillet, B. J. Eggleton, D. Freeman, Y. Ruan, S. Madden, B. Luther-Davies, H. Giessen, and Y. Lee. Microfluidic photonic crystal double heterostructures. *Applied Physics Letters*, 91(12), September 2007.

[91] C. L. C. Smith, U. Bog, S. Tomljenovic-Hanic, Michael W. Lee, D. K. C. Wu, L. O'Faolain, C. Monat, C. Grillet, T. F. Krauss, C. Karnutsch, R. C. McPhedran, and B. J. Eggleton. Reconfigurable microfluidic photonic crystal slab cavities. *Optics Express*, 16(20):15887–15896, September 2008.

[92] U. Bog, C. L. C. Smith, M. W. Lee, S. Tomljenovic-Hanic, C. Grillet, C. Monat, L. O'Faolain, C. Karnutsch, T. F. Krauss, R. C. McPhedran, and B. J. Eggleton. High-q microfluidic cavities in silicon-based two-dimensional photonic crystal structures. *Optics Letters*, 33(19):2206–2208, October 2008.

[93] D. Psaltis, S. R. Quake, and C. Yang. Developing optofluidic technology through the fusion of microfluidics and optics. *Nature*, 442(7101):381–386, July 2006.

[94] M. Lipson. Guiding, modulating, and emitting light on silicon - challenges and opportunities. *Journal of Lightwave Technology*, 23(12):4222–4238, December 2005.

[95] K. K. Lee. *Transmission and routing of optical signals in on-chip waveguides for silicon microphotonics*. PhD thesis, Massachusetts Inst. of Technology, 2001.